Studies on Low-temperature De-NO_x System over TiO_2-based Photocatalysts

YAMAMOTO AKIRA

2015

Preface

Photocatalysis has been investigated since the early part of 19th century. In the history of photocatalysis, the most innovative work is the discovery of water decomposition using TiO_2 electrodes under UV-light irradiation (Honda–Fujishima Effect) in 1972. The discovery accelerated the researches on photocatalysis, and at present, many researchers are dealing with the photocatalysts and the related phenomena. Water decomposition is eagerly investigated not only to solve the energy problem but also to imitate plant photosynthesis (i.e., artificial photosynthesis). On the other hand, one of the most promising fields on photocatalysis is decomposition of organic pollutants for air purification. Many researches have been done in this topic, and there are some examples commercialized. However, up to date, water decomposition using photocatalysts has not been commercialized, and the application range in decomposition of organic pollutants have been limited. The essential and potential problem is the low activity (low conversion and/or low apparent quantum yield) of the photocatalysts, and the improvement is the most important theme to put the photocatalytic system into practical use.

It is assumed that the cause of the low activity is not the same in these two systems. In water decomposition, a large amount of substrate (i.e., H_2O) exists in the system and is fully supplied to a catalyst surface in the reaction condition. Thus, the low activity is related to a material itself used as a photocatalyst. In contrast, substrate concentrations are typically low in decomposition of organic pollutants if the target is air purification. In such a low concentration system, the catalytic activity is limited by diffusion and adsorption of substrates. Although there were many investigations to improve the adsorption of substrates, the kind of substrate and environments of the target (e.g., temperature, concentration, and co-existential gas) restrict the activity ultimately. The limitation would narrow the application range in photocatalysts in air purification.

Considering the concentration range of substrates, the optimum concentration, at which photocatalysts show high performance, should be exist (naturally, it depends on the kind of substrate). At a high concentration of substrates, the conversion become low because it defined as a ratio of products to substrates added into the system. Lowering the concentration of substrates leads to low conversion because of the limitation of its diffusion and adsorption. Thus, the optimum target concentration should be chosen to draw the maximum performance of photocatalysts. In addition, a clear advantage is required in economic and environmental viewpoints for the practical use of photocatalysts because light energy is not inexpensive compared to thermal energy.

On the other hand, emission of nitrogen oxide (NO_x) causes serious environmental problems such as acid rain and photochemical smog. In developed countries, the acid rain and the photochemical smog have been actualized and become visible since the first part of 19th century. The acid rain killed plants, polluted rivers and lakes, and damaged stone figures and buildings. The photochemical smog damaged eyes and skin of human and caused serious health problems. In Japan, it was recognized that these environmental problems are serious in both human health and ecological system during the era of high-speed economic growth. The first regulation of NO_x emission was introduced based on the air pollution control act (1973) in Japan. The regulation accelerated the research on the removal technology of NO_x (de-NO_x). At present, the regulation is becoming stricter step by step, and the researchers in academia and company are challenging the improvement of the de-NO_x technology.

NO_x exhausted from motor vehicles has been strictly regulated in these years, and thereby the novel and innovative approaches are strongly required to control it. As a matter of course, decomposition of NO_x is difficult once NO_x is exhausted and diffused into the air because of the above-mentioned reason. Thus, NO_x is removed in a concentrated condition prior to its diffusion into the air. Even in such a concentrated condition, the actual concentration of NO_x is not high in the exhaust gas from motor vehicles (< 1000ppm). Although photocatalysts would have a potential to decompose it effectively in terms of its concentration range, the performance of photocatalysts has not been evaluated adequately. Thus, in this thesis, the target was fixed in NO_x removal in the exhaust gas using photocatalysts. To meet the future's regulation of NO_x emission, the photocatalyst is one of the candidates even though it has a potential disadvantage of use of light energy.

The theme on this thesis is evaluation, application, and developments of photocatalysts for de-NO_x system under practical exhaust gas conditions, and elucidation of the working mechanism. Two types of photocatalytic systems were investigated in this viewpoint. One is selective catalytic reduction of NO with NH_3 over TiO_2-based photocatalysts; in this study, the activity was improved into a satisfactory level at a practical gas hourly space velocity (GHSV) by means of the improvement of both the system and the photocatalyst based on the reaction mechanism. Effects of the reaction temperature were investigated in detail, and were clearly explained using kinetic and thermodynamic parameters by the aid of kinetic analysis. This is a novel approach to interpret the effect of the reaction temperature on photocatalysis using kinetic analysis. Besides, the author successfully developed visible-light-sensitive photocatalysts combining various dyes with TiO_2. In both investigations, improvements of the activity were achieved and the reasonable mechanisms of the activity improvements were proposed. In addition, effect of SO_2 gas, which is a poisoning gas for the catalysts, was investigated, and the poisoning mechanism was proposed in the photocatalytic system. Another approach for the NO_x removal at low temperatures is NO_x storage on TiO_2-based photocatalysts. In this research, the author demonstrated the modification of TiO_2 with Ba species greatly enhanced the performance of NO_x storage under UV-light irradiation. The role of Ba was investigated by means of various spectroscopic methods and the Ba–Ti mixed oxide phase was proposed to be active components for NO_x storage. In the above two types of de-NO_x systems using photocatalysts, the author demonstrated the effectiveness of the photocatalysis for de-NO_x system in the exhaust gas by means of development of the photocatalytic system and the photocatalysts. The author hopes that the photocatalytic de-NO_x system is commercialized into practical use in exhaust gas and contributes to the solution of the environmental problems.

The studies presented in this thesis were performed at Department of Molecular Engineering, Graduate School of Engineering, Kyoto University from 2010 to 2015 under the supervision of Prof. Tsunehiro Tanaka. The author wishes to express his sincere gratitude to Prof. Tsunehiro Tanaka for his exact guidance, fruitful discussions, insightful suggestions and valuable comments, throughout this study. The author makes grateful acknowledgements to Prof. Kentaro Teramura for his instructive discussions, warmhearted advices, and continual encouragement. The author's heartfelt appreciation goes to Dr. Saburo Hosokawa for his beneficial suggestions, and helpful supports. The author thanks sincerely his heart to Prof. Tetsuya Shishido at Tokyo Metropolitan University for his insightful comments and encouragement. Special thanks are made to Prof. Hisao Yoshida at Kyoto University and Prof. Tomoko Yoshida at Osaka City University for their valuable discussions and kind supports. The author demonstrates his gratitude at Prof. Hiromi Yamashita at Osaka University, Prof. Hiroshi Kominami at Kinki University, Prof. Sakae Takenaka at Kyushu University, Prof. Takashi Yamamoto at Tokushima University, Prof. Fumiaki Amano at The University of Kitakyushu, Dr. Seiji Yamazoe at The University of Tokyo, and Dr. Hiroki Miura at Tokyo Metropolitan University for their valuable suggestions, warmhearted advices and cheerful messages. The author shows gratitude to the staff of SPring-8 in Hyogo Prefecture for their technical supports in XAFS measurement.

The author expresses his gratitude to Dr. Junya Ohyama at Nagoya University, for his considerable encouragement, thoughtful advise, and continuing support since the time the author started the research in Prof. Tanaka's laboratory. The author is deeply grateful to Dr. Shinya Furukawa at Tokyo Institute of Technology, Dr. Hiroyuki Asakura at Nagoya University, Dr Tomoyuki Kitano at Nippon Shokubai Co., Ltd., who were seniors in the Prof. Tanaka's laboratory, for their fruitful suggestions and kind encouragement. Special thanks also go to Dr. Atsuhiro Tanaka at Ritsumeikan University for his invaluable helps and kind advices.

The author is indebted to Mr. Yuto Mizuno for his significant contribution and extensive discussions on the study. The author thanks Dr. Wang Zheng and Dr. Deng Lidan, who were the same-age peers in the doctor course, for their kind helps and supports. Many thanks are dedicated to Mr. Shoji Iguchi, who was a colleague of the laboratory, for his helpful discussions and advices. Thanks should be made to the same-age peers, Mr. Hiroaki Nasu, Mr. Hirotaka Kuno, Mr. Shota Okazaki, and Mr. Takashi Sato, for their kind supports and fruitful discussions. The author thanks to Lab Secretary Mrs. Ayako Tanaka and Mrs. Mami Nishio for their kind official supports. The author is grateful to all the members of the Prof. Tanaka's laboratory.

Finally, the author sincerely thanks his parents Kiyoshi and Miwako, his grandparents Sawako and Hideo, his younger brother Kenji, his uncle Yasuhiro and Takashi, and his aunt Kazumi for their understanding and encouragement.

Akira Yamamoto

Kyoto,

March, 2015

CONTENTS

General Introduction

De-NO_x technology in stationary emission sources

Nitrogen oxide (NO_x, x = 1, 2), which is one of the air pollutants, causes acid rain and photochemical smog. Emission of NO_x was strictly regulated in terms of the environmental protection. Emission sources of NO_x were classified into two types: stationary emission sources (e.g., thermal power plants and incinerators) and mobile emission sources (e.g., automobiles, ships, and trucks). In both NO_x emission sources, catalytic technologies have been investigated and developed for NO_x emission control. Reduction of NO_x to harmless N_2 is intrinsically difficult because the exhaust gas includes excess O_2 in the air; the reduction of NO_x should be done under such a oxidative condition. In the stationary emission sources, selective catalytic reduction with NH_3 (NH_3-SCR) is used to control the NO_x emission in the presence of excess O_2. The NH_3-SCR systems were at first installed in Japan in the late 1970s, and nowadays, are used worldwide for the control of NO_x emission from the stationary emission sources due to the high efficiency and economics.[1-3] A typical catalyst for the NH_3-SCR is a supported vanadium oxide (V_2O_5) catalysts promoted by tungsten and molybdenum oxide. The operating temperature is typically over 573 K, at which NO_x is efficiently decomposed to N_2 over the catalyst.[2, 4] In the NH_3-SCR, NH_3 functions as a reductant and reacts with NO to form N_2. The detail reaction mechanisms were reviewed in the previous reports.[5] One of the problems in the NH_3-SCR system is a deactivation of the catalyst by poisoning materials such as SO_x, halogen compounds, and particulate matter (PM) in the exhaust gas. To avoid the catalyst deactivation, the removal equipment for the poisoning materials are installed prior to the de-NO_x system (i.e., desulfurization, de-halogen, dust collection, and PM combustion). As a result, the temperature of the exhaust gas decreased to approximately 473 K, and below 473 K the above-mentioned V_2O_5 catalysts do not work efficiently.[5] Thus, undesired re-heating process in the V_2O_5 catalysts is necessary to obtain the high-efficiency of NO_x removal in the NH_3-SCR system.

De-NO_x technology in mobile emission sources

NO_x emission from the mobile sources is a serious problem. In Japan, the regulation in mobile NO_x emission sources was introduced in 1973 based on the air pollution control act, and have become stricter step by step to date. In addition, new emission standards are planned to be introduced and the emission amount is restricted more strictly in the near future.[6] The typical de-NO_x catalyst is a three-way catalyst and it is installed in motor vehicles with gasoline engines. The three way catalyst, which is composed of Pt, Pd, and Rh, works efficiently around the stoichiometric air-to-fuel (A/F) ratio of 14.7. A typical A/F dependence of the conversion of NO, HC, and CO is shown in Fig. 1.[7] The removal efficiency of NO_x drastically decreased with increasing the A/F ratio from 14.7. In motor vehicles with gasoline engines, the A/F ratio is controlled by adjusting engine operation in response to a signal output from a gas sensor, such as an oxygen sensor, to obtain the high efficiency.

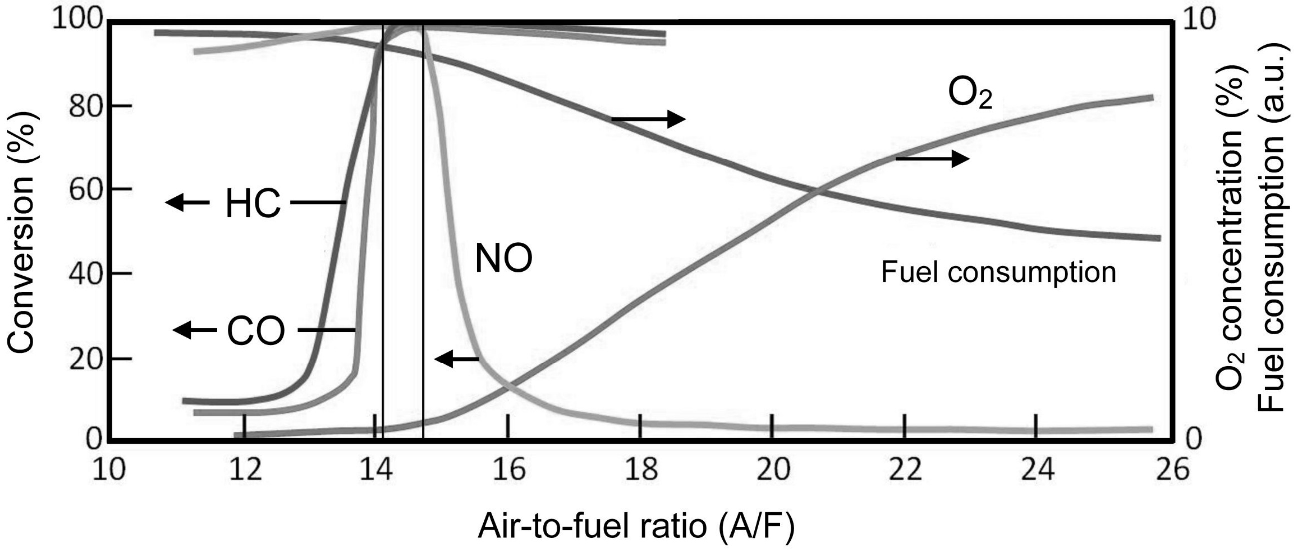

Figure 1. Effect of air-to-fuel ratio on the conversion of NO, CO, and HC. Reprinted with modifications from ref. 7.

NO_x emission in lean conditions

Diesel engines and lean-burn gasoline engines have an advantage in the fuel economy compared to the gasoline engines operated at the stoichiometric point, and use of these engines lowers the fuel consumption up to 30%.[8] In the near future, use of the diesel and lean-burn engines will spread due to the fuel economy and low CO_2 emission because the emission amount of CO_2 from motor vehicles is regulated as well as the NO_x emission.[6] The diesel and lean-burn engines are operated at a high A/F ratio of 25–60, where three way catalysts cannot decompose the NO_x

efficiently. Mainly three technologies have been developed for NO_x removal at high A/F ratio: direct decomposition, NH_3-SCR, and NO_x storage and reduction (NSR).

Direct decomposition of NO_x is an ideal route for NO_x removal without any reductant as shown in eq. 1;

$$NO \rightarrow 1/2\ N_2 + 1/2\ O_2 \quad (1).$$

Several catalysts were reported for the direct decomposition such as Cu-zeolites,[9-10] perovskite-type oxides,[11-13] and $Ag/La_{0.6}Ce_{0.4}CoO_3$.[14] However, the reaction proceeded efficiently only at high temperatures, and the activity decreased drastically in the presence of O_2, H_2O, and SO_2.[8] Although many researches have been carried out, it is not applicable in the practical situations at least in this stage.

The NH_3-SCR technology was developed for the stationary emission sources at first, and then was applied to the mobile emission sources such as diesel engines in ships, trucks, and buses. In the NH_3-SCR, urea is typically used as a NH_3 source (urea-SCR). Urea is introduced to the exhaust gas and the introduced urea decomposes to NH_3 prior to the catalyst bed. The urea-SCR was widely commercialized in the mobile emission sources because it can decompose the NO_x to N_2 selectively with high activity under lean conditions. However, in the mobile emission sources, a problem of the urea-SCR is low activity below 473 K as well as the stationary emission sources. Recently, International Council for Clean Transportation (ICCT) pointed out the impact of the NO_x emission in the initial stage of start-up of engines on the total emission amounts; in the cold start condition below 473 K (approximately 800 s), urea cannot be injected because of the low activity of the catalyst.[15] Thus, improving the activity at low temperatures is a serious challenge in NH_3-SCR.

A concept of NSR technology was proposed by TOYOTA researchers in Japan in the mid-1990s.[16-17] The typical NSR catalyst is composed of three components: precious metal (e.g., Pt), basic materials such as alkali and alkali earth metal oxides (e.g., BaO), and supports (e.g., Al_2O_3). The mechanism of NSR was shown in Fig. 2 using as an example of a $Pt/BaO/Al_2O_3$ catalyst. In the exhaust gas, NO is a main component in NO_x even in the presence of excess O_2. Under the lean conditions, NO in the exhaust gas is oxidized to NO_2 on Pt sites and then trapped onto BaO sites as nitrate (NO_3^-) forms. As the catalyst surface becomes saturated with NO_x species, it needs to be regenerated. After the storage period under the lean conditions, fuels are added to the catalysts for a short period, and the injected fuels reduce the stored NO_x to N_2 (fuel-rich condition). The alternative operation of the lean and rich conditions leads to the effective removal of NO_x from lean-burn engines. The problems in the NO_x storage systems are the low tolerance to SO_x and the use of precious metals such as Pt and Rh. Typically, the exhaust gas includes SO_2, and it drastically deactivates the catalyst performance. In the NSR catalyst, the use of precious metals is inevitable to both oxidize NO into NO_2 under lean conditions and reduce NO_x^- to N_2 under the rich conditions.

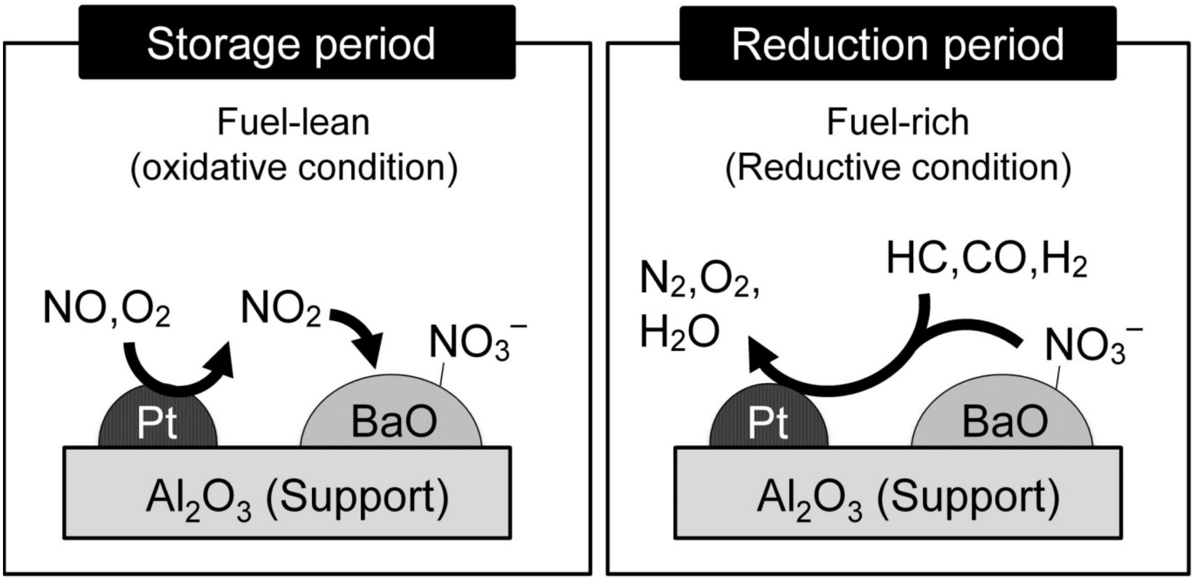

Figure 2. Schematic representation of NO_x storage and reduction in Pt/BaO/Al_2O_3 system .

Demand for low-temperature de-NO_x system

The NH_3-SCR technology is used in not only the stationary emission sources but also the mobile emission sources. In both of the emission sources, a common and fundamental problem of V_2O_5 catalysts is its high operating temperature (623–673 K)[4] as mentioned above, and low-temperature catalysts for NH_3-SCR are strongly desired. Several researchers have investigated the low temperature catalyst for NH_3-SCR.[4] Fe- and Cu-zeolite catalysts show high activity for the NH_3-SCR at 473–573 K.[18-22] Although these catalysts are commercially used, the activity decreased below 473 K.[4] Mn-based catalysts were reported for effective low-temperature catalysts below 473 K.[23-26] The Mn-based catalysts were investigated in morphology, oxidation state of active Mn sites, loading of Mn on metal oxides, and addition of third components into the catalysts.[27-28] However, problems of the Mn-based catalysts were generation of undesired by-products of N_2O and the low SO_2 tolerance.[29] The activity in Mn-based catalysts was drastically decreased in the presence of SO_2 poisoning gas due to the generation of $MnSO_4$. The generated $MnSO_4$ is stable even at high temperature (> 1000 K),[29] which means that the re-activation of the catalyst is difficult at moderate temperatures.

NH_3-SCR systems using photocatalysts

Photocatalysts are one of the promising materials in terms of such a low temperature operation in NH_3-SCR. In 1992, Cant et al. reported the photocatalysis of the reaction between NH_3 and NO on a TiO_2 surface under UV-light irradiation.[30] In their isotopic experiment, $^{14}N^{15}N$ was formed using $^{15}NH_3$ and ^{14}NO over TiO_2, which clearly shows that N_2 was formed via the reaction between NO and NH_3. Although their work was pioneering, there was no report about this reaction for the 8 years after their report possibly because of the following three reasons. The two reasons were the fact that their reaction system was different from the practical NH_3-SCR system; they carried out the reaction (i) in the absence of O_2 (ii) using a closed reactor system. The researchers normally carried out the activity tests in the NH_3-SCR in the presence of excess O_2 using a continuous flow reactor because their target is the exhaust gas including O_2 gas. The third reason was (iii) the low activity; N_2 produced for 30 min was 3.6 μmol, and N_2 formation rate was calculated to be 7.2 μmol h^{-1} (catalyst: ca. 50 mg, light source: 100W mercury lump).

In 2000, Tanaka et al. reported the NH_3-SCR using photocatalysts (photo-SCR) in the presence of O_2, and in their research, they confirmed the formation of N_2 over Rb-ion-modified V_2O_5/SiO_2 photocatalysts under UV-light irradiation. That is the first report in NH_3-SCR using photocatalysts in the presence of O_2.[31] In 2002 and 2003, the same group revealed TiO_2/SiO_2[32] and TiO_2[33-34] photocatalysts showed high activity in photo-SCR. Especially in the case of TiO_2, the high activity was achieved using a continuous flow reactor; inlet NO (1000ppm) was converted to N_2 at the conversion of 80%. The N_2 formation rate was calculated to be 200 μmol h^{-1}, which was 28 times higher that by Cant et al. at the GHSV of 4000 h^{-1} although a large amount of TiO_2 (1.2 g) was used for the reaction. (light source: 300W ultra-high pressure Xe lamp). Teramura et al. also investigated the reaction mechanism using kinetic[35] and spectroscopic methods such as FT-IR spectroscopy,[34] and

ESR.[36] In this mechanism (Fig. 3), amide radicals ($\cdot NH_2$) generated under light irradiation reacts with NO in the gas phase to form N_2 (Eley–Rideal mechanism). The rate-determining step of the photo-SCR was decomposition of nitrosoamide (NH_2NO) intermediates (step 4).[35]

Yamazoe et al. investigated various kinds of TiO_2 photocatalysts,[37] and metal oxide promoted TiO_2 catalysts,[38] and successfully improved the activity of photo-SCR. Among the various photocatalysts investigated, WO_3/TiO_2 photocatalysts showed the highest activity, and NO conversion of 96% and N_2 selectivity to N_2 of > 99% were obtained at a GHSV of 25,000 h^{-1}. The NH_3 adsorption experiments revealed that the loading of WO_3 on TiO_2 increased the amount of weak Lewis acid sites. The DFT calculations suggested that the decomposition rate of the NH_2NO intermediates on weak Lewis acid sites was faster that on strong Lewis acid sites. Thus, the increase of weak Lewis acid sites by loading of WO_3 promotes the decomposition of the NH_2NO intermediates, and it leads to the high activity.[39] Their results give the important suggestion that the promoting the decomposition of the NH_2NO intermediates is effective to improve the activity. In addition, it is worth mentioned that the photo-SCR over TiO_2 proceeds under visible light (λ= 400–450 nm) although TiO_2 itself does not absorb the visible light. The response to visible light was explained by a unique photo-activation mechanism of NH_3: the direct electron transfer from N 2p level of the adsorbed NH_3 to the conduction band of TiO_2 (in situ doping).[40-41] The concept would contributed to the development of new type of visible-light-sensitive photocatalysts.

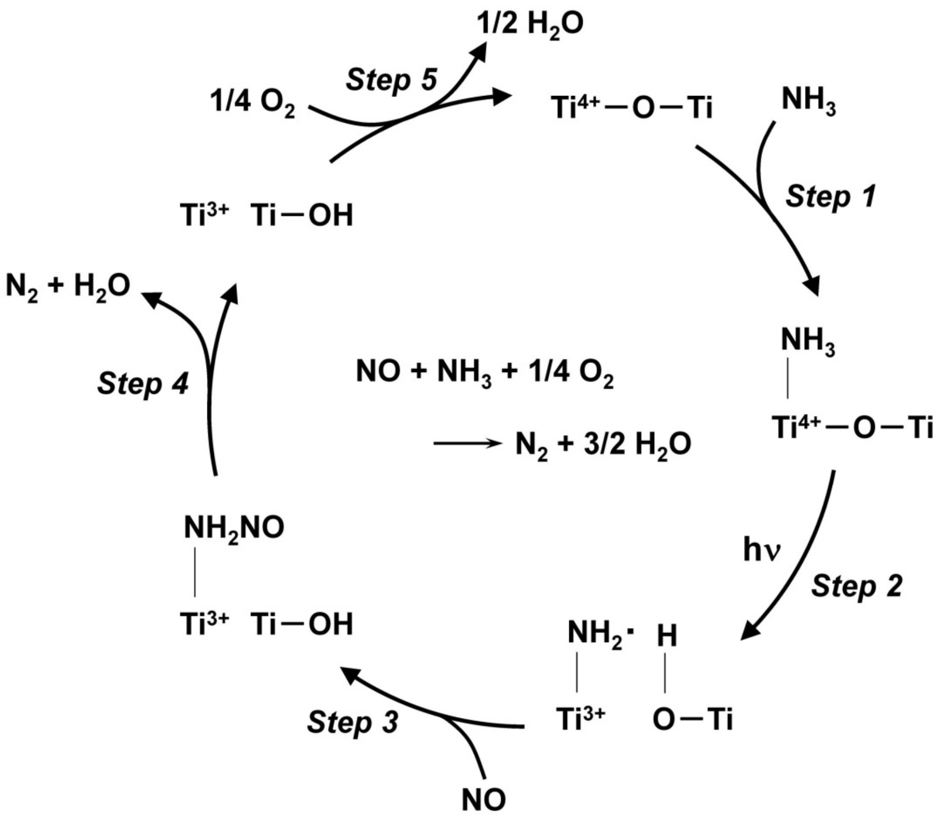

Figure 3. Proposed reaction mechanism of photo-SCR over a TiO_2 photocatalyst. Reprinted with modifications from ref. 34.

Part I: Development of Photo-assisted Selective Catalytic Reduction of NO with NH_3 over Photocatalysts

To put the photo-SCR into the practical de-NO_x system for diesel and lean-burn engines, the following two problems should be considered:

(i) Improving the activity for the practical GHSV conditions.

NO conversion > 90%, N_2 selectivity > 90%, GHSV = 100,000 h^{-1}

(ii) Evaluation of the tolerance to SO_x poisoning

To improve the activity, the author focused on acceleration of elementary steps in the reaction mechanism in Fig. 3. The previous kinetic analysis revealed that the reaction order for NH_3 was approximately zero,[35] which means that the reaction rate of NH_3 adsorption (Step 1) is faster than those of the other elementary steps. Thus, promotion of the other steps (Step 2–4) is necessary to improve the activity. Generally, effective improvement of the activity is achieved by accelerating a relatively slow step that dominates the overall reaction rate. Thus, accelerating the rate-determining step (i.e., Step 4 in the case of photo-SCR)[35] is considered to be the most effective to improve the activity. Moreover, in the case of photocatalsis, the reaction rate of the photo-excitation step (Step 2) is expected to have an great impact on the activity, and the promotion of the Step 2 should be effective to improve the activity. In addition, the tolerance to SO_x poisoning should be evaluated to put photo-SCR into practical use.

Part II: Low-temperature NO_x Storage under Lean-conditions: Photo-assisted NO_x Storage over Photocatalysts

In the exhaust gas from diesel and lean-burn engines, NO_x removal technology at low temperatures (< 473 K) is strongly desired to decrease the total NO_x emission amount in practical driving conditions including a cold start during 800 s from the engine start-up.[15] The NSR catalysts also do not work efficiently below 473 K. Thus, a new technology must be developed to achieve such a low temperature removal of NO_x. In this standpoint, we focused on the concept of the above-mentioned NSR catalysts. In NO_x storage period in Fig. 2, Pt works as oxidation sites for NO into NO_2, and the activity is low at low temperatures.[42-43] Thus, one of the reasons of the low activity in the NSR catalyst should be the low NO oxidation ability of Pt. In contrast, it was previously reported that the NO oxidation proceeded over TiO_2 photocatalysts and TiO_2-based photocatalysts at room temperature under light irradiation.[44-50] These reports indicate that the TiO_2 photocatalysts have a potential to replace the role of Pt (i.e., oxidation of NO) even at low temperatures. Thus, utilization of the photocatalysis has two advantages compared to the typical NSR catalyst on NO_x storage; it lead to not only lowering the operation temperature but also the replacement of Pt. On this background, we investigated and evaluated the performance of photocatalysts under a practical GHSV and NO concentration conditions to develop the low temperature NO_x removal technology without using precious metals.

References

[1] H. Bosch, F. Janssen, *Catal. Today* **1988**, *2*, 369-379.

[2] P. Forzatti, L. Lietti, *Heterog. Chem. Rev.* **1996**, *3*, 33-51.

[3] P. Forzatti, *Appl. Catal. A* **2001**, *222*, 221-236.

[4] J. Li, H. Chang, L. Ma, J. Hao, R. T. Yang, *Catal. Today* **2011**, *175*, 147-156.

[5] G. Busca, L. Lietti, G. Ramis, F. Berti, *Appl. Catal. B* **1998**, *18*, 1-36.

[6] A. Takami, *PETROTECH* **2015**, *38*, 209.

[7] P.-A. Beñat, R. G.-V. Juan, in *Diesel Engine - Combustion, Emissions and Condition Monitoring*, InTech, **2013**.

[8] Z. Liu, S. Ihl Woo, *Catal. Rev.* **2006**, *48*, 43-89.

[9] M. Iwamoto, H. Yahiro, Y. Mine, S. Kagawa, *Chem. Lett.* **1989**, *18*, 213-216.

[10] M. Iwamoto, H. Yahiro, S. Shundo, Y. Yu-u, N. Mizuno, *Appl. Catal.* **1991**, *69*, L15-L19.

[11] C. Tofan, D. Klvana, J. Kirchnerova, *Appl. Catal. B* **2002**, *36*, 311-323.

[12] T. Ishihara, M. Ando, K. Sada, K. Takiishi, K. Yamada, H. Nishiguchi, Y. Takita, *J. Catal.* **2003**, *220*, 104-114.

[13] T. Ishihara, K. Anami, K. Takiishi, H. Yamada, H. Nishiguchi, Y. Takita, *Chem. Lett.* **2003**, *32*, 1176-1177.

[14] Z. Liu, J. Hao, L. Fu, T. Zhu, *Appl. Catal. B* **2003**, *44*, 355-370.

[15] L. Dana, K. Fanta, *Urban off-cycle NO_x emissions from Euro IV/V trucks and buses* **2012**, http://www.theicct.org/urban-cycle-nox-emissions-euro-ivv-trucks-and-buses.

[16] N. Takahashi, H. Shinjoh, T. Iijima, T. Suzuki, K. Yamazaki, K. Yokota, H. Suzuki, N. Miyoshi, S.-i. Matsumoto, T. Tanizawa, T. Tanaka, S.-s. Tateishi, K. Kasahara, *Catal. Today* **1996**, *27*, 63-69.

[17] S. i. Matsumoto, *Catal. Today* **1996**, *29*, 43-45.

[18] R. Q. Long, R. T. Yang, *Chem. Commun.* **2000**, 1651-1652.

[19] R. Q. Long, R. T. Yang, *J. Catal.* **2002**, *207*, 224-231.

[20] J. A. Sullivan, J. Cunningham, M. A. Morris, K. Keneavey, *Appl. Catal. B* **1995**, *7*, 137-151.

[21] A.-Z. Ma, W. Grunert, *Chem. Commun.* **1999**, 71-72.

[22] A. Grossale, I. Nova, E. Tronconi, *Catal. Today* **2008**, *136*, 18-27.

[23] L. Singoredjo, R. Korver, F. Kapteijn, J. Moulijn, *Appl. Catal. B* **1992**, *1*, 297-316.

[24] F. Kapteijn, L. Singoredjo, A. Andreini, J. A. Moulijn, *Appl. Catal. B* **1994**, *3*, 173-189.

[25] J. Li, J. Chen, R. Ke, C. Luo, J. Hao, *Catal. Commun.* **2007**, *8*, 1896-1900.

[26] X. Tang, J. Hao, H. Yi, J. Li, *Catal. Today* **2007**, *126*, 406-411.

[27] W. S. Kijlstra, D. S. Brands, E. K. Poels, A. Bliek, *J. Catal.* **1997**, *171*, 208-218.

[28] W. S. Kijlstra, D. S. Brands, H. I. Smit, E. K. Poels, A. Bliek, *J. Catal.* **1997**, *171*, 219-230.

[29] W. Sjoerd Kijlstra, M. Biervliet, E. K. Poels, A. Bliek, *Appl. Catal. B* **1998**, *16*, 327-337.

[30] N. W. Cant, J. R. Cole, *J. Catal.* **1992**, *134*, 317-330.

[31] T. Tanaka, K. Teramura, T. Funabiki, *PCCP* **2000**, *2*, 2681.

[32] T. Tanaka, K. Teramura, T. Yamamoto, S. Takenaka, S. Yoshida, T. Funabiki, *J. Photochem. Photobiol. A* **2002**, *148*, 277-281.

[33] T. Tanaka, K. Teramura, K. Arakaki, T. Funabiki, *Chem. Commun.* **2002**, 2742-2743.

[34] K. Teramura, T. Tanaka, T. Funabiki, *Langmuir* **2003**, *19*, 1209-1214.

[35] K. Teramura, T. Tanaka, S. Yamazoe, K. Arakaki, T. Funabiki, *Appl. Catal. B* **2004**, *53*, 29-36.

[36] K. Teramura, T. Tanaka, T. Funabiki, *Chem. Lett.* **2003**, *32*, 1184-1185.

[37] S. Yamazoe, T. Okumura, K. Teramura, T. Tanaka, *Catal. Today* **2006**, *111*, 266-270.

[38] S. Yamazoe, Y. Masutani, T. Shishido, T. Tanaka, *Res. Chem. Intermed.* **2008**, *34*, 487-494.

[39] S. Yamazoe, Y. Masutani, K. Teramura, Y. Hitomi, T. Shishido, T. Tanaka, *Appl. Catal. B* **2008**, *83*, 123-130.

[40] S. Yamazoe, K. Teramura, Y. Hitomi, T. Shishido, T. Tanaka, *J. Phys. Chem. C* **2007**, *111*, 14189-14197.

[41] T. Shishido, K. Teramura, T. Tanaka, *Catal. Sci. Technol.* **2011**, *1*, 541-551.

[42] E. Xue, K. Seshan, J. R. H. Ross, *Appl. Catal. B* **1996**, *11*, 65-79.

[43] K. Li, X. Tang, H. Yi, P. Ning, D. Kang, C. Wang, *Chem. Eng. J.* **2012**, *192*, 99-104.

[44] K. Hashimoto, K. Wasada, N. Toukai, H. Kominami, Y. Kera, *J. Photochem. Photobiol., A* **2000**, *136*, 103-109.

[45] K. Hashimoto, K. Sumida, S. Kitano, K. Yamamoto, N. Kondo, Y. Kera, H. Kominami, *Catal. Today* **2009**, *144*, 37-41.

[46] J. Lasek, Y.-H. Yu, J. C. S. Wu, *J. Photochem. Photobiol. C: Photochem. Rev.* **2013**, *14*, 29-52.

[47] T. Ibusuki, K. Takeuchi, *J. Mol. Catal.* **1994**, *88*, 93-102.

[48] R. Dillert, A. Engel, Gro, P. Lindner, D. W. Bahnemann, *PCCP* **2013**, *15*, 20876-20886.

[49] A. Folli, S. B. Campbell, J. A. Anderson, D. E. Macphee, *J. Photochem. Photobiol. A* **2011**, *220*, 85-93.

[50] Q. Wu, R. van de Krol, *J. Am. Chem. Soc.* **2012**, *134*, 9369-9375.

Chapter 1

Effect of Reaction Temperature on Photocatalytic Activity for Photo-SCR of NO with NH_3 over a TiO_2 Photocatalyst

Abstract

Effects of reaction temperature on activity of photo-assisted selective catalytic reduction (photo-SCR) of NO with NH_3 were investigated at very high GHSV condition (100,000 h^{-1}). The reaction temperature had a significant effect on the photo-SCR activity over a TiO_2 photocatalyst. Maximum NO conversion was achieved at 433 K (NO conversion = 84%, N_2 selectivity = 100%). The apparent activation energies in the low and high temperature range were evaluated to be 9.0 kJ mol^{-1} (353–433 K) and –2.7 kJ mol^{-1} (493–593 K), respectively. Kinetic analysis revealed that the rate-determining step in the photo-SCR was decomposition of NH_2NO intermediates in all the range of the reaction temperature (353–593 K). The reaction temperature affects not only the rate constant of decomposition of NH_2NO intermediates but also the total number of active sites ($[S]_0$) and the equilibrium constant of NH_3 adsorption, resulting in the dynamic change of the reaction rate.

Introduction

The removal of NO_x from the exhaust gas of diesel engines has become a major goal for the automotive industry in the last few years. Among the deNO_x technologies, the selective catalytic reduction (SCR) is currently regarded as the most promising one for heavy-duty and light-duty diesel engines.[1] The SCR process is based on the reaction between NO_x present in the flue gases and NH_3 (produced from urea) in the presence of O_2. The V_2O_5–WO_3/TiO_2 catalyst, which is commonly used for stationary SCR systems, shows a relative high conversion at 623 K–723 K.[2] However, this type of catalyst has insufficient performance for diesel engines because the exhaust gas from diesel engines has wide temperature range (373 K–923 K) depending on the engine load.[3] Ion exchanged zeolites, which are practically used in diesel cars, convert NO_x to N_2 with high conversion and selectivity over 433 K.[4-7] However, the ion exchanged zeolites do not work efficiently under 433 K (Conversion of NO is below 40% at 423 K in the case of Cu-ZSM-5 and Fe-ZSM-5, GHSV = 100,000 h^{-1}).[8] On the other hand, non-supported MnO_x[9-10] and supported MnO_x catalysts[11] show high activity for the NH_3-SCR at low temperature, however, the selectivity to N_2 is low.

Photocatalyst, which works at ambient temperature, is one of promising candidates for the de-NO_x process at low temperature. Pichat et al. initially reported that NO produce N_2O and N_2 over UV-irradiated TiO_2 at room temperature.[12] We have reported that photo-assisted selective catalytic reduction of NO with NH_3 (photo-SCR) in the presence of O_2 proceeds over a TiO_2 photocatalyst at room temperature.[13-16] More than 90% of NO conversion and approximately 100 % of selectivity to N_2 were achieved in our systems (GHSV = 8,000 h^{-1}).[16-18] Approximately 10,000 h^{-1} is suitable GHSV for use with typical stationary sources such as power plants, blast furnace, and incinerator. On the other hand, in the case of diesel engines, catalysts are required to work at a very high GHSV region because of a limited installation area of the process for the removal of NO_x and a high flow rate of the exhaust gas. Ultimately, the catalyst volume must be of the order of the engine cylinder volume (typical GHSV in three-way catalyst amount to about 100,000 h^{-1}).[3] This means that driving at much higher GHSV is absolutely imperative in the case that the photo-SCR applies to the removal of NO_x from the exhaust gas of diesel engines. Fig. 1 shows dependence of conversion of NO and selectivity to N_2 for the photo-SCR of NO with NH_3 over TiO_2 at room temperature on GHSV. Unfortunately, the conversion of NO decreased with increasing the GHSV, although the selectivity to N_2 (ca. 96 %) did not change. The conversion of NO descended to 40% at 100,000 h^{-1}. In order to use this photocatalytic system for the industrial SCR system, higher activity is required in the high GHSV region.

The mechanism of photo-SCR of NO with NH_3 over TiO_2 has already been reported by our group as shown in Scheme 1.[19] The process of decomposition of NH_2NO intermediates is a rate-determining step at room temperature in the presence of excess O_2 gas.[17] This process will be promoted by increasing the reaction temperature because it proceeds without photoirradiation, indicating that the reaction rate can be dramatically accelerated by increasing the reaction temperature. Some researchers reported that increment of reaction temperature successfully improved activity for photocatalytic reactions.[20-23] However, the effects of the temperature on the rate of photocatalytic reactions in the gas phase have rarely been studied. In the present study, we investigated effects of the reaction temperature on the photocatalytic activity of the photo-SCR.

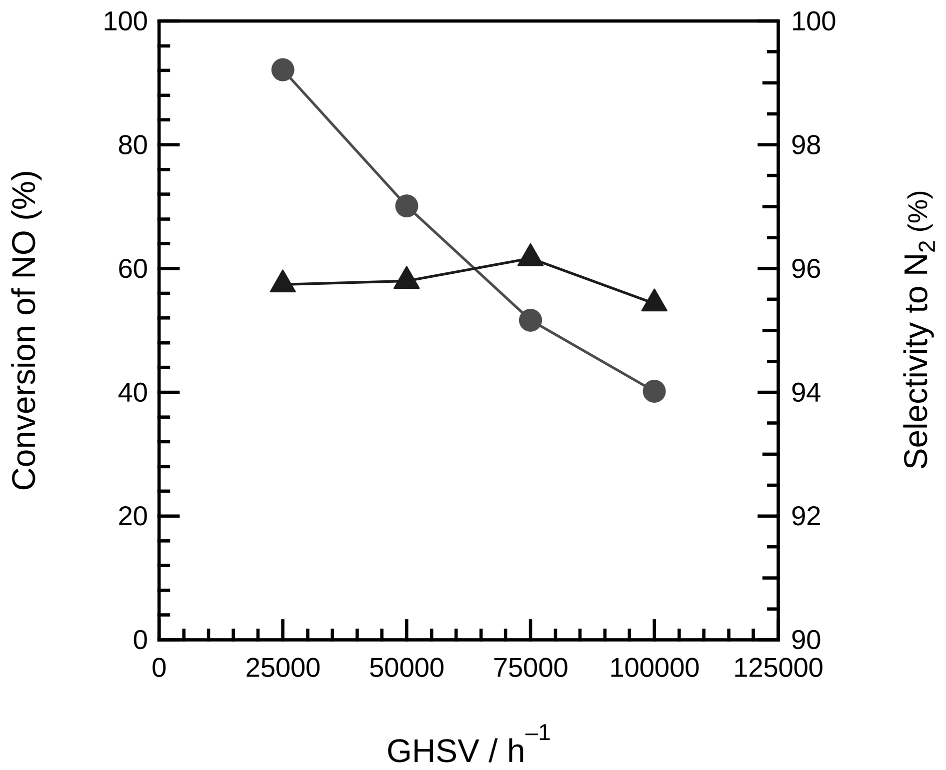

Figure 1. Conversion of NO (●) and N_2 selectivity (▲) in the photo–SCR as a function of GHSV. (catalyst amount: 110 mg, NO: 1000 ppm, NH_3: 1000 ppm, O_2: 2 %)

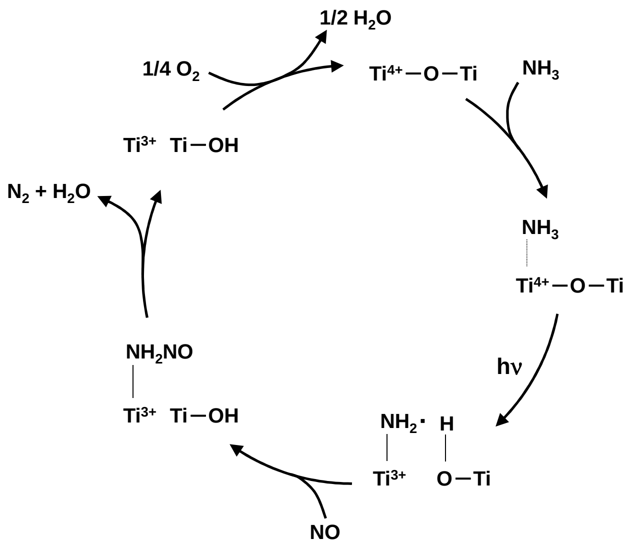

Scheme 1. Proposed reaction mechanism of the photo–SCR over TiO_2.

Experimental

TiO_2 (ST-01, Ishihara Sangyo Kaisha, Ltd.,), which has an anatase phase, was hydrated in distilled water for 2 h at 353 K and was dried at 353 K overnight, followed by calcination in dry air at 673 K for 3 h. The specific surface area of the prepared TiO_2 was evaluated to be 93 $m^2\ g^{-1}$ by the Brunauer–Emmett–Teller (BET) method using N_2 adsorption isotherm at 77 K.

The photo-SCR was carried out in a conventional fixed bed flow system at an atmospheric pressure at various temperatures. A 110 mg of catalyst was fixed with quartz wool and filled up in a quartz reactor which has flat facets (12 mm × 10 mm × 1 mm). Before reactions, catalysts were pretreated at 673 K by flowing 10% O_2 / He gas at 50 mL min^{-1} for 60 min. The reaction gas composition was as follows: NO 1000 ppm, NH_3 1000 ppm, O_2 2%, He balance gas. A 200 W Hg–Xe lamp equipped with fiber optics, collective lens, and a mirror (San-Ei Electric Co., Ltd., UVF-204S type B) was used as a light source and the sample was irradiated from one side of the flat facets of the reactor. The measured light irradiance was 360 mW cm^{-2}. N_2 and N_2O products were analyzed by a SHIMADSU GC-8A TCD gas chromatograph with MS-5A and Porapak Q columns, respectively.

Adsorption isotherms of NH_3 were measured by a volumetric method using a closed vacuum system. A 0.2 g of TiO_2 were evacuated at 673 K for 30 min and then pretreated by O_2 (80 Torr) at 673 K for 60 min. After evacuating at 673 K for 60 min, the catalyst was cooled down to a given temperature. Before adsorption measurements, the dead volume was measured using Ar gas at each temperature. In the first experiment, adsorption amounts of NH_3 were measured at various equilibrium pressures of NH_3 (physical adsorption and chemical adsorption). After evacuation for 90 min, the second adsorption experiment was carried out (physical adsorption). The chemical adsorption amount of NH_3 was calculated by subtracting the adsorption amount of the second experiment from the one of the first experiment.

Results and discussion

Fig. 2 shows dependence of conversion of NO and selectivity to N_2 for the photo-SCR over TiO_2 on reaction temperature. The selectivity to N_2 slightly increased with increasing the reaction temperature and then kept up 100% above 453 K. The conversion of NO drastically increased with increasing the reaction temperature. The maximum conversion of NO (84%) was observed at 433 K. However, it decreased with further increment of the reaction temperature. Fig. 3 displays the time course for the photo-SCR over TiO_2 at 433 K. The conversion of NO reached to 84% as soon as the TiO_2 photocatalyst was irradiated and was kept for at least 480 min, indicating that the TiO_2 photocatalyst used in this study was very stable under the reaction condition. The conversion in the photo-SCR system below 433 K is higher than those of Fe and Cu zeolite catalysts (The conversion of NO is below 40% in the case of Cu-ZSM-5 and Fe-ZSM-5 at 423 K at GHSV = 100,000 h^{-1}).[8]

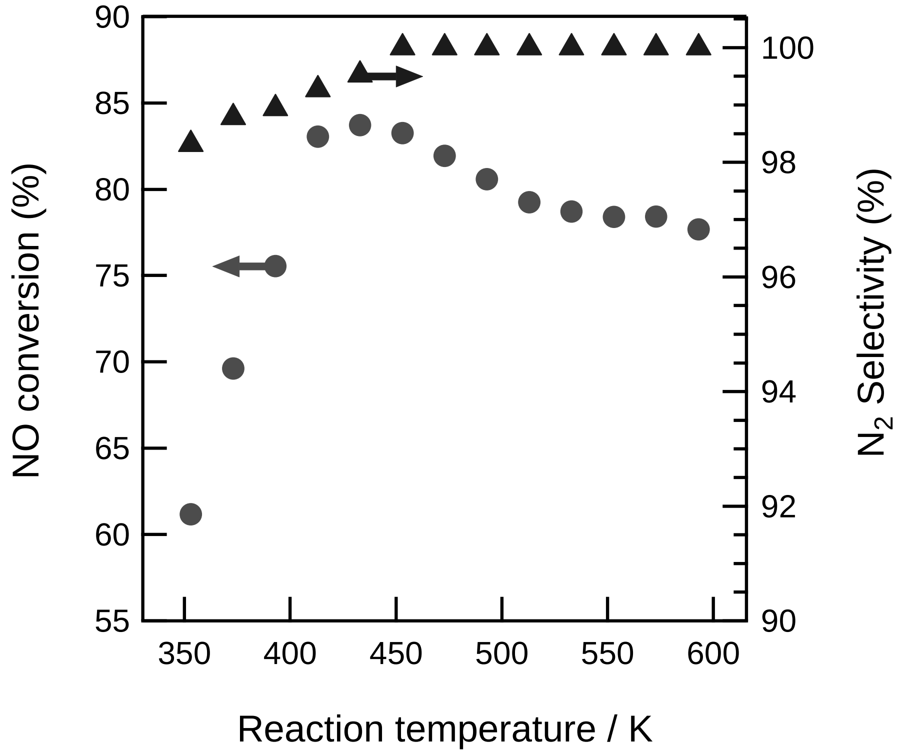

Figure 2. Dependence of conversion of NO (●) and N_2 selectivity (▲) in the photo–SCR on the reaction temperature. (catalyst amount: 110 mg, NO: 1000 ppm, NH_3: 1000 ppm, O_2: 2 %, GHSV: 100,000 h^{-1})

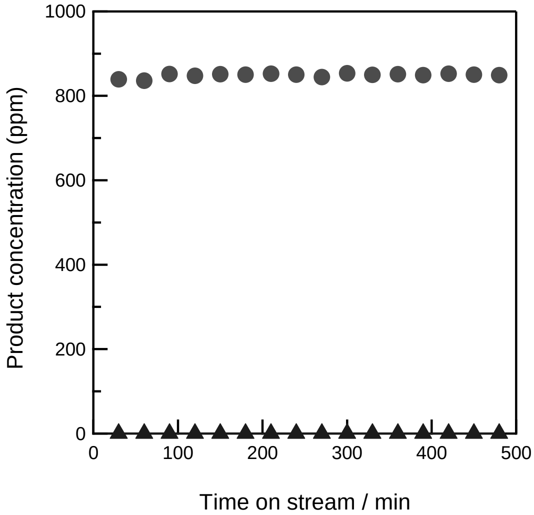

Figure 3. Time profile of conversion of NO in the photo–SCR at 323 K (●) and 433 K (▲). (catalyst amount: 110 mg, NO: 1000 ppm, NH_3: 1000 ppm, O_2: 2 %, GHSV: 100,000 h^{-1})

We carried out the photo-SCR at lower contact time (catalyst amounts: 16 mg) to evaluate the initial rates. The selectivity to N_2 was 100% at all the temperatures. Arrhenius plot (Ln r v.s. 1/T) of the initial rates is shown in Fig. 4. The NO conversion denoted the same tendency of Fig. 2. In the low (353–433 K) and high (493–593 K) temperature range, the logarithm of N_2 formation rate shows a good linear relation to the inverse number of the reaction temperature. In these two temperature ranges, following equations were obtaind using a linear fitting:

$$\ln r = 6.08 - 1.08 \times 10^3 / T \quad (353 - 433\ \mathrm{K}) \tag{1}$$

$$\ln r = 2.98 + 3.26 \times 10^2 / T \quad (493 - 593\ \mathrm{K}) \tag{2}$$

where, r is the N_2 formation rate (nmol s^{-1}) and T is the absolute reaction temperature (K). Using the slope of these equations, the activation energies were estimated to be 9.0 kJ mol^{-1} (353–433 K) and -2.7 kJ mol^{-1} (493–593 K).

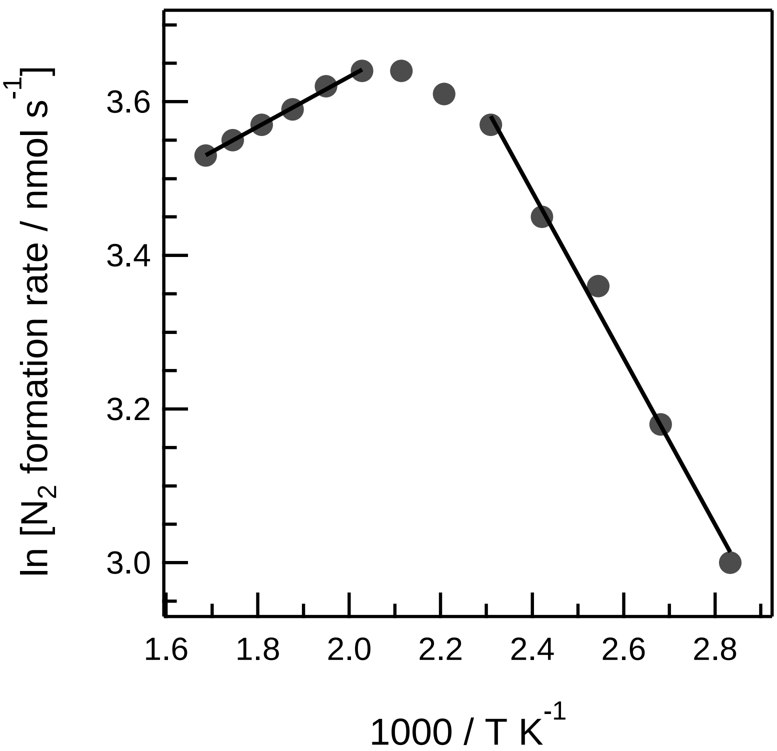

Figure 4. Arrhenius plots of the photo–SCR. (catalyst amount: 16 mg, NO: 1000 ppm, NH_3: 1000 ppm, O_2 2 %, GHSV: 100,000 h^{-1})

The first increase of the photocatalytic activity at the temperature range in 353–433 K would be due to the acceleration of the rate-determining step, which is the decomposition of NH_2NO intermediates at room temperature.[17] To determine the rate-determining step in the temperature range between room temperature and 553 K, the kinetic study was carried out at various temperatures. The reaction rate of the photo-SCR is expressed as a following formula:

$$r = k\, P_{NO}^{\alpha}\, P_{NH_3}^{\beta}\, P_{O_2}^{\gamma}\, I^{\delta} \tag{3}$$

where P_x is a partial pressure of x (x = NH_3, NO, and O_2) and I is irradiance. To obtain the reaction order (α, β, γ, and δ) at various temperatures, the photo-SCR was carried out under the condition of the various partial pressures of NO, NH_3 or O_2, or different light intensities. The reaction orders at each temperature are listed in Table 1.

Table 1. Reaction orders at each temperature

T / K	α^{*1}	β^{*2}	γ^{*3}	δ^{*4}
323	0.01	0.58	0.33	0.75
373	0.09	0.48	0.19	0.71
433	0.12	0.46	0.29	0.6
553	0.17	0.49	0.29	0.58

Reaction orders of NH_3 ^{*1}, NO^{*2}, O_2 ^{*3}, and irradiance^{*4}.

The rate constant and equilibrium constant of each elementary step are defined on the basis of proposed reaction mechanism as follows:

STEP 1 $NH_3 + S \rightleftarrows NH_3{-}S$ $K_1 = k_1/k_{-1}$ (4)

STEP 2 $NH_3{-}S + h\nu \rightleftarrows {}^{\bullet}NH_2{-}S^* + H^+$ $K_2 = k_2/k_{-2}$ (5)

STEP 3 $NO + {}^{\bullet}NH_2{-}S^* \rightleftarrows NH_2NO{-}S^*$ $K_3 = k_3/k_{-3}$ (6)

STEP 4 $NH_2NO{-}S^* \rightleftarrows N_2 + H_2O + S^*$ $K_4 = k_4/k_{-4}$ (7)

STEP 5 $1/4\ O_2 + S^* + H^+ \rightleftarrows 1/2\ H_2O + S$ $K_5 = k_5/k_{-5}$ (8)

We calculated the following rate equations by assuming that each step is a rate-determining step:

$$r = \frac{k_1 P_{NH_3} [S]_0}{1 + (1/K_5 P_{O_2}^{1/4})} \tag{9}$$

$$r = \frac{k_2 K_1 P_{NH_3} I[S]_0}{1 + K_1 P_{NH_3} + (1/K_5 P_{O_2}^{1/4})} \tag{10}$$

$$\mathrm{r} = \frac{k_3 K_1 K_2 P_{NH_3} P_{NO} I[S]_0}{1 + K_1 P_{NH_3} + K_1 K_2 P_{NH_3} I + (1 + 1/K_5 P_{O_2}^{1/4})} \tag{11}$$

$$r = \frac{k_4 K_1 K_2 K_3 P_{NH_3} P_{NO} I[S]_0}{K_1 P_{NH_3} + K_1 K_2 P_{NH_3} I + K_1 K_2 K_3 P_{NH_3} P_{NO} I + (1/K_5 P_{O_2}^{1/4})} \quad (12)$$

$$r = k_5 P_{O_2}^{1/4} [S]_0 \quad (13)$$

where, $[S]_0$ is the total number of active sites. The reaction orders of P_{NO} in the Eqs. 9, 10, 11, and 13 do not satisfy the experimental reaction orders at all the temperatures in Table 1. Consequently, Steps 1, 2, 3, and 5 are excluded from candidates for the rate-determining step. The Eq. 12 satisfies the experimental reaction orders at all the temperatures, which indicates that the rate-determining step in the photo-SCR is step of decomposition of NH_2NO intermediates (Step 4) in the temperature range studied. The conversion of NO increased with increasing the reaction temperature from 353 K to 433 K because the decomposition process of NH_2NO intermediates was promoted by the thermal effect (k_4 in Eq. 12 increased as the reaction temperature increased).

The increase of k_4 has only a positive effect on the activity. Accordingly, it is unaccountable for the reason why the NO conversion decreased as the reaction temperature increased from 433 K to 593 K. Two reasons have been proposed for the appearance of negative apparent activation energies. One is thermal deactivation of catalysts[24] and the other is the case that an exothermic and equilibrium reaction in elementary steps have an effect on the overall reaction rate.[25] To confirm whether thermal deactivation of the catalysts occurs or not, we elevated the reaction temperature in the photo-SCR to 593 K at first, and then lowered it to 353 K (Fig. 5). If the thermal deactivation occurs, NO conversion in the cooling procedure should be lower than that in the heating procedure. The hysteresis curve was not observed between the heating and cooling procedures. This result clearly indicated that the negative apparent activation energy was not due to the thermal deactivation of the catalysts.

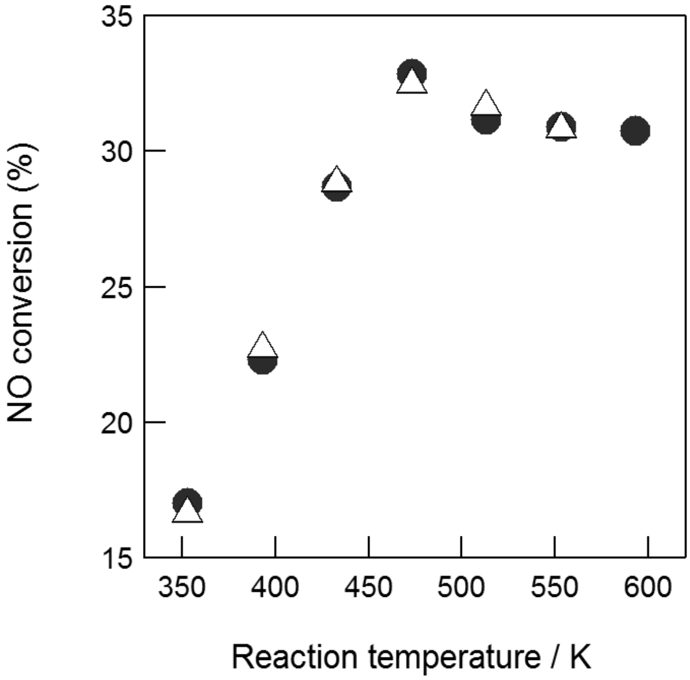

Figure 5. Temperature cycle test in heating procedure (●) and cooling procedure (△). (catalyst amount: 16 mg, NO: 1000 ppm, NH_3: 1000 ppm, O_2 2 %, GHSV: 100,000 h^{-1})

In all the elementary steps (Step 1–5), adsorption of NH_3 (Step 1) is an exothermic and equilibrium reaction. NH_3 adsorption isotherm experiments were carried out at various temperatures as shown in Fig. 6. Amount of NH_3 adsorption clearly decreased as the temperature increased. The Langmuir adsorption isotherm was used to describe the NH_3 adsorption as follows:

$$P_a/q_e = P_a/q_m + 1/q_m K_1 \tag{14}$$

where q_e is the equilibrium adsorption amount (μmol g^{-1}), P_a is the equilibrium partial pressure of NH_3 (atm), q_m is the maximum adsorption capacity (μmol g^{-1}), K_1 is adsorption equilibrium constant (atm^{-1}). The q_m and K_1 at each temperature that are obtained using Eq. 14 are listed in Table 2. The increment of the temperature decreased not only the equilibrium constant of NH_3 adsorption (K_1) but also the maximum adsorption capacity (q_m) of NH_3. The q_m is corresponding to the number of ammonia adsorption sites, which is assumed to be the total number of active sites ($[S]_0$ in the Eq. 12). From the Eq. 12, the decrease of $[S]_0$ and K_1 leads to decline of the overall reaction rate. Thus, we concluded that the overall reaction rate decreased because both the total number of active sites ($[S]_0$) and the value of K_1 decreased with increasing the temperature from 433 K to 593 K.

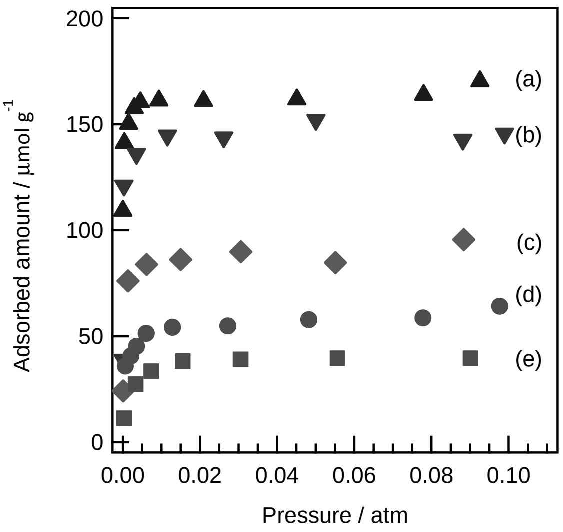

Figure 6. NH_3 adsorption isotherms on the TiO_2 catalyst at various temperatures: (a) 373 K, (b) 413 K, (c) 473 K, (d) 513 K, and (e) 553 K.

Table 2. Langmuir isotherm parameters for the NH_3 adsorption on the TiO_2 at various temperatures.

T / K	q_m / µmol g^{-1}	K_1 / atm^{-1}
373	160.9	1.65×10^4
413	146.5	8.96×10^3
473	90.1	3.13×10^3
513	57.8	1.64×10^3
553	39.8	9.45×10^2

In summary, three kinetic and thermodynamic parameters should be considered as a function of temperature to describe the reaction rate of the photo-SCR: (i) the rate constant of decomposition of NH_2NO intermediates (k_4), (ii) the total number of active sites ($[S]_0$), and (iii) the equilibrium constant of NH_3 adsorption (K_1). In the low temperature range (353–433 K), k_4 dominates the overall reaction rate, which results in the straight and negative line in Arrhenius plots. In the middle temperature range (433–493 K), $[S]_0$ and/or K_1, which decreases as the temperature increases, starts to contribute to the reaction rate, which results in the curved Arrhenius plots. In the high temperature range (493–593 K), contribution of $[S]_0$ and/or K_1 to the overall reaction rate becomes more dominant than that of k_4. As a result, the negative apparent activation energy appeared in high temperature range.

Conclusions

We found the reaction temperature had a significant effect on the photo-SCR activity over a TiO_2 photocatalyst. The photocatalytic activity was increasing with an increase of the reaction temperature from 353 K to 433 K, however deceasing from 433 to 593 K. Maximum conversion was 84% at the high GHSV of 100,000 h^{-1} at 433 K. The high efficiency of the NO removal indicates that the photo-SCR system have a potential for the practical de-NO_x system in deisel engines. The kinetic analysis revealed that the rate-determining step in the photo-SCR is decomposition of NH_2NO intermediates in all the temperature range studied. The calculated rate equation and the NH_3 adsorption experiment indicated that the absorption amount of NH_3 at high temperature affords the key to achieve the high NO conversion, because of a trade-off relationship between the absorption of NH_3 and the decomposition of NH_2NO intermediates. We believe that thermodynamics and kinetics is becoming more important in the field of photocatalysis as well as catalysis.

References

[1] T. Johnson, *Platinum Met. Rev.* **2008**, *52*, 23-37.

[2] G. Busca, L. Lietti, G. Ramis, F. Berti, *Appl. Catal. B* **1998**, *18*, 1-36.

[3] M. Koebel, M. Elsener, M. Kleemann, *Catal. Today* **2000**, *59*, 335-345.

[4] R. Q. Long, R. T. Yang, *J. Am. Chem. Soc.* **1999**, *121*, 5595-5596.

[5] J. A. Sullivan, J. Cunningham, M. A. Morris, K. Keneavey, *Appl. Catal., B* **1995**, *7*, 137-151.

[6] A.-Z. Ma, W. Grunert, *Chem. Commun.* **1999**, 71-72.

[7] A. Grossale, I. Nova, E. Tronconi, *Catal. Today* **2008**, *136*, 18-27.

[8] Y. J. Kim, H. J. Kwon, I. Heo, I.-S. Nam, B. K. Cho, J. W. Choung, M.-S. Cha, G. K. Yeo, *Appl. Catal. B* **2012**, *126*, 9-21.

[9] F. Kapteijn, L. Singoredjo, A. Andreini, J. A. Moulijn, *Appl. Catal. B* **1994**, *3*, 173-189.

[10] M. Kang, E. D. Park, J. M. Kim, J. E. Yie, *Appl. Catal. A* **2007**, *327*, 261-269.

[11] L. Singoredjo, R. Korver, F. Kapteijn, J. Moulijn, *Appl. Catal. B* **1992**, *1*, 297-316.

[12] H. Courbon, P. Pichat, *J. Chem. Soc., Faraday Trans. 1* **1984**, *80*, 3175-3185.

[13] T. Tanaka, K. Teramura, T. Funabiki, *Phys. Chem. Chem. Phys.* **2000**, *2*.

[14] T. Tanaka, K. Teramura, T. Yamamoto, S. Takenaka, S. Yoshida, T. Funabiki, *J. Photochem. Photobiol. A* **2002**, *148*, 277-281.

[15] T. Tanaka, K. Teramura, K. Arakaki, T. Funabiki, *Chem. Commun.* **2002**.

[16] S. Yamazoe, T. Okumura, K. Teramura, T. Tanaka, *Catal. Today* **2006**, *111*, 266-270.

[17] K. Teramura, T. Tanaka, S. Yamazoe, K. Arakaki, T. Funabiki, *Appl. Catal. B* **2004**, *53*, 29-36.

[18] S. Yamazoe, Y. Masutani, K. Teramura, Y. Hitomi, T. Shishido, T. Tanaka, *Appl. Catal. B* **2008**, *83*, 123-130.

[19] K. Teramura, T. Tanaka, T. Funabiki, *Langmuir* **2003**, *19*, 1209-1214.

[20] X. Fu, L. A. Clark, W. A. Zeltner, M. A. Anderson, *J. Photochem. Photobiol. A* **1996**, *97*, 181-186.

[21] J. L. Falconer, K. A. Magrini-Bair, *J. Catal.* **1998**, *179*, 171-178.

[22] J.-F. Wu, C.-H. Hung, C.-S. Yuan, *J. Photochem. Photobiol. A* **2005**, *170*, 299-306.

[23] T. Hisatomi, K. Maeda, K. Takanabe, J. Kubota, K. Domen, *J. Phys. Chem. C* **2009**, *113*, 21458-21466.

[24] S. Kodama, T. Kagiya, S. Machi, T. Shimidzu, S. Yuasa, K. Fukui, *J. Appl. Polym. Sci.* **1960**, *3*, 20-25.

[25] H. zur Strassen, *Z. Phys. Chem.* **1934**, *169*, 81-90.

Chapter 2

Visible-Light-Assisted Selective Catalytic Reduction of NO with NH_3 on Porphyrin Derivative-Modified TiO_2 Photocatalysts

Abstract

Porphyrin-derivative modified TiO_2 photocatalysts showed high photocatalytic activity for the selective catalytic reduction of NO with NH_3 in the presence of O_2 under visible-light irradiation. Tetra(p-carboxyphenyl)porphyrin (TCPP) was the most effective photosensitizer among the five porohyrin derivatives investigated. NO conversion and N_2 selectivity of 79.0% and 100% respectively, were achieved at a gas hourly space velocity of 50,000 h^{-1}. UV–Vis and photoluminescence spectroscopies revealed the presence of two species of TCPP on the TiO_2 surface; one was a TCPP monomer and the other was a H-aggregate of the TCPP molecules. It was concluded that the TCPP monomer is an active species for the photo-assisted selective catalytic reduction (photo-SCR). Moreover, an increase in the fraction of H-aggregates with the increasing TCPP loading amount resulted in a decrease in the decrease of the photocatalytic activity of the photo-SCR.

Introduction

NO_x, which is present in the exhaust gas of stationary emission sources, is removed by the selective catalytic reduction with NH_3 (NH_3-SCR) over vanadium oxide-based catalysts according to the following equation: ($4NO + 4NH_3 + O_2 \rightarrow 4N_2 + 6H_2O$).[1-3] The NH_3-SCR process is performed at temperatures above 573 K. To save the energy used for heating the catalyst bed, novel catalysts are required for performing the NH_3-SCR at low temperatures.[4-6] Photocatalysis is one of the promising candidates for the NH_3-SCR because photocatalytic reactions proceed at room temperature. We have reported the photo-assisted selective catalytic reduction (photo-SCR) of NO with NH_3 in the presence of O_2 over TiO_2 photocatalysts under UV-light irradiation.[7-10] In this system, the NO conversion and N_2 selectivity of 90% and 99%, respectively, were achieved at a gas hourly space velocity (GHSV) of 8,000 h^{-1}, which is sufficient for the deNO_x process in typical stationary sources such as power plants, blast furnaces, and incinerators. However, a very high GHSV was required in diesel engines owing to the limited installation space of the deNO_x process and a high flow rate of the exhaust gas. The volume of the catalyst was required to be of the order of the volume of the diesel engine cylinder (typical GHSV in a three-way catalyst is approximately 100,000 h^{-1}).[11] Unfortunately, the NO conversion decreased with the increasing GHSV in the photo-SCR system and it decreased to 40% at a GHSV of 100,000 h^{-1}.[10] Therefore, the photocatalytic activity of the photo-SCR has to be improved at a high GHSV region in order to remove the NO_x from the exhaust gas of diesel engines.

Expansion of the adsorption wavelength to the visible-light region is an effective way of improving the photocatalytic activity. TiO_2 photocatalysts do not absorb visible light because of their wide band gap (> 3.2 eV). Surprisingly, the photo−SCR proceeds to some extent under visible-light irradiation over the TiO_2 photocatalysts. This is due to the direct electron transfer from the electron donor level of the N 2p orbital of the adsorbed NH_3 to the conduction band of the Ti 3d orbital of TiO_2 (in-situ doping) [12-13]. However, the photocatalytic activity under visible-light irradiation is not sufficient for the application of the photo-SCR technology to the system at a high GHSV region. Thus, the proposed study aims to increase the photocatalytic efficiency under visible-light irradiation.

Porphyrin derivatives have absorption bands in the visible region owing to the π–π* transitions. Porphyrin derivatives are widely used as sensitizers in dye-sensitized solar cells (DSSCs) [14-17] and dye-sensitized photocatalysts [18-20] under visible-light irradiation owing to the following properties: 1) they exhibit intense absorption bands in the visible-light region, and 2) their photochemical and electrochemical properties can be tuned by the modification of the substituents and selection of the central metal. In previous studies, the porphyrin-sensitized photocatalysts were used for performing liquid phase reactions such as the hydrogen production from water,[20] and degradation of organic compounds.[18-19, 21] However, there are only a few reports on the reactions involving porphyrin-sensitized photocatalysts in the gas phase. Recently, Ismail et al. reported that the porphyrin-sensitized mesoporous TiO_2 films exhibited an improved photocatalytic activity for the photodegradation of acetaldehyde in the gas phase under visible-light irradiation.[22] The porphyrin derivative-modified photocatalyst works efficiently as a visible-light response photocatalyst in the gas phase. In this study, we used five types of porphyrins for the modification of the TiO_2 photocatalyst, and investigated their performances in the photo−SCR using a gas flow reactor at a high GHSV of 50,000 h^{-1}.

Experimental

Catalyst Preparation

A TiO_2 powder (ST-01, anatase, 273 m^2 g^{-1}) was purchased from Ishihara Sangyo Kaisha, Ltd. A SiO_2 powder (630 m^2 g^{-1}) was prepared by hydrolysis of tetraethyl orthosilicate (TEOS) in a water–ethanol mixture at boiling point, followed by calcination in dry air at 773 K for 5 h. Tetraphenylporphyrin (TPP), Tetra(*p*-carboxyphenyl)porphyrin (TCPP), Tetra(*p*-sulfonatephenyl) porphyrin (TSPP), Tetra(*p*-methoxyphenyl)porphyrin (TMPP), and Tetra(*p*-aminophenyl)porphyrin (TAPP) were purchased from Tokyo Chemical Industry Co., Ltd. and used without further purification (see Fig. 1). The porphyrin derivatives were impregnated over the TiO_2 powder and the porphyrin-modified TiO_2 photocatalysts were abbreviated to porphyrin-TiO_2 (e.g. TCPP-TiO_2). Various loading amount of TCPP-TiO_2 catalysts were prepared by an impregnation method using 1 M NH_3 aqueous solution as a solvent (TCPP-TiO_2-IMP). A TCPP-modified SiO_2 catalyst was prepared by the impregnation method as shown above (TCPP-SiO_2-IMP). A physical mixture catalyst of TCPP and the TiO_2 powder was prepared as a reference (TCPP-TiO_2-MIX).

Photocatalytic reaction

The photo-SCR was carried out in a conventional fixed-bed flow system at an atmospheric pressure. The catalyst was fixed with quartz wool and filled up in a quartz reactor with flat facets (H12 mm × W10 mm × D1.0 mm). The reaction gas composition was as follows: NO 1000 ppm, NH_3 1000 ppm, O_2 2–10%, He balance. 300 W Xe lamp (PERKIN-ELMER PE300BF) equipped with a L-42 cut-off filter was used as a light source ($\lambda > 400$ nm) and the sample was irradiated from the one side of the flat facets of the reactor. N_2 and N_2O were analyzed by SHIMADZU GC-8A TCD gas chromatographs equipped with MS-5A and Porapak Q.

Characterization

UV–Vis transmission adsorption and diffuse reflectance spectra were obtained with a UV–Vis spectrometer (JASCO V-650). Transmission adsorption spectra were measured using a 1 cm quartz cell at room temperature in the scan range of 300–800 nm. Photoluminescence spectra were recorded on a Hitachi F-7000 fluorospectrometer in the scan range of 550–760 nm at an excitation wavelength of 410 nm. The concentrations of TCPP in methanol solution used in the adsorption and emission spectroscopy were 3.4×10^{-6} mol L^{-1} and 1.0×10^{-6} mol L^{-1}, respectively.

Results and discussion

Effects of functional group in the porphyrins

Fig. 1 shows the conversion of NO during the photo-SCR over the various porphyrin derivative-modified TiO_2 photocatalysts at a GHSV of 50,000 h^{-1} after 6 h of visible-light irradiation. The conversion of NO over the unmodified TiO_2 photocatalyst was 13.4% under visible-light irradiation. Modification of the TiO_2 photocatalyst with the porphyrin derivatives greatly enhanced the photocatalytic conversion of NO under the visible-light irradiation as shown in Fig. 1. Among the five porphyrin derivative-modified TiO_2 photocatalysts, the TCPP-TiO_2 photocatalyst showed the highest conversion of NO (71.4%). The conversion of NO decreased in the following order:

$TCPP-TiO_2$ > $TPP-TiO_2$ > $TSPP-TiO_2$ > $TMPP-TiO_2$ > $TAPP-TiO_2$ > TiO_2. Hence, it can be seen that the porphyrin functional group used for the modification of TiO_2 had a significant effect on the photo-SCR activity.

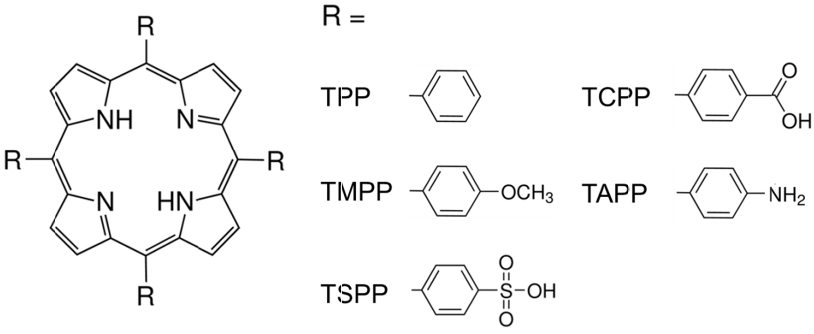

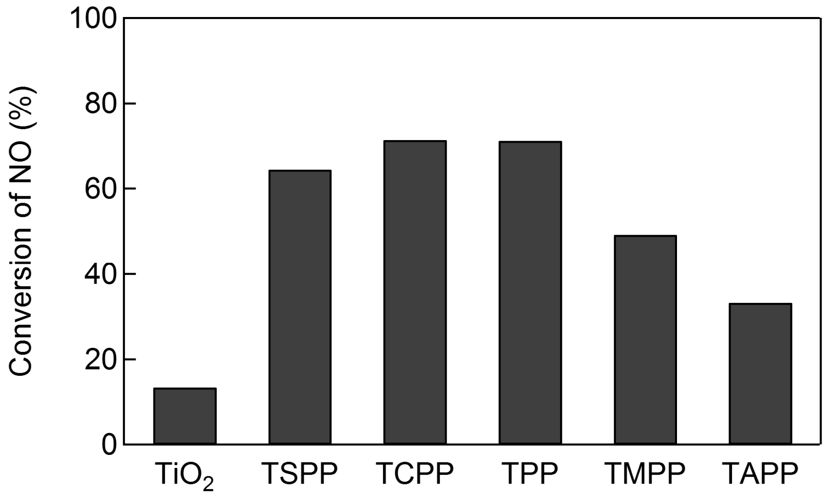

Figure 1. Structures of porphyrin derivatives and conversion of NO in the photo–SCR over the various porphyrin derivative–modified TiO_2 photocatalysts after 6 h of visible–light irradiation (loading of porphyrin derivative: 18 μmol g^{-1}, catalyst amount: 110 mg, NO: 1000 ppm, NH_3: 1000 ppm, O_2: 2 %, GHSV: 50,000 h^{-1}).

Fig. 2 shows the UV–Vis DR spectra of the various porphyrin modified TiO_2 photocatalysts. The unmodified TiO_2 photocatalyst did not absorb the visible-light above 400 nm. The modification of the porphyrin derivatives increased the absorption in the visible-light region. The absorption at 420 nm (Soret band) decreased in the following order: $TCPP-TiO_2$ > $TPP-TiO_2$ ≒ $TSPP-TiO_2$ > $TMPP-TiO_2$ > $TAPP-TiO_2$ > TiO_2. The order of the absorption is consistent with that of the NO conversion. The photocatalytic activities of NO were strongly dependent on the absorbance in the visible-light region, which suggested that the porphyrin derivatives functioned as photosensitizers under visible-light irradiation.

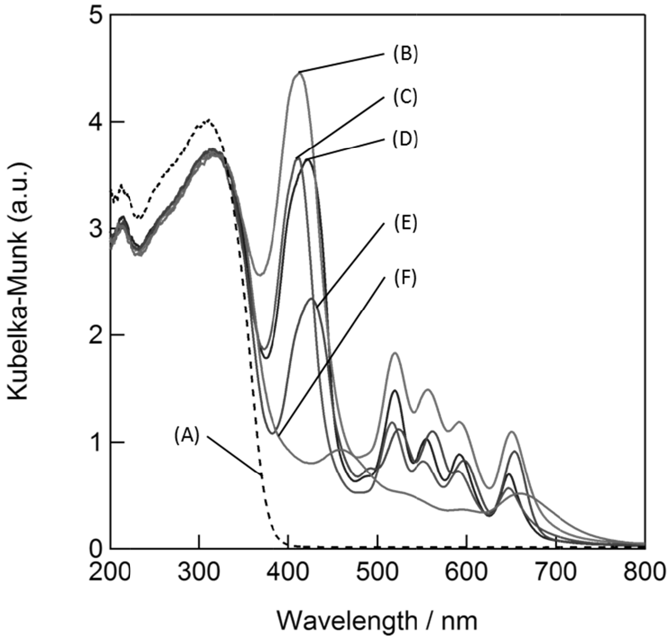

Figure 2. UV–Vis diffuse reflectance spectra of (A) TiO_2, (B) TCPP–TiO_2, (C) TSPP–TiO_2, (D) TPP–TiO_2, (E)TMPP –TiO_2, and (F)TAPP –TiO_2.

Effect of TCPP loading on the activity of photo-SCR

Fig. 3 shows the UV/Vis DR spectra of the different loading amounts of the TCPP-TiO_2 photocatalysts. One major peak and four minor peaks were observed in the visible region in each sample. The major peak is the Soret band ($S_2 \leftarrow S_0$ transition) and the four minor peaks are the Q bands ($S_1 \leftarrow S_0$ transition). The Q bands are attributed to the 0–0 and 0–1 components of the non-degenerated Q_x and Q_y bands (etio type),[23] as expected for the D_{2h} symmetry. The increase in the TCPP loading amount enhanced the capability of visible-light absorption.

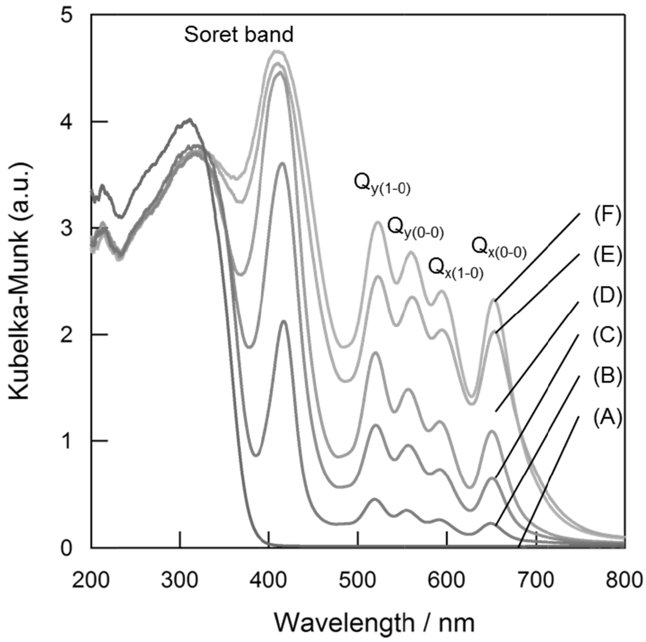

Figure 3. UV–Vis diffuse reflectance spectra of various loading of TCPP–TiO_2. (A) 0 µmol g^{-1}, (B) 1.3 µmol g^{-1}, (C) 6.3 µmol g^{-1}, (D) 12.5 µmol g^{-1}, (E) 37.5 µmol g^{-1}, and (F) 62.5 µmol g^{-1}.

The peak positions of the Soret band and Q bands as a function of TCPP loading are shown in Table 1. The peak position of the Soret band of 1.3 µmol g^{-1} TCPP-TiO_2-IMP (417 nm) corresponded to those of the TCPP molecules dissolved in CH_3OH (418 nm). The TCPP molecules existed as a monomer in the CH_3OH solution and the peak position of the TCPP monomer coincided with that reported previously.[24] Thus, the TCPP molecules existed as monomers on the TiO_2 surface at the low loading amount of 1.3 µmol g^{-1}. The peak position of the Soret band was shifted from 417 nm to 407 nm (blue-shift) when the loading amount of TCPP was increased from 1.3 µmol g^{-1} to 62.5 µmol g^{-1}. The origin of the blue-shift can be explained on the basis of a "face to face" stacking pattern of TCPP (H-aggregate) according to Kasha's exciton theory.[25] Thus, the blue-shifted peak observed at 407 nm can be attributed to the Soret exciton band in the H-aggregates of the TCPP. The gradual spectral shift can be explained as the result of the relative contribution of the monomers and H-aggregates. The H-aggregates were generated with the increase in the TCPP loading. The contribution of the H-aggregates became dominant for the Soret band of adsorption spectra of various loading amount of TCPP-TiO_2, which results in the gradual blue shift of the Soret band.

On the other hand, the peak positions of the Q bands of 1.3 μmol g^{-1} TCPP-TiO_2-IMP (519, 555, 592, 649 nm) were slightly shifted to longer wavelengths compared to those of the TCPP monomer in CH_3OH (515, 549, 590, 646 nm). The slight red-shift can be ascribed to the aggregation of TCPP [24] and/or the interactions between the TCPP and a solid surface.[26] The peak positions of the four Q bands of the TCPP-TiO_2-IMP were shifted to longer wavelengths with an increase in the TCPP loading amount. The peak position of the Q bands of the H-aggregates of the TCPP is larger than that of the TCPP monomers.[24] Thus, the red-shift of the Q bands is due to the generation of the H-aggregates. Consequently, both the monomers and H-aggregates of TCPP are generated on TiO_2 and the fraction of the H-aggregates increased with the increasing TCPP loading amount.

Table 1. Peak positions of the soret band and Q bands.

Sample	Loading of TCPP / μmol g^{-1}	Soret / nm	$Q_{y(0, 1)}$ / nm	$Q_{y(0, 0)}$ / nm	$Q_{x(0, 1)}$ / nm	$Q_{x(0, 0)}$ / nm
TCPP-TiO_2-IMP	1.3	417	519	555	592	649
TCPP-TiO_2-IMP	6.3	416	520	557	592	651
TCPP-TiO_2-IMP	12.5	411	521	559	593	652
TCPP-TiO_2-IMP	37.5	411	522	562	595	654
TCPP-TiO_2-IMP	62.5	407	522	560	594	653
TCPP-TiO_2-MIX	12.5	419	529	565	600	658
TCPP-SiO_2-IMP	12.5	422	521	556	593	649
TCPP in MeOH	–	418	515	549	590	646

Fig. 4 shows the effect of various loading amounts of TCPP-TiO_2-IMP on the photo-SCR. The conversion of NO increased with the increasing TCPP loading amount up to 12.5 μmol g^{-1}. The surface density of TCPP molecules on 12.5 μmol g^{-1} TCPP-TiO_2-IMP is estimated to be 2.8×10^{-2} molecule nm^{-2}. As shown in Fig. 3, increasing the loading amount of TCPP enhanced the capability of the visible-light absorption, which leads to the higher conversion of NO. On the other hand, the conversion of NO decreased when the TCPP loading was higher than 12.5 μmol g^{-1}. The UV–Vis spectroscopy revealed that the H-aggregates of TCPP were generated with the increase of the TCPP loading amount. The excited state lifetime of the H-aggregates was slightly shorter than those of the monomers.[24, 27] The generation of H-aggregates with a short excited state lifetime decreased the electron transfer efficiency from the excited state of TCPP to the conduction band of TiO_2 due to non-radiative deactivation, which possibly resulted in the decrease of the photo-SCR activity.

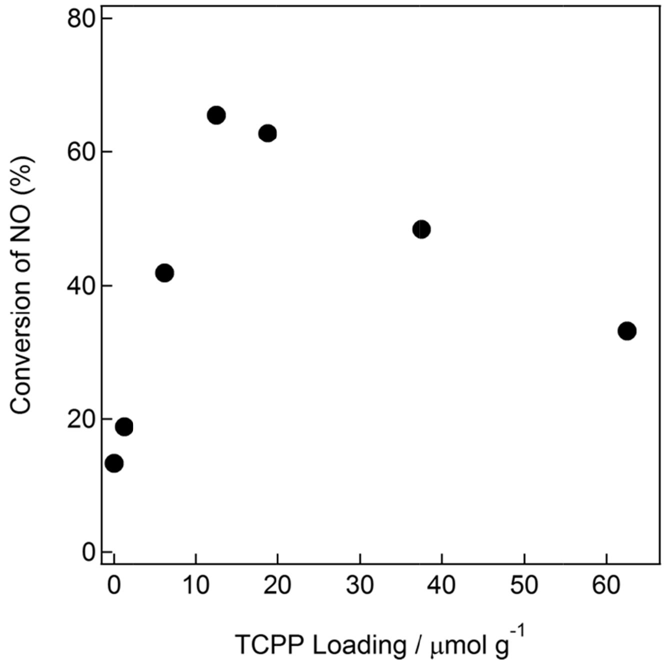

Figure 4. Dependence of conversion of NO on TCPP loading on TiO_2 (catalyst amount: 110 mg, NO: 1000 ppm, NH_3: 1000 ppm, O_2: 2 %, GHSV: 50,000 h^{-1}).

Photo-SCR under various reaction conditions

Table 2 summarizes the concentrations of N_2 in the outlet gas for the photo-SCR under various reaction conditions. The conversion of NO in the photo-SCR over TCPP-TiO_2-IMP was 79.0% (Entry 1). Fig. 5 shows the time profile of the conversion of NO in the photo-SCR over TiO_2, TCPP-TiO_2, and TCPP-SiO_2. The photocatalytic conversion of NO over TCPP-TiO_2 maintained for 6 h without marked deactivation. N_2 was the only product observed and N_2O was not detected in any of the reactions. The utilization of visible-light was advantageous for the high selectivity to N_2, since N_2O was generated as a by-product of the photo-SCR over TiO_2 photocatalyst under UV-light irradiation. Turnover number (TON) of TCPP was calculated to be 810 after 6 h of visible-light irradiation. Thus, the total N_2 in the outlet gas was originated from the nitrogen atoms of NO and NH_3 molecules in the gas phase and not from the TCPP molecules. The reaction hardly proceeded over the TCPP-TiO_2 photocatalyst without a substrate such as NO, NH_3, and O_2 (Entry 2, 3, and 4). The O_2 concentrations did not affect the generation rate of N_2 over 2% (Entry 1, 5, and 6). The TCPP-SiO_2-IMP showed much lower activity under the same reaction conditions than that of the TCPP-TiO_2-IMP (Entry 7), although the TCPP on SiO_2 absorbed visible-light as well as that on TiO_2 as shown in Fig. 6. In addition, the activity of the photo-SCR over the TCPP-TiO_2 photocatalyst prepared by a physical mixture method (TCPP-TiO_2-MIX) was similar to that of the unmodified TiO_2, although the TCPP-TiO_2-MIX absorbed in the visible region as shown in Fig. 6.

Table 2. Results of photo–SCR under various reaction conditions.

Entry	Catalyst	Inlet gas conc. (ppm)			N_2 conc.[a] (ppm)
		NO (ppm)	NH_3 (ppm)	O_2 (%)	
1	TCPP-TiO_2-IMP[b]	1000	1000	2	790
2	TCPP-TiO_2-IMP[b]	0	1000	2	57
3	TCPP-TiO_2-IMP[b]	1000	0	2	24
4	TCPP-TiO_2-IMP[b]	1000	1000	0	42
5	TCPP-TiO_2-IMP[b]	1000	1000	5	780
6	TCPP-TiO_2-IMP[b]	1000	1000	10	771
7	TCPP-SiO_2-IMP[b]	1000	1000	2	63
8	TCPP-TiO_2-MIX[b]	1000	1000	2	140

[a] Concentration of N_2 in the outlet gas. Catalyst amount: 110 mg (TiO_2, TCPP–TiO_2), 50 mg (TCPP–SiO_2), [b] TCPP loading: 12.5 μmol g^{-1}.

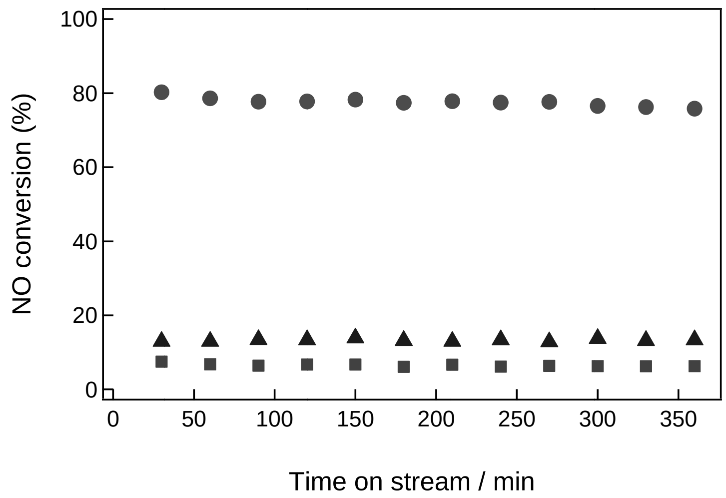

Figure 5. Time profile of conversion of NO in the photo–SCR over TiO_2 (▲), TCPP–TiO_2 (●), and TCPP–SiO_2 (■). (TCPP loading: 12.5 μmol g^{-1}, catalyst amount: 110 mg, NO: 1000 ppm, NH_3: 1000 ppm, O_2: 2%, GHSV: 50,000 h^{-1}).

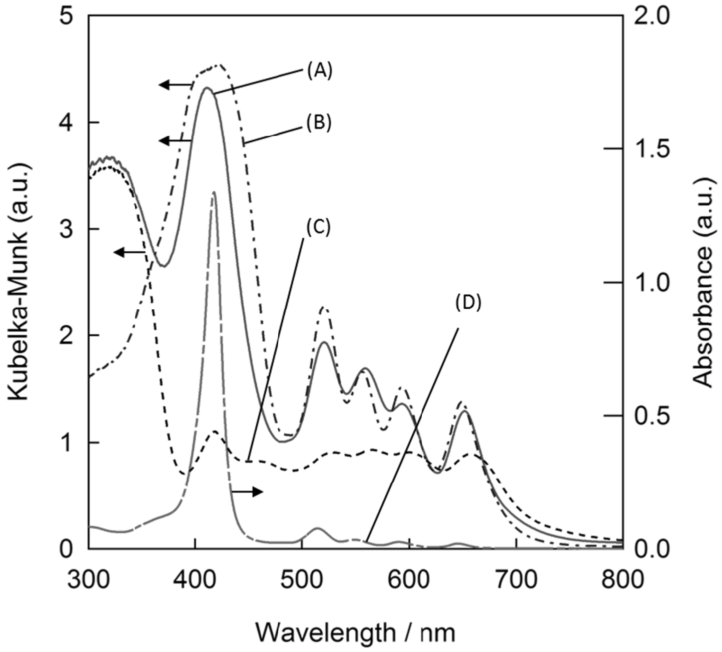

Figure 6. UV–Vis diffuse reflectance spectra of (A) TCPP–TiO_2(IMP), (B) TCPP–SiO_2, and (C) TCPP–TiO_2(MIX), and adsorption spectra of 3.4×10^{-6} mol L^{-1} TCPP in methanol (D).

Fig. 7 shows the photoluminescence spectra of TCPP-TiO_2-IMP, TCPP-SiO_2-IMP, TCPP-TiO_2-MIX, and TCPP monomer in CH_3OH. Two emission bands were observed in the TCPP monomer in CH_3OH solution (650 and 714 nm), which coincided with the previously reported values.[24] The emission bands at 650 nm and 714 nm can be attributed to the transition from the vibrational ground state of S_1 to the vibrational ground state of S_0 ($Q_{x(0,0)}$ transition) and to the vibrational excited state of S_0 ($Q_{x(0,1)}$ transition) of the TCPP monomer, respectively.[24, 28] The peak positions of the emission bands in the TCPP-TiO_2-IMP (654 and 715 nm) were almost similar to those of the TCPP monomer in CH_3OH. It is reported that the emission bands of the H-aggregates of TCPP have lower intensity and are shifted to longer wavelengths than those of the monomers,[29] which is totally different from the emission spectrum of the TCPP-TiO_2-IMP. Accordingly, the emission bands of TCPP-TiO_2-IMP were mainly composed of the TCPP monomer emissions.

Two emission bands were observed at 658 and 713 nm, and the peak positions were similar to those of the TCPP in CH_3OH (650 and 714 nm) and TCPP-TiO_2-IMP (654 and 715 nm) (Fig. 7). Thus, the TCPP species on SiO_2 possesses a monomeric state, which is similar to that on TiO_2. The low activity of TCPP-SiO_2-IMP can be explained by an electron transfer mechanism, which is the key step in the DSSCs and dye-sensitized photocatalysts. In the first step of the photo-SCR over the TCPP-TiO_2-IMP, the TCPP is excited by the visible-light irradiation. In the next step, the electron transfer occurs from the photo-excited TCPP to the conduction band of TiO_2. However, the electron transfer cannot occur from the photo-excited TCPP to the conduction band of SiO_2 because the energy level of the SiO_2 conduction band is much higher than that of the lowest unoccupied molecular orbital (LUMO) of TCPP, which results in the low activity of the TCPP-SiO_2-IMP. Hence, the photo-SCR over TCPP-TiO_2-IMP under visible-light irradiation proceeds via the electron transfer from the photo-excited TCPP to the conduction band of TiO_2.

No emission peak was observed for the TCPP-TiO_2-MIX and TCPP powder (Fig. 7). The interaction between the TCPP molecules might lead to the non-radiative deactivation of the photo-excited states of TCPP, resulting in the luminescence quenching for the TCPP-TiO_2-MIX and TCPP powder. These results explain the low activity of the TCPP-TiO_2-MIX, *i.e.* though the TCPP molecules on the TCPP-TiO_2-MIX absorb visible-light, they do not function as a photosensitizer under visible-light irradiation because of the fast non-radiative quenching.

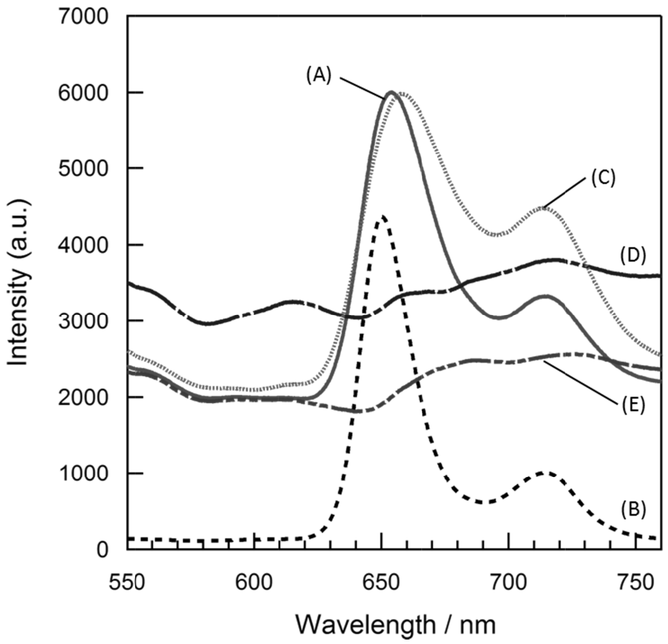

Figure 7. Photoluminescence spectra of (A) TCPP–TiO_2–IMP, (B) TCPP in methanol, (C) TCPP–SiO_2–IMP, (D) TCPP–TiO_2–MIX, and (E) TCPP powder. The excitation wavelength was 410 nm. The spectra of (A), (C), (D), and (E) were measured at the voltage of photomultiplier tube of 700 V and spectrum (B) was of 450 V. Loading of TCPP was 12.5 μmol g^{-1}, and the concentration of TCPP in methanol was 1.0×10^{-6} mol L^{-1}.

On–off response tests of visible light irradiation

Fig. 8 shows the on–off response for the photo-SCR under visible-light irradiation over the TCPP-TiO_2 photocatalyst at a GHSV of 50,000 h^{-1}. The conversion of NO was about 6% without visible-light irradiation. The conversion of NO significantly increased to 86.5% under visible-light irradiation, indicating the function of the TCPP-TiO_2 photocatalyst as a visible-light-driven photocatalyst for the photo-SCR. The conversion of NO gradually decreased to 81.2% with the increasing irradiation time, although the conversion was restored to the original level (85.5%) after the on–off action. The decrease in the conversion of NO with the irradiation time was not due to the decomposition of TCPP. If the TCPP on the TiO_2 surface was decomposed under visible-light irradiation, the initial conversion of NO was expected to decrease gradually in the second, third, and fourth times. However, we did not observe a decrease in the initial conversion of NO. The recovery of the initial conversion of NO took place reversibly.

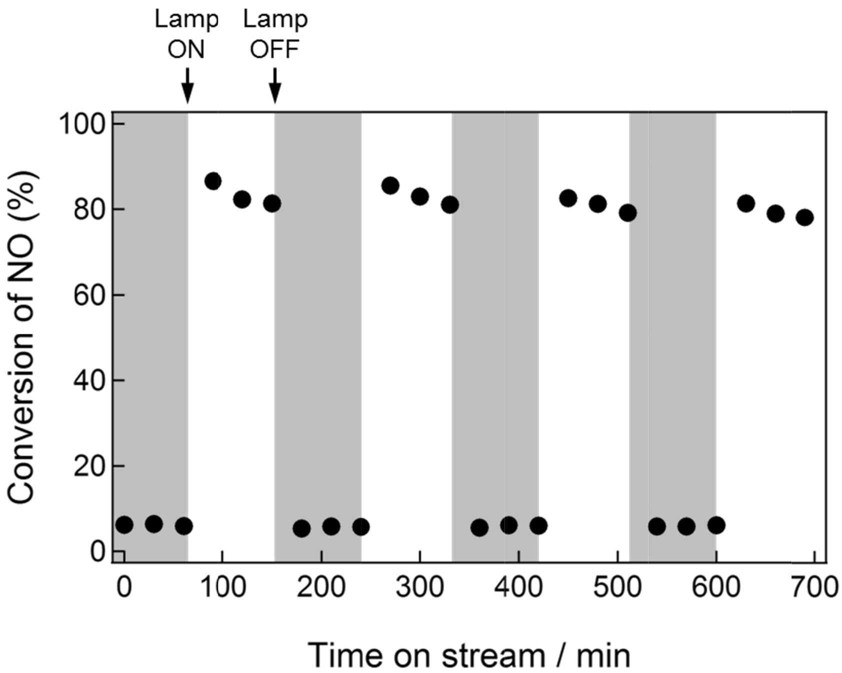

Figure 8. Conversion of NO during several on/off cycles of visible–light irradiation over the TCPP/TiO_2 photocatalyst: each cycle consisted of two–hours light on and off (TCPP loading: 12.5 μmol g^{-1}, catalyst amount: 110 mg, NO: 1000 ppm, NH_3: 1000 ppm, O_2: 2 %, GHSV: 50,000 h^{-1}).

Conclusions

We found that porphyrin derivative-modified TiO_2 functions as a visible-light-driven photocatalyst for the photo-SCR. The TCPP-modified TiO_2 photocatalyst showed the highest activity of the photo-SCR among the TiO_2 photocatalysts modified with the five porphyrin derivatives investigated. We elucidated the state of TCPP on TiO_2 affect the photocatalytic conversion of NO and the active species is a TCPP monomer adsorbed on TiO_2 due to efficient electron transfer from the photo-excited TCPP monomer to the conduction band of TiO_2.

References

[1] H. Bosch, F. Janssen, *Catal. Today* **1988**, *2*, 369-379.

[2] G. Busca, L. Lietti, G. Ramis, F. Berti, *Appl. Catal. B* **1998**, *18*, 1-36.

[3] P. Forzatti, L. Lietti, *Heterog. Chem. Rev.* **1996**, *3*, 33-51.

[4] R. Q. Long, R. T. Yang, R. Chang, *Chem. Commun.* **2002**, 452-453.

[5] J. Li, H. Chang, L. Ma, J. Hao, R. T. Yang, *Catal. Today* **2011**, *175*, 147-156.

[6] P. G. Smirniotis, D. A. Peña, B. S. Uphade, *Angew. Chem. Int. Ed.* **2001**, *40*, 2479-2482.

[7] T. Tanaka, K. Teramura, K. Arakaki, T. Funabiki, *Chem. Commun.* **2002**, 2742-2743.

[8] K. Teramura, T. Tanaka, S. Yamazoe, K. Arakaki, T. Funabiki, *Appl. Catal. B* **2004**, *53*, 29-36.

[9] S. Yamazoe, T. Okumura, K. Teramura, T. Tanaka, *Catal. Today* **2006**, *111*, 266-270.

[10] A. Yamamoto, Y. Mizuno, K. Teramura, T. Shishido, T. Tanaka, *Catal. Sci. Technol.* **2013**, *3*, 1771-1775.

[11] M. Koebel, M. Elsener, M. Kleemann, *Catal. Today* **2000**, *59*, 335-345.

[12] S. Yamazoe, K. Teramura, Y. Hitomi, T. Shishido, T. Tanaka, *J. Phys. Chem. C* **2007**, *111*, 14189-14197.

[13] T. Shishido, K. Teramura, T. Tanaka, *Catal. Sci. Technol.* **2011**, *1*, 541-551.

[14] A. Kay, M. Graetzel, *J. Phys. Chem.* **1993**, *97*, 6272-6277.

[15] W. M. Campbell, A. K. Burrell, D. L. Officer, K. W. Jolley, *Coord. Chem. Rev.* **2004**, *248*, 1363-1379.

[16] H. Imahori, H. Norieda, H. Yamada, Y. Nishimura, I. Yamazaki, Y. Sakata, S. Fukuzumi, *J. Am. Chem. Soc.* **2000**, *123*, 100-110.

[17] A. Yella, H.-W. Lee, H. N. Tsao, C. Yi, A. K. Chandiran, M. K. Nazeeruddin, E. W.-G. Diau, C.-Y. Yeh, S. M. Zakeeruddin, M. Grätzel, *Science* **2011**, *334*, 629-634.

[18] G. Mele, R. Del Sole, G. Vasapollo, E. García-López, L. Palmisano, M. Schiavello, *J. Catal.* **2003**, *217*, 334-342.

[19] S. Murphy, C. Saurel, A. Morrissey, J. Tobin, M. Oelgemöller, K. Nolan, *Appl. Catal. B* **2012**, *119–120*, 156-165.

[20] H. Hagiwara, N. Ono, T. Inoue, H. Matsumoto, T. Ishihara, *Angew. Chem. Int. Ed.* **2006**, *45*, 1420-1422.

[21] D. Li, W. Dong, S. Sun, Z. Shi, S. Feng, *J. Phys. Chem. C* **2008**, *112*, 14878-14882.

[22] A. A. Ismail, D. W. Bahnemann, *ChemSusChem* **2010**, *3*, 1057-1062.

[23] M. Gouterman, *J. Mol. Spectrosc.* **1961**, *6*, 138-163.

[24] N. C. Maiti, S. Mazumdar, N. Periasamy, *J. Phys. Chem. B* **1998**, *102*, 1528-1538.

[25] M. Kasha, H. R. Rawls, M. A. El-Bayoumi, *Pure Appl. Chem.* **1965**, *11*, 371-392.

[26] S. Cherian, C. C. Wamser, *J. Phys. Chem. B* **2000**, *104*, 3624-3629.

[27] N. C. Maiti, M. Ravikanth, S. Mazumdar, N. Periasamy, *J. Phys. Chem.* **1995**, *99*, 17192-17197.

[28] M. Gouterman, G.-E. Khalil, *J. Mol. Spectrosc.* **1974**, *53*, 88-100.

[29] S. Verma, A. Ghosh, A. Das, H. N. Ghosh, *J. Phys. Chem. B* **2010**, *114*, 8327-8334.

Chapter 3

Visible-Light-Assisted Selective Catalytic Reduction of NO with NH_3 over Dye-Modified TiO_2 Photocatalysts

Abstract

Dye-modified TiO_2 photocatalysts showed high photocatalytic activity for the selective catalytic reduction of NO with NH_3 in the presence of O_2 under visible-light irradiation. Among the 15 dyes investigated, the maximum conversion was achieved using a Ru(2,2'-bipyridyl-4,4'-dicarboxylic acid)$_2$(NCS)$_2$ complex (N3-dye) for the modification of TiO_2 (NO conversion > 99%, N_2 selectivity > 99%). Diffuse reflectance infrared Fourier transform (DRIFT) investigation showed that nitrite (NO_2^-) and nitrate (NO_3^-) species were generated on the N3-TiO_2 surface under visible-light irradiation. In gas switch reactions, NO_2^- on the N3-TiO_2 surface became N_2 by a reaction with adsorbed NH_3 under visible-light irradiation, although NO_3^- reacted with NH_3 to form N_2 and N_2O. Based on the relativity with NH_3, we concluded that the NO_2^- species is an intermediate in photo-SCR and reacts with NH_3 adsorbed on the surface of N3-TiO_2 under visible-light irradiation to selectively form N_2.

Introduction

Nitrogen oxides (NO_x) are air pollutants and cause serious environmental problems, including acid rain and town smog. In NO_x emission from heavy-duty diesel engines for trucks and buses, selective catalytic reduction (SCR) technology with urea is used to remove the NO_x in the exhaust gas.[1] In the SCR system, the injected urea decomposes to NH_3 and CO_2, and the formed NH_3 reduces NO to harmless N_2 according to eq. 1.

$$4NO + 4NH_3 + O_2 \rightarrow 4N_2 + 6H_2O \qquad (1)$$

V_2O_5-based catalysts[2-4] and Fe- or Cu-zeolite catalysts[5-8] are used for the SCR process and these catalysts effectively decomposes the NO_x.

Regulations in NO_x emission have become stricter step by step, and further improvements of the de-NO_x systems are required to meet the future regulations.[9] The world harmonized transient cycle (WHTC) tests were introduced in Euro VI regulation (2014) for the heavy-duty diesel engines to simulate in-use driving conditions; in the WHTC, the NO_x emission is monitored in transident situations including a cold start.[10] However, in the SCR system, urea cannot be injected because of the low activity of the catalysts during the cold start condition (< 473 K).[10] Thus, novel technology is strongly desired to remove the NO_x at low temperatures.

Utilizing photocatalysis is an effective way in terms of such a low temperature operation. We have reported photocatalysts that show activity for NH_3-SCR at low temperatures in the presence of excess O_2 (referred to as photo-SCR).[11-14] The reaction mechanism of photo-SCR has been investigated by us and other groups using spectroscopic,[15-16] kinetic,[12, 17-18] and theoretical[19] methods. Over TiO_2 photocatalyst, the conversion of NO and the selectivity to N_2 becomes 90% and 99%, respectively, at a gas hourly space velocity (GHSV) of 8000 h^{-1}, which is sufficient for the De-NO_x process in typical stationary sources such as power plants, blast furnaces, and incinerators. However, higher GHSV values (>50,000 h^{-1}) are required in engines owing to the limited installation space of the De-NO_x process and a high flow rate of the exhaust gas.

Recently, we reported that porphyrin-sensitized TiO_2 functions as a visible-light-sensitive photocatalyst for NH_3-SCR.[20] In the porphyrin-sensitized TiO_2 system, maximum conversion of NO was 79% at a GHSV of 50,000 h^{-1} under visible-light irradiation. However, the improvement of the activity at the higher GHSV of 100,000 h^{-1} is essential from the practical application viewpoint. This reaction proceeds via electron injection from photo-excited dyes into the conduction band of TiO_2 (dye-sensitization mechanism),[20] although a detailed mechanism of the reaction is unclear. The electron injection process from photo-excited dyes into the conduction band of a semiconductor is an important step in dye-sensitized solar cells (DSSCs)[21-23] and dye-sensitized photocatalysts,[24-27] and has been previously investigated.[28-30] Many researchers have tested various dyes, including Ru complexes,[31-34] porphyrins,[35-41] phthalocyanines,[42-45] and other organic dyes,[22, 26, 46-47] to improve the performance of DSSCs and dye-sensitized photocatalysts. The type of dye used for the modification of semiconductors has a great impact on the performance of DSSCs and dye-sensitized photocatalysts, and thus, should have a significant effect on the activity in photo-SCR under visible-light irradiation. A major problem of the dye-sensitization system is the stability of the dyes; moreover, optimization of the dye is essential to evaluate and improve the performance of photo-SCR over dye-modified TiO_2 photocatalysts. Herein, we investigated photo-SCR under visible-light irradiation using TiO_2 photocatalysts modified with 15 different dyes (Fig. 1) to improve the activity of this photocatalytic system. The reactivity of the adsorbed intermediates generated over the dye-modified TiO_2 photocatalyst were also investigated by means of *in situ* diffuse reflectance infrared Fourier transform (DRIFT) and UV–Vis diffuse reflectance (DR) spectroscopies to elucidate the reaction mechanism.

Experimental

Catalyst Preparation

All dyes were used without further purification, and their structures are shown in Fig. 1. The dyes were impregnated on a TiO_2 powder (ST-01, anatase, 273 m^2 g^{-1}), purchased from Ishihara Sangyo Kaisha, Ltd., using appropriate solvents (Table 1). Sodium nitrite ($NaNO_2$) and sodium nitrate ($NaNO_3$) were impregnated on the N3-dye-modified photocatalyst using water as the solvent (loading of $NaNO_2$ or $NaNO_3$: 1000 μmol g^{-1}).

Photocatalytic reaction

Photo-SCR was carried out in a conventional fixed-bed flow system at atmospheric pressure, the details of which we have previously reported.[12, 20] In brief, two types of a quartz reactor were used in this research: reactor 1 (12 mm × 10 mm × 1.0 mm, catalyst amount: 110 mg) for a GHSV of 100,000 and 250,000 h^{-1}, and reactor 2 (50 mm × 15 mm × 1.0 mm, catalyst amount: 420 mg) for a GHSV of 8000 h^{-1}. The reaction gas (NO 1000 ppm, NH_3 1000 ppm, O_2 2%, He balance) was introduced to the reactors at a flow rate of 100–500 mL min^{-1}. A 300 W Xe lamp (PERKIN-ELMER PE300BF) equipped with an L42 cut-off filter was used as a light source ($\lambda > 400$ nm). N_2 and nitrous oxide (N_2O) were analyzed using two SHIMADZU GC-8A TCD gas chromatographs.

Characterization

In situ DRIFT measurements were performed with a JASCO ISDR-600 FTIR spectrometer equipped with a mercury-cadmium-tellurium (MCT) detector cooled by liquid N_2 at a resolution of 4 cm^{-1} and with 16 co-added scans. The sample powder (50 mg) was placed in a DR cell, which was fitted with a KBr window at the top. The catalyst was pretreated at 353 K under a He gas flow (100 mL min^{-1}) for 1 h, and was then cooled to room temperature. Concentrations of gases were the same as in the reaction. The background spectrum was measured after the pretreatment in a He gas flow at room temperature. A 200 W Hg–Xe lamp equipped with a collective lens (San-Ei Electric Co. Ltd., UVF-204S type C) was used as a light source, and light was irradiated through an L42 cut-off filter. UV–Vis DR spectra were measured using a UV–Vis spectrometer (JASCO V-650) with an integrating sphere. A $BaSO_4$ plate was used as a reference. A sample powder was added to a quartz cell with flat facets and evacuated at 373 K for 1 h before the measurement. Cl_2 and NH_3 gas were added to the cell using a vacuum line.

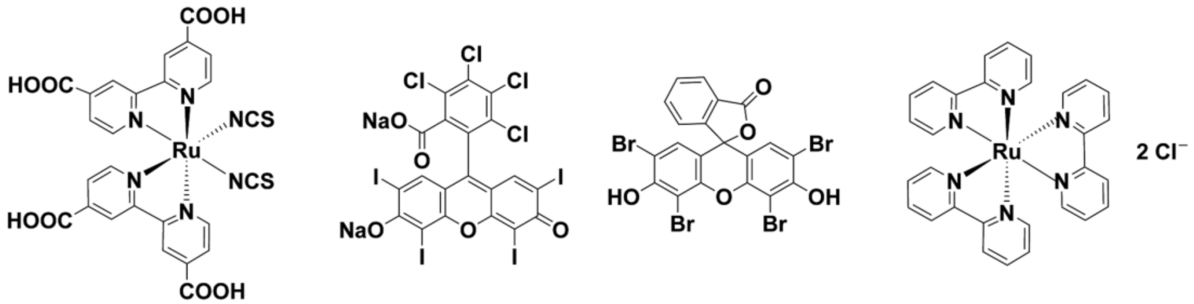

N3 dye (**1**) | Rose bengal (**2**) | Eosin Y (**3**) | $Ru(bpy)_3Cl_2$ (**4**)

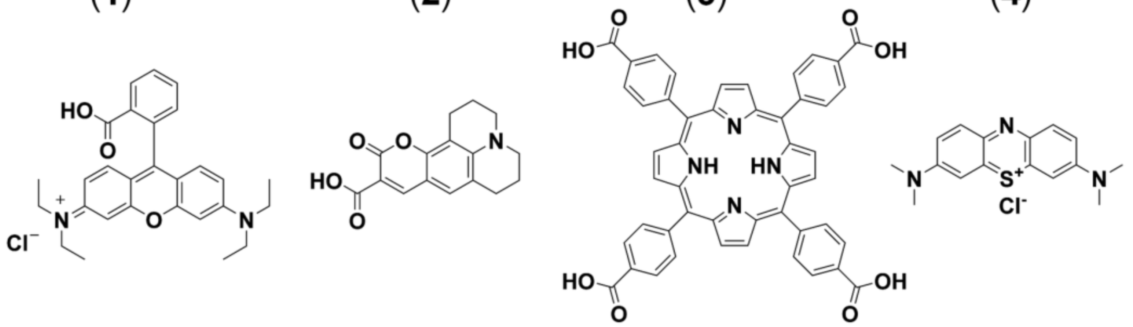

Rhodamine B (**5**) | Coumarin 343 (**6**) | TCPP (**7**) | Methylene blue (**8**)

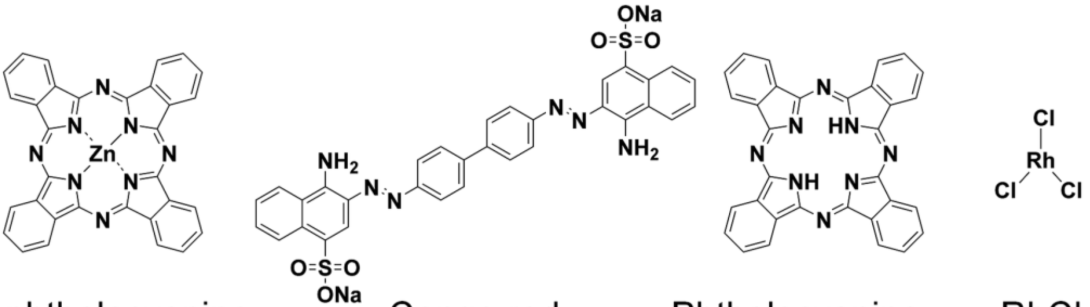

Zn phthalocyanine (**9**) | Congo red (**10**) | Phthalocyanine (**11**) | $RhCl_3$ (**12**)

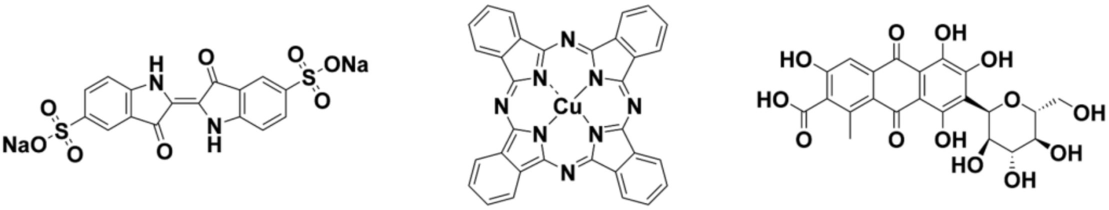

Indigo carmine (13) | Cu phthalocyanine (**14**) | Carmine (**15**)

Figure 1. Schematic representation of dyes

Table 1. Solvents used for the impregnation

Entry	Dye	Solvent used for the impregnation
1	N3-dye [a]	Methanol
2	Rose bengal	Methanol
3	Eosin Y	Methanol
4	$Ru(bpy)_3Cl_2$	Methanol
5	Rhodamine B	Methanol
6	Coumarin 343	Methanol
7	TCPP [b]	Methanol
8	Methylene blue	Methanol
9	Zn phthalocyanine	Trifluoroacetic acid
10	Congo red	Water
11	Phthalocyanine	Trifluoroacetic acid
12	$RhCl_3$	Water
13	Indigo carmine	Water
14	Cu phthalocyanine	Trifluoroacetic acid
15	Carmine	10 mmol L^{-1} NaOH aq.

[a] Ru(4,4'-dicarboxy-2,2'-bipyridine)$_2$(NCS)$_2$

[b] Tetrakis(4-carboxyphenyl)porphyrin

Results and discussion

Screening of dyes

Fig. 2 shows the results of photo-SCR over dye-modified TiO_2 photocatalysts. The reaction proceeded to some extent (ca. 5%) over a bare TiO_2 photocatalyst under visible-light irradiation, as reported in the previous paper.[48] Modification of TiO_2 with various dyes greatly enhanced photo-SCR activities. The maximum conversion of NO (>99%) was obtained using an N3-dye (**1** in Fig. 1)-modified TiO_2 photocatalyst (N3-TiO_2) after 30 min. The conversion of NO was significantly higher than those of other photocatalysts (e.g., UV-light irradiated TiO_2)[14, 20] and conventional catalysts (e.g., Fe- and Cu-zeolite catalysts)[49] at low temperatures. N_2O was not detected in all reactions shown in Fig. 2. The high selectively to N_2 is consistent with our previous reports of photo-SCR over porphyrin-modified TiO_2 photocatalysts under visible-light irradiation.[20] The order of activities is discussed in the last section.

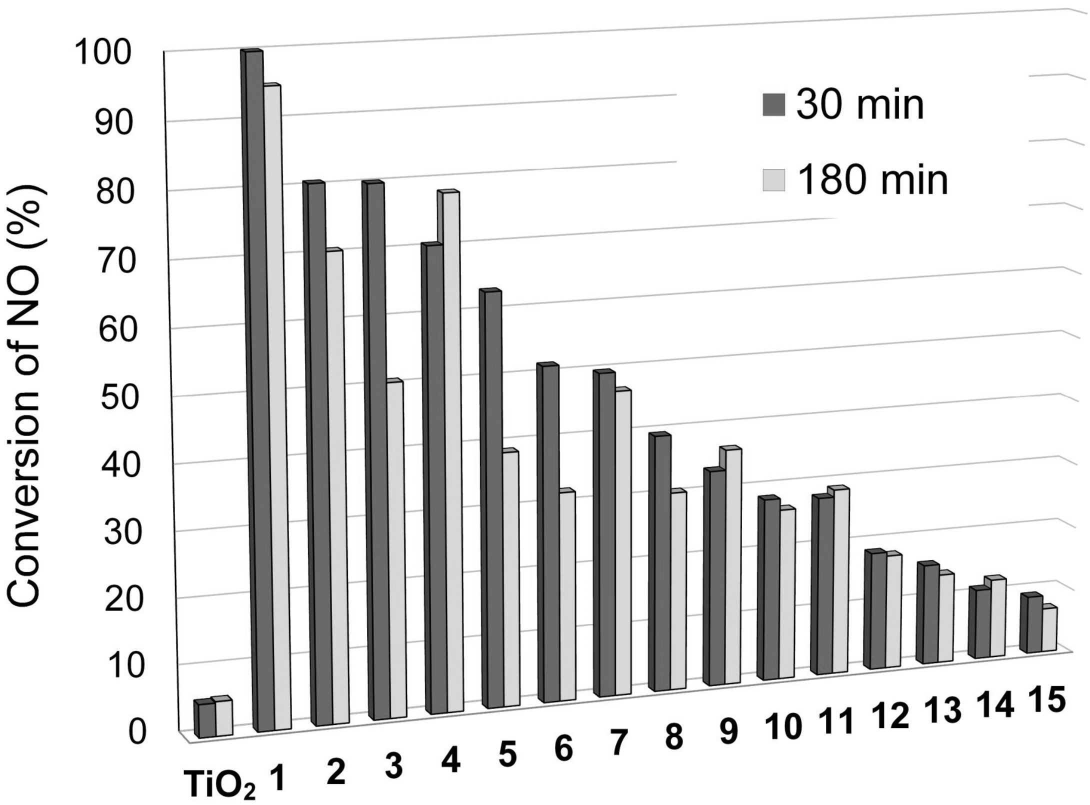

Figure 2. Conversion of NO in photo-SCR over the dye-modified TiO_2 photocatalysts under visible-light irradiation. Dye loading: 12.5 μmol g^{-1}. GHSV: 100,000 h^{-1}. The numbers in the bottom axis correspond to those in Fig.1.

In TCPP-TiO_2 (**7**), conversion of NO was 50% at 30 min of the reaction, and the decrease of the conversion was hardly observed during 180 min (Fig. 3). The high stability of TCPP agreed with the previous reports.[20] When xanthene dyes were used, relatively high conversions of NO were obtained after 30 min: rose bengal **2** (81%), eosin Y **3** (80%), and rhodamine B **5** (63%). However, the conversions gradually decreased during 180 min of the reaction (Fig. 3). Bleaching of the catalyst colors was observed after the reaction, which suggested that the decrease of the activity was due to dye decomposition. The low stability of xanthene dyes was consistent with the previously reported DSSCs.[22, 50] Thus, the xanthene dyes were deemed unsuitable for photo-SCR. In $Ru(bpy)_3Cl_2$ **4**, and phthalocyanines (**9**, **11**, and **14)**, the conversions of NO at 180 min were higher than those at 30 min although the color bleaching was observed in these dyes after the reaction. A relatively high stability was observed in N3-dye **1** despite the presence of O_2, and the N3-TiO_2 photocatalyst showed the highest conversion of NO even at 180 min (95%) as shown in Fig. 3. Although the breaching of the catalyst color was also observed in N3-TiO_2 after the reaction, the total amount of generated N_2 reached to 1.4 mmol for 3 h, and the turnover number (TON) of N3-dye was calculated to be 1000 after 3 h of the reaction. As a result of the screening of dyes, N3-dye showed the highest activity and relatively high stability in photo-SCR under a practical GHSV condition.

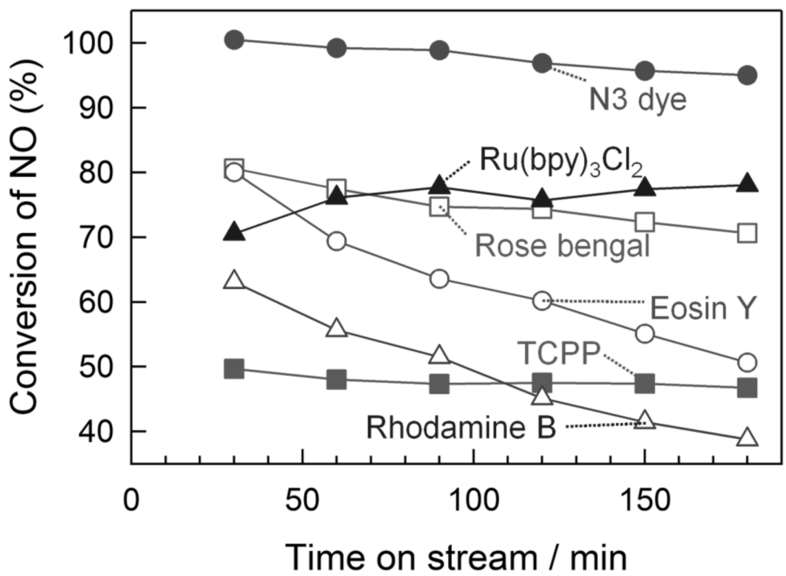

Figure 3. Time course of the conversion of NO in photo-SCR over the dye-modified TiO_2 photocatalysts under visible-light irradiation. Dye loading: 12.5 μmol g^{-1}. GHSV: 100,000 h^{-1}.

Optimization of the catalyst preparation conditions

Effect of loading of N3-dye on the activity was investigated at a GHSV of 250,000 h^{-1} (Fig. 4). The conversion of NO drastically increased up to 37.5 μmol g^{-1}, and then slightly decreased. The maximum conversion of NO was 63% after 30 min of the reaction. The tendency of the activity to the dye loading was similar to the porphyrin-TiO_2 system in our previous reports although the optimized loading of N3-dye was larger than that of TCPP-TiO_2 (12.5 μmol g^{-1}).[20] Fig. 5 shows the effect of the solvent used in the impregnation on the conversion of NO. As a result of the optimization, methanol was found to be the most effective solvent for the impregnation. Ru-K edge XANES spectra were measured using 37.5 μmol g^{-1} N3-TiO_2 catalysts prepared using various solvents. The edge energies of all the spectra of N3-TiO_2 catalysts (a–d) were the same as that of the reference pellet of N3-dye (e), and were completely different from that of Ru foil. This result indicates the valence of Ru in all the N3-TiO_2 catalysts was +2. There was no change in the shapes of the spectra of N3-TiO_2 catalysts and N3-dye (a–e). In our previous research, the aggregation of dyes drastically decreased the activity.[20] The solvents used in the impregnation may affect the aggregation state of N3-dye and change the photocatalytic activity observed in Fig. 5.

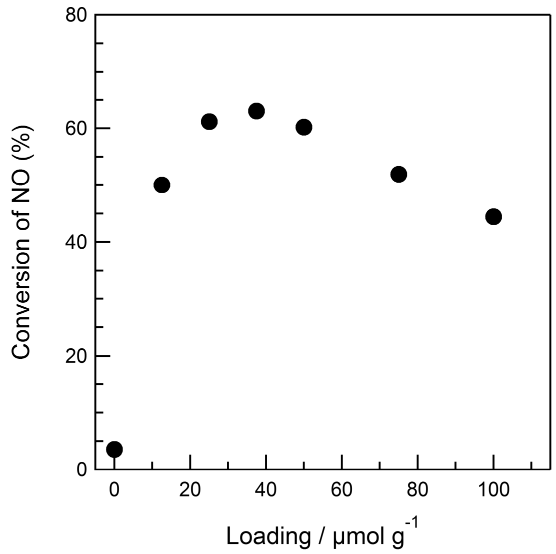

Figure 4. Effect of loading of N3-dye on the acivity. GHSV: 250,000 h^{-1}. The data were obtained after 30 min of the reaction.

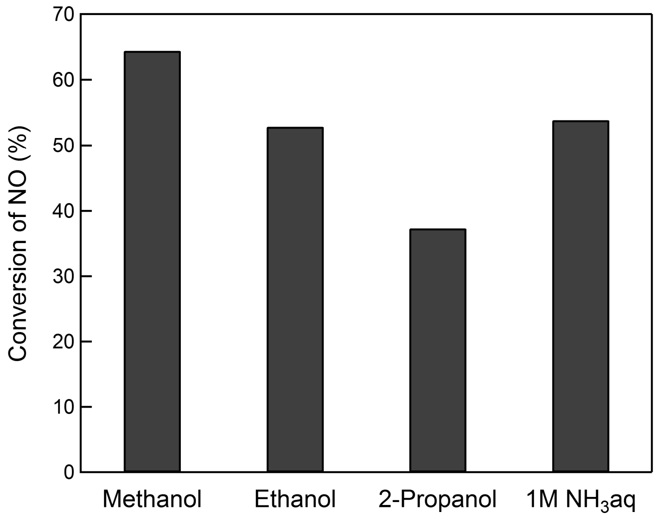

Figure 5. Effect of the solvents used in the impregnation on the activity. N3-dye loading: 37.5 μmol g^{-1}, GHSV: 250,000 h^{-1}. The data were obtained after 30 min of the reaction.

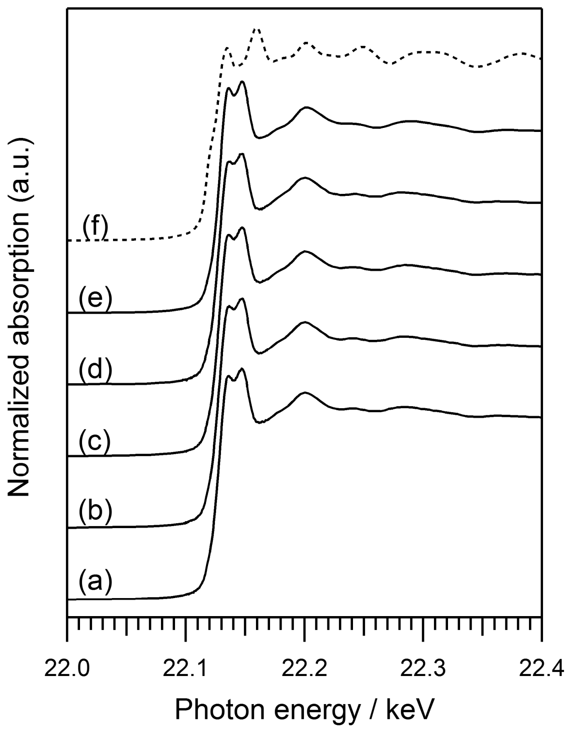

Figure 6. Rh-K edge XANES spectra of 37.5 μmol g^{-1} N3-TiO_2 prepared by impregnation using (a): methanol, (b) ethanol, (c) 2-propanol, and (d) 1 M NH_3 aq., and reference samples. (e): N3-dye, and (f) Ru foil.

Reactivity of adsorbed species of NH_3 and NO

Table 2 lists the results of reactions under various conditions. Efficient N_2 formation was observed over N3-TiO_2 in the presence of NO, NH_3, and O_2 under visible-light irradiation (640 ppm, Entry 2). The activity of N3-TiO_2 was significantly higher than that of the TiO_2 photocatalyst under UV and visible light irradiation (290 ppm, Entry 1). Product formation was greatly diminished without NO, NH_3, or O_2 (Entries 3, 4, and 5), which indicated that all the gases are involved in the formation of N_2. Furthermore, visible-light irradiation drastically promoted photo-SCR over N3-TiO_2 (Entry 6).

Table 2. Results of photo–SCR under various reaction conditions.

Entry	Catalyst	Inlet (%)[a]			Lamp[b]	Outlet (ppm)[c]	
		NO	NH_3	O_2		N_2	N_2O
1	TiO_2	0.1	0.1	2	UV+Vis.	290	4
2	N3-TiO_2[d]	0.1	0.1	2	Vis.	640	n.d.[e]
3	N3-TiO_2[d]	0	0.1	2	Vis.	14	n.d.[e]
4	N3-TiO_2[d]	0.1	0	2	Vis.	10	n.d.[e]
5	N3-TiO_2[d]	0.1	0.1	0	Vis.	35	7
6	N3-TiO_2[d]	0.1	0.1	2	OFF	15	n.d.[e]
7	N3-SiO_2[d]	0.1	0.1	2	Vis.	16	n.d.[e]

[a] Concentration of N_2 and N_2O in the inlet gas. [b] Light source, UV+Vis: 300 W Xe lamp without cut-off filter, Vis: 300 W Xe lamp with L-42 cut-off filter. [c] Concentration of N_2 and N_2O in the outlet gas. GHSV: 250,000 h^{-1}, total flow rate: 500 ml min^{-1}, catalyst amount: 110 mg. [d] Loading of N3-dye: 37.5 μmol g^{-1}. [e] Not detected.

A couple of gas switch experiments were carried out to investigate the reactivity of the adsorbed species of NH_3 and NO on the N3-TiO_2 surface. In the first experiment, NH_3/He gas was flowed in the first 120 min in the dark (Fig. 7A), and no product was observed. Subsequently, the feed gas was switched to NO/O_2/He gas and visible-light irradiation was started. Selective formation of N_2 (910 ppm, selectivity to N_2 > 99%) was observed after 5 min of visible-light irradiation. The concentration of N_2 in the outlet gas gradually decreased with increasing visible-light irradiation time and dropped to 24 ppm after 270 min. This formation of N_2 presumably derived from the reaction between the initially adsorbed NH_3 and NO in the gas phase, because low amount of N_2 were formed via a reaction of NO and O_2 under visible-light irradiation (Table 2, Entry 4). The above gas switch reaction clearly showed the adsorbed NH_3 was involved in the reaction.

In the second experiment, NO/O_2/He gas was flowed under visible-light irradiation for 90 min, and then the feed gas was switched to NH_3/He gas in the dark (Fig. 7B). During this period, a small amount of N_2 was formed and N_2O was not detected. After 120 min of the NH_3/He gas flow in the dark, visible-light irradiation was started and N_2 (780 ppm) and N_2O (130 ppm) were observed (selectivity to N_2: 86%) after 5 min; the concentrations gradually decreased as the irradiation time was increased. The blank test results showed that NH_3 did not decompose to N_2 over N3-TiO_2 under visible-light irradiation (Table 2, Entry 3). Thus, the generation of N_2 and N_2O was due to the reaction between NO_x species generated on a N3-TiO_2 surface and NH_3 molecules.

The couple of gas switch experiments revealed that the adsorbed two species (i.e., NH_3 and NO_x) were involved in the reaction. In addition, the reaction did not proceed without visible-light irradiation, which indicated that visible-light was essential for this surface reaction between NH_3 and NO_x species. Accordingly, we concluded that the adsorbed NH_3 and surface NO_x speices reacted under visible-light irradiation to form N_2 and N_2O.

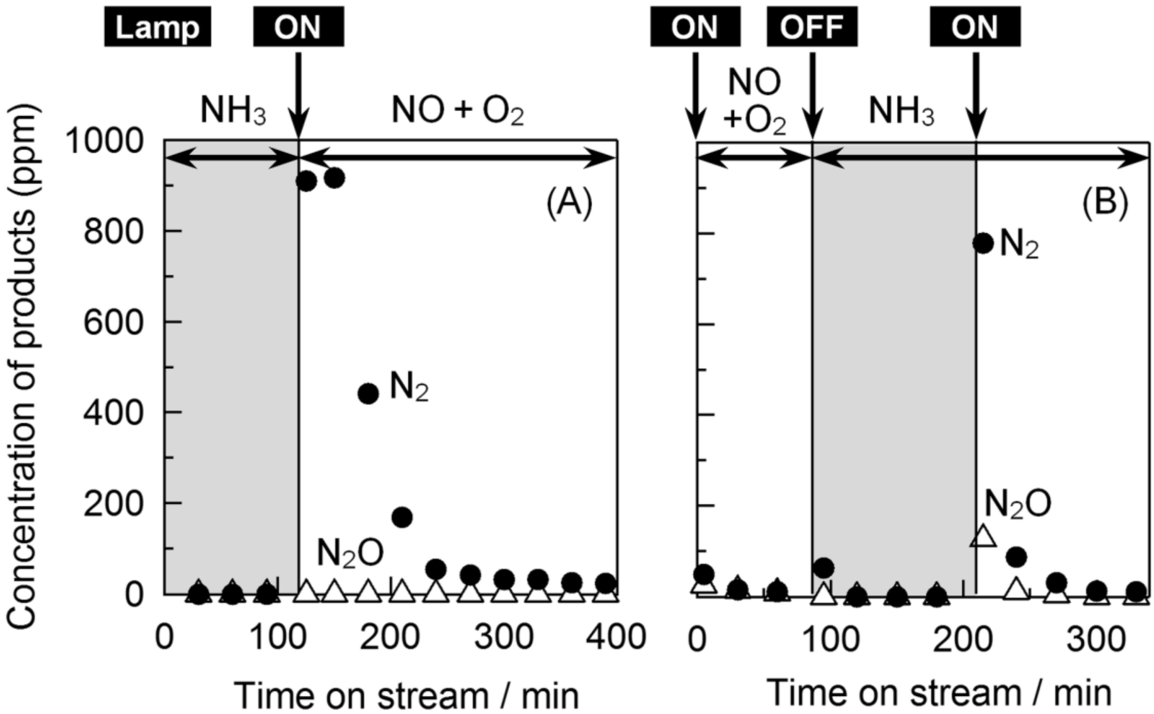

Figure 7. Time course of concentration of N_2 and N_2O in the outlet gas in the gas switch reactions. Catalyst: 37.5 μmol g^{-1} N3-TiO_2, NO: 1000 ppm, NH_3: 1000 ppm, O_2: 2 %, He: balance. GHSV: 8000 h^{-1}, Light source: 300 W Xe lump equipped with a L42 cut-off filter.

DRIFT investigations of surface NO_x species

Fig. 8 represents the DRIFT spectra before and after the addition of NO/O_2/He gas in the dark. The spectrum before the addition was used as the baseline. Two peaks, at 1478 and 1198 cm^{-1}, gradually increased with increasing the exposure time (Fig. 8A). The peak at 1478 cm^{-1} was assigned to a ν_3 vibration of monodentate NO_2^- adsorbed on the surface of N3-TiO_2. This species is also expected to have a ν_1 vibration band between 1065 and 1050 cm^{-1}.[51-52] In the DRIFT experiment, a shoulder band was observed around that region, which supports its proposed generation. The peak at 1198 cm^{-1} was assigned to a bridged bidentate NO_2^- in a previous paper.[51-52] Three negative peaks at 3697, 3659, and 3631 cm^{-1}, and a broad positive peak around 3500 cm^{-1} appeared after the addition of NO/O_2/He gas (Fig. 8B). The negative peaks were assigned to isolated OH groups in different surroundings (e.g., number of coordinated Ti atom, valence of coordinated Ti atom, surface sites of TiO_2)[53-54] and the broad positive peak was attributed to a hydrogen-bonded OH group. We did not observe a characteristic band of deformation vibration of water molecules around 1640 cm^{-1}, which indicated that the amount of adsorbed water did not change by the co-adsorption of NO and O_2. Thus, the increase of the band intensity centered at 3500 cm^{-1} is not due to the adsorption of water molecules generated. The change in the OH region suggests that the adsorbed NO_2^- species interacted with the isolated OH groups through hydrogen bonding, thus reducing the band intensities of the isolated OH groups and increasing the hydrogen-bond-related band intensity. Both NO_2^- species (monodentate and bridged bidentate) were generated on the surface of N3-TiO_2 by the co-adsorption of NO and O_2 in the dark.

After 30 min of NO/O_2 gas flow, O_2/He gas was introduced to the DRIFT cell, and then visible-light irradiation was started across the KBr window. As shown in Fig. 9A, the band at 1478 cm^{-1} decreased with visible-light irradiation, which indicated that the NO_2^- species were consumed by the reaction with O_2 under visible-light irradation. New bands at 1605, 1583, 1297, and 1253 cm^{-1} increased with increasing irradiation time. Bands at 1605 and 1253 cm^{-1} were attributed to a v_3 vibration of the bridging bidentate nitrate (NO_3^-), and a set of bands at 1583 and 1297 cm^{-1} was assigned to the chelating bidentate NO_3^-.[51-52] Thus, the NO_2^- species was oxidized into the NO_3^- species under visible-light irradiation. In the OH region (Fig. 9B), the isolated OH bands at 3697, 3659, and 3631 cm^{-1} decreased with visible-light irradiation, suggesting that the surface OH groups reacted with the adsorbed NO_2^- to form NO_3^-. The DRIFT investigation revealed that the NO_2^- species appeared after the co-adsorption of NO and O_2 in the dark, and were oxidized into NO_3^- by O_2 under visible-light irradiation (Scheme 1).

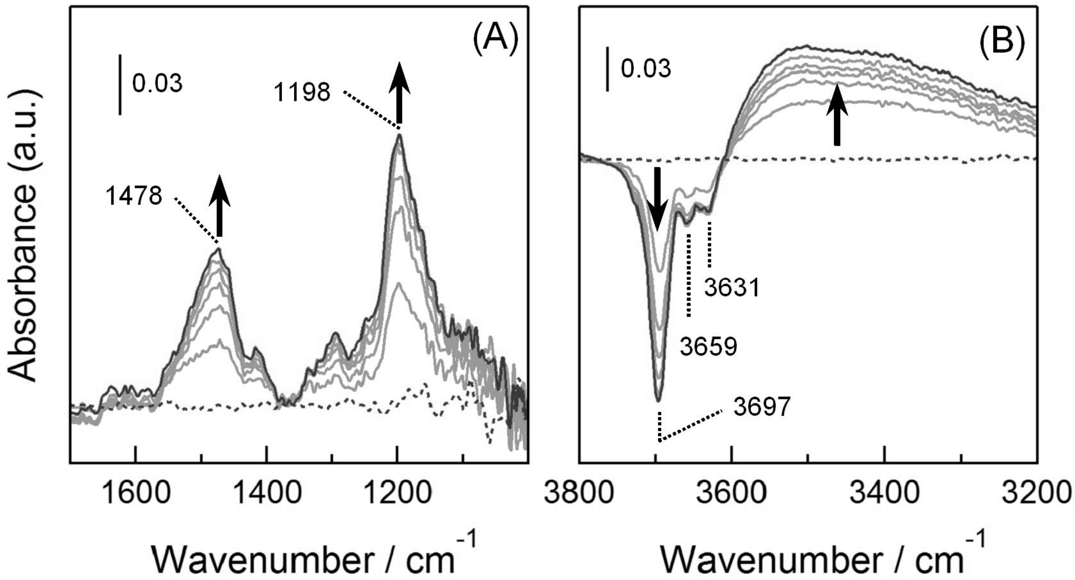

Figure 8. DRIFT spectra of N3-TiO_2 in the dark before addition of NO/O_2/He gas (dotted line), and after 5, 10, 15, 20, 25 (grey lines), and 30 min (black line).

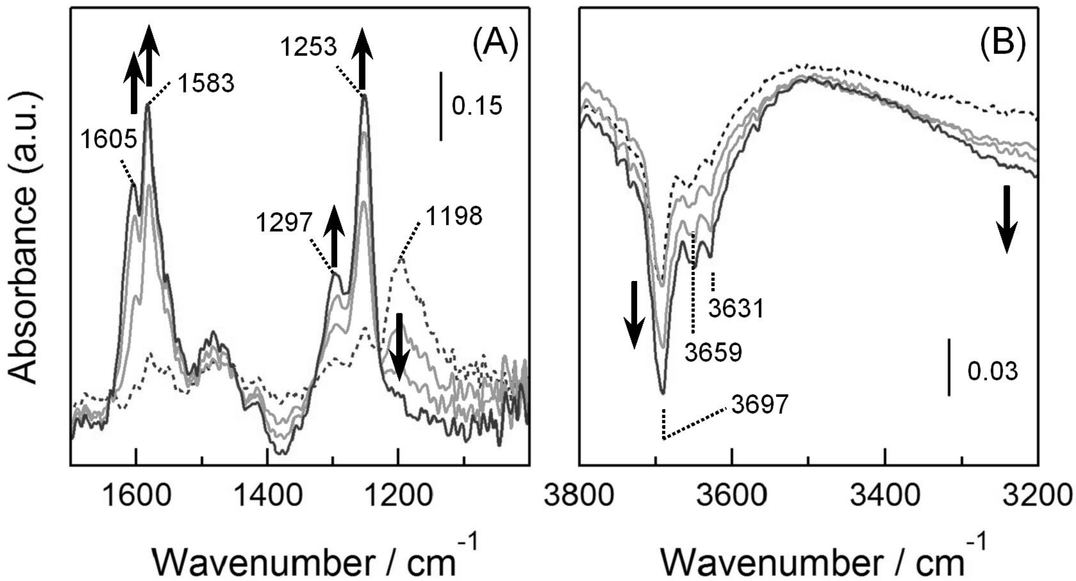

Figure 9. DRIFT spectra of N3-TiO_2 in O_2/He gas before visible-light irradiation (dotted line), and after 20 min, 40 min (grey lines), and 60 min (black line) from the start of visible-light irradiation.

Reactivity of the NO_2^- and NO_3^- species with NH_3 under visible-light irradiation.

Either $NaNO_2$ or $NaNO_3$ was impregnated over N3-TiO_2 in order to investigate the reactivity of NO_2^- and NO_3^- on the surface of N3-TiO_2. NH_3 was flowed into the reactor filled with the $NaNO_3$- or $NaNO_2$-impregnated catalysts (Fig. 10). In the dark, N_2 and N_2O were not detected in an NH_3/He gas flow for both catalysts. For the $NaNO_3$-impregnated N3-TiO_2, N_2 (2020 ppm) and N_2O (1420 ppm) were observed after 5 min of visible-light irradiation. Not much N_2 was observed in the NH_3/He gas flow under visible-light irradiation in the blank tests (Table 2, Entry 3). Thus, the generated N_2 shown in Fig. 10A is derived from a reaction between NH_3 in the gas phase and NO_3^- species on the surface of N3-TiO_2. Surprisingly, a large amount of N_2O was detected in this experiment (selectivity to N_2 = 59%). In contrast, selective formation of N_2 was observed from the $NaNO_2$-impregnated N3-TiO_2 under visible-light irradiation (Fig. 10B, selectivity to N_2 = 94%), which suggested that NO_2^- became N_2 on reacting with NH_3. As shown above, the reactivity of NO_2^- with NH_3 was significantly different from that of NO_3^- in terms of selectivity to N_2 (Scheme 1), which could explain the relatively low selectivity to N_2 (selectivity to N_2 = 86%) in the gas switch reaction shown in Fig. 7B; both the NO_2^- and NO_3^- species were formed in NO/O_2/He gas under visible-light irradiation on the surface of N3-TiO_2 and reacted with NH_3. High selectivity to N_2 (>99%) in photo-SCR in the presence of NO, NH_3, and O_2 (Table 2, Entry 2) over N3-TiO_2 strongly indicated that an intermediate in photo-SCR was NO_2^- was adsorbed on the surface of N3-TiO_2 on the basis of the difference in their reactivity.

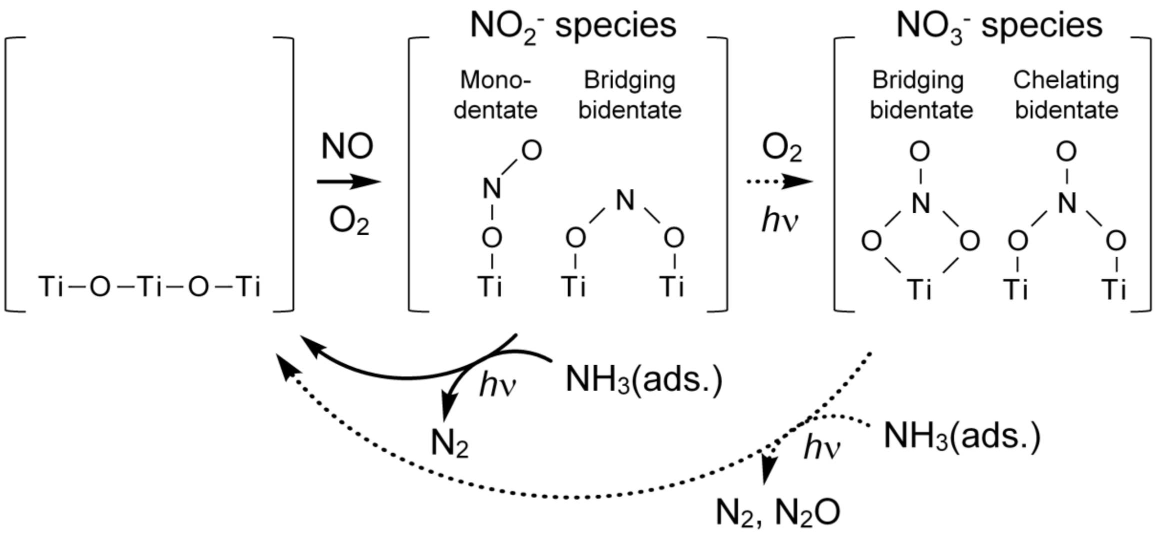

Scheme 1. Surface NO_x species on N3-TiO_2 catalyst and its reactivity with NH_3 under visible light irradiation.

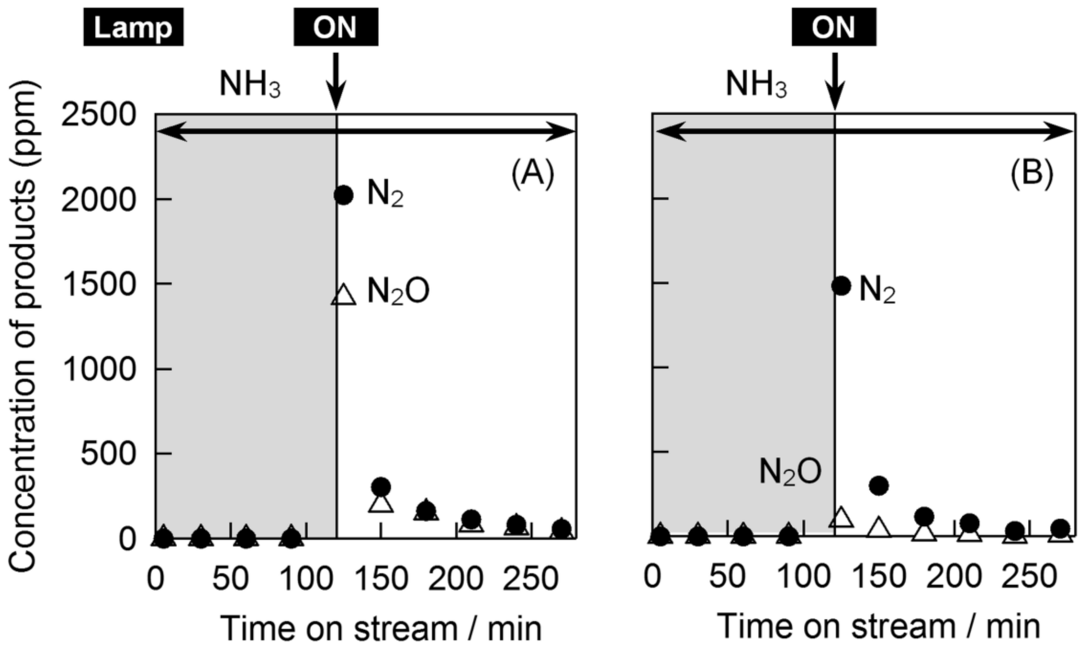

Figure 10. Time course of concentration of N_2 and N_2O in the outlet gas over (A) $NaNO_3$-imprignated N3-TiO_2 and (B) $NaNO_2$-imprignated N3-TiO_2. Loading of $NaNO_3$ or $NaNO_2$: 1000 μmol g^{-1}. Loading of N3-dye: 37.5 μmol g^{-1}, Reaction gas: 1000 ppm NH_3/He. GHSV: 8000 h^{-1}, light source: 300 W Xe lump equipped with a L42 cut-off filter.

Role of dyes.

As shown in Table 2, the activity of N3-SiO_2 catalyst was very low (conversion of NO: 1.6%, entry 7), which indicated that the N3-dye did not function independently of the support (i.e., TiO_2). Thus, the reaction over N3-TiO_2 proceeds via a dye-sensitization mechanism: visible-light irradiation induces the electron injection from photo-excited dyes to the conduction band of TiO_2. A similar result was obtained in porphyrin-modified TiO_2 photocatalysts.[20] After the electron injection, the oxidation product of N3-dye and an electron in the conduction band of TiO_2 should be generated as shown in eq. 2:

$$\text{N3-dye} + h\nu \rightarrow \text{N3-dye}^{+} + e^{-}_{cb} \qquad (2)$$

Based on eq. 2, we investigated the reactivity of the oxidation product of N3-dye with NH_3. In a previous report,[55] the one-electron oxidation product of $Ru^{2+}(bpy)_3$ (i.e., $Ru^{3+}(bpy)_3$) in zeolite was prepared using Cl_2 as an oxidant, and we attempted the corresponding oxidation of N3-dye. Fig. 11 shows the UV-Vis DR spectra of N3-dye. After evacuation, the catalyst color was the dark purple, and an absorption band at 515 nm was observed (a). The band is assigned to a MLCT band of the grand state N3-dye (Ru^{2+}). After addition of Cl_2, the catalyst color changed from dark purple into ocher, and the absorption peak was shifted to 420 nm (b). The band at 420 nm is not attributed to the one electron oxidation products (Ru^{3+}) of N3-dye because the one electron oxidation product have an adsorption band around 740 nm, which was observed in several transient adsorption experiments.[30, 56]

S. Das and P. V. Kamat[56] investigated the oxidized form of N3-dye by using transient absorption spectroscopy using azide (N3•) radical generated by γ-Radiolysis as an oxidant. Their results provided the spectral evidence for the formation of two different species that follow the oxidation of N3-dye. One oxidized product (species 1, abs. max: 740 nm) was attributed to the one-electron oxidation product of N3-dye, and is undergone further transformations to the other oxidized form (species 2, abs. max: 440 nm) at room temperature. The identification of species 2 was not made in their report. The ocher products (abs. max: 420 nm) observed in our UV-Vis DR experiments can be assigned to the species 2 judging from the position of adsorption maximum. To examine the reactivity of species 2, NH_3 was introduced to the cell. After addition of NH_3, the catalyst color changed into the initial dark purple as shown in Fig. 11c. This result clearly indicates that species 2 can react with NH_3 and returned to the initial ground state of N3-dye. Although the identification is not made and which oxidation products (species 1 or 2) activate NH_3 in the in situ reaction condition is unclear, the UV-Vis DR spectroscopy revealed that oxidized products (at least, species 2) of N3-dye have a potential to activate NH_3.

As discussed above, N3-dye$^+$ could not be prepared because of its instability. Therefore, we used the TiO_2 photocatalyst modified with $Ru^{2+}(bpy)_3Cl_2$ (**4** in Fig. 1) in the UV–Vis spectroscopic study and investigated the reactivity of one-electron oxidation products of $Ru^{2+}(bpy)_3$ with NH_3 (Fig. 12). After the evacuation of $Ru(bpy)_3Cl_2/TiO_2$, an adsorption band at 455 nm was observed (spectrum (a) in Fig. 12) and attributed to an MLCT band of $Ru^{2+}(bpy)_3$. After the addition of Cl_2, the catalyst color changed from light orange to slightly greyish orange and the adsorption at 600–800 nm increased (spectra (b)), which was assigned to an LMCT band of $Ru^{3+}(bpy)_3$.[55] As previously mentioned, $Ru^{3+}(bpy)_3$ was successfully prepared on the TiO_2 surface by using Cl_2 as an oxidant. Subsequent introduction of NH_3 to the cell resulted in a decrease in the adsorption at 600–800 nm (spectra (c)), which clearly showed the reaction of $Ru^{3+}(bpy)_3$ with NH_3 and reduction to the initial $Ru^{2+}(bpy)_3$ species. The UV–Vis spectroscopic result shows that $Ru^{3+}(bpy)_3$ has the potential to oxidize NH_3. We concluded that $Ru^{3+}(bpy)_3$, generated after the electron injection, activates NH_3 to an NH_2 radical (eq. 3),[48] which reacts with NO_2^- to form N_2 selectively.[12, 48]

$$Ru^{3+}(bpy)_3 + NH_3 \rightarrow Ru^{2+}(bpy)_3 + NH_2 \text{ radical} + H^+ \qquad (3)$$

On the other hand, the electron injected to the conduction band of TiO_2 is consumed by the reaction with O_2 and H^+ (surface OH group) to form H_2O according to eqs. 4 and 5.[12, 15-16]

$$Ti^{4+} + e^-_{cb} \rightarrow Ti^{3+} \qquad (4)$$

$$Ti^{3+} + 1/4O_2 + H^+ \rightarrow Ti^{4+} + 1/2H_2O \qquad (5)$$

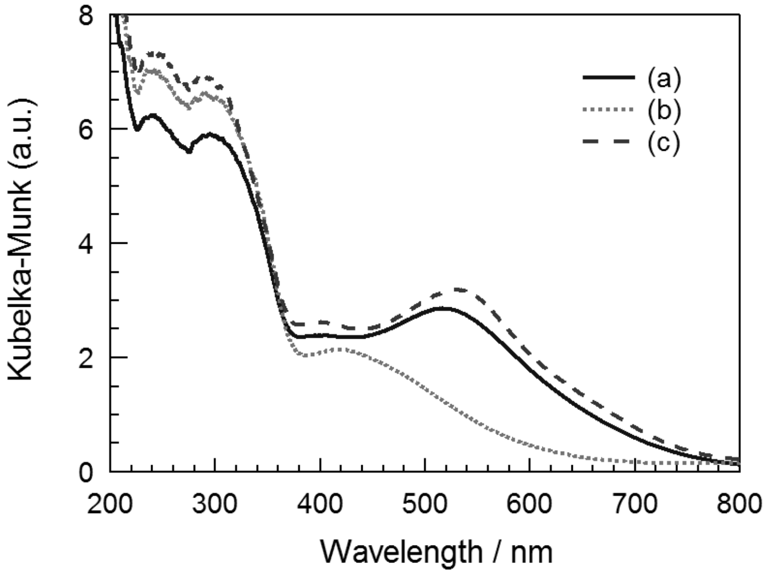

Figrue 11. UV-Vis DR spectra and photographs of 37.5 μmol g^{-1} N3-TiO_2 photocatalyst after evacuation (a), after addition of Cl_2 (b), and after addition of NH_3 (c).

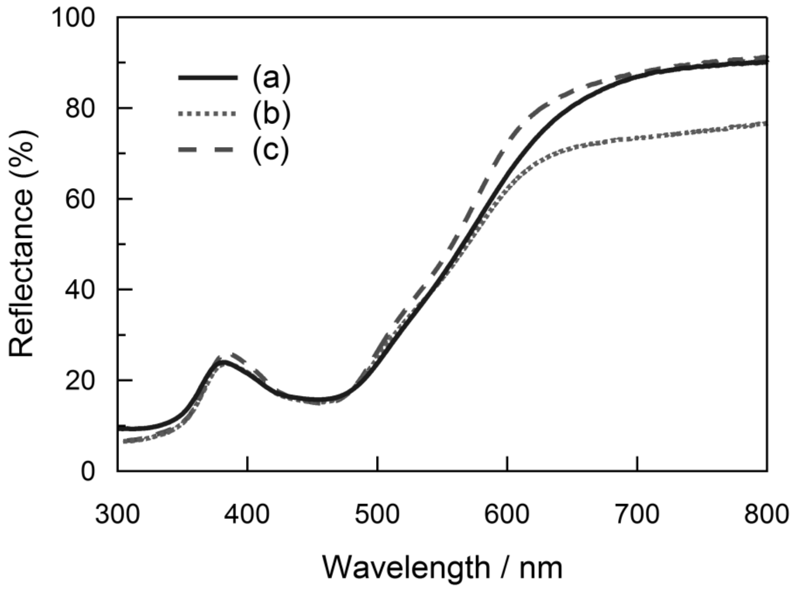

Figure 12. UV–Vis DR spectra of the TiO_2 photocatalyst modified with $Ru(bpy)_3Cl_2$ after evacuation (a), after addition of Cl_2, and after addition of NH_3. Dye loading: 37.5 μmol g^{-1}.

Proposed reaction mechanism and effects of dyes on the activity.

Based on the results obtained thus far, we proposed the reaction mechanism of photo-SCR over Ru-dye-modified TiO_2 photocatalysts under visible-light irradiation (Scheme 2). The mechanism is composed of five steps: (1) adsorption of NO and NH_3 on the catalyst surface, (2) electron injection from photo-excited Ru dyes into the conduction band of TiO_2, (3) activation of NH_3 by oxidized Ru dyes, (4) surface reaction between an NH_2 radical and NO_2^-, and (5) re-oxidation of Ti^{3+} sites by O_2.

In DSSCs, Ru complexes have shown the best photovoltaic properties among a huge number of dyes,[22] and N3-dye was known to be an effective Ru dye for DSSCs due to 1) the wide adsorption range to 800 nm, 2) strong adsorption on the semiconductor surface due to binding with up to four carboxyl groups, and 3) sufficiently long excited state life-time (~20 ns).[22] In our research, N3-dye showed the highest activity in photo-SCR under visible-light irradiation among the 15 dyes studied. The adsorption of N3-dye was not larger than other dyes as shown in Fig. 13. This result indicated that the highest activity was not due to the adsorption amount in the visible region, although this should be a significant factor. In the case of DSSCs, carboxylic groups were necessary in terms of the strong adsorption of dyes on the semiconductor surface, and the strong adsorption led to strong photovoltaic properties. In this research, $Ru(bpy)_3Cl_2$ dye, which does not possess a carboxylic group, also showed high activity (conversion of NO = 70.5%). A similar result for photo-SCR was obtained in our previous reports using the porphyrin-modified TiO_2 photocatalysts with different functional groups.[20] Therefore, carboxylic groups were not important to improve the activity, unlike the DSSCs system. Thus, the life-time of the photo-excited state and the reactivity of the oxidized product of dyes with NH_3, which should affect reaction steps 2 and 3 in Scheme 2, would have a significant effect on the photo-SCR activity.

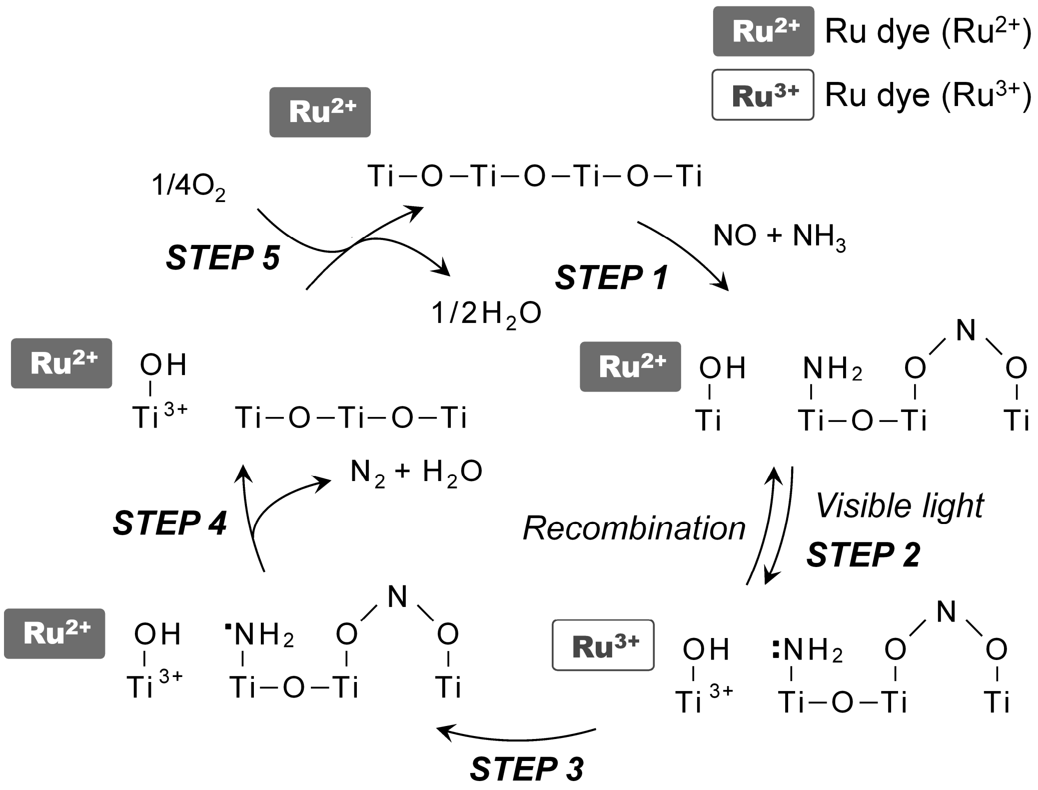

Scheme 2. Proposed reaction mechanism of photo-SCR under visible-light irradiation over Ru complexes modified TiO_2 photocatalyst.

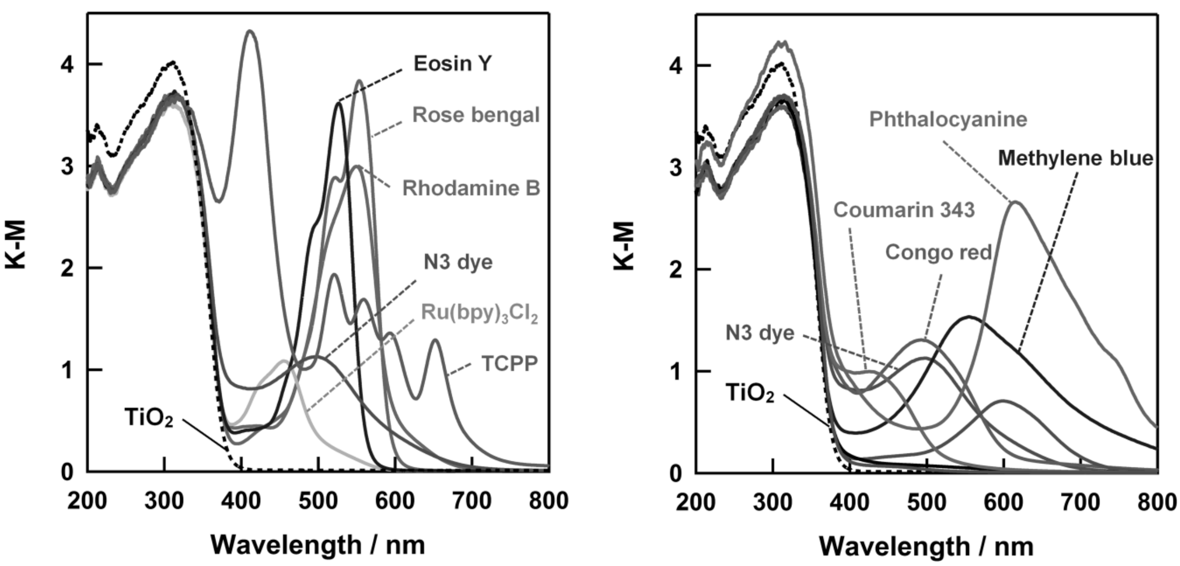

Figure 13. UV–Vis DR spectra of the dye-modified TiO_2 photocatalysts. Dye loading: 12.5 μmol g^{-1}.

Conclusions

We demonstrated high-performance photocatalysts for NH_3-SCR under visible-light irradiation by combining popular dyes with TiO_2 photocatalysts. The screening of 15 dyes displayed that N3-dye was most effective for the modification of TiO_2. Complete conversion of NO and selectivity to N_2 were achieved over N3-TiO_2 at a high GHSV of 100,000 h^{-1} after 30 min of visible-light irradiation. We proposed a reasonable reaction mechanism of the photo-SCR over dye-modified TiO_2 photocatalysts under visible light irradiation by using *in situ* DRIFT and UV–Vis DR spectroscopies. The reaction proceeds via electron injection from dyes excited by visible-light irradiation into the conduction band of TiO_2 (dye-sensitization). The dye oxidation product, generated after the electron injection, oxidatively activates NH_3, which then reacts with surface NO_2^- to provide selective formation of N_2.

References

[1] J. Li, H. Chang, L. Ma, J. Hao, R. T. Yang, *Catal. Today* **2011**, *175*, 147-156.

[2] H. Bosch, F. Janssen, *Catal. Today* **1988**, *2*, 369-379.

[3] G. Busca, L. Lietti, G. Ramis, F. Berti, *Appl. Catal. B* **1998**, *18*, 1-36.

[4] P. Forzatti, L. Lietti, *Heterog. Chem. Rev.* **1996**, *3*, 33-51.

[5] J. A. Sullivan, J. Cunningham, M. A. Morris, K. Keneavey, *Appl. Catal. B* **1995**, *7*, 137-151.

[6] R. Q. Long, R. T. Yang, *J. Am. Chem. Soc.* **1999**, *121*, 5595-5596.

[7] A.-Z. Ma, W. Grunert, *Chem. Commun.* **1999**, 71-72.

[8] R. Q. Long, R. T. Yang, *J. Catal.* **2002**, *207*, 224-231.

[9] C.-L. Myung, A. Ko, J. Kim, K. Choi, S. Kwon, S. Park, *J. Mech. Sci. Technol.* **2013**, *27*, 3893-3902.

[10] L. Dana, K. Fanta, *Urban off-cycle NO_x emissions from Euro IV/V trucks and buses* **2012**, http://www.theicct.org/urban-cycle-nox-emissions-euro-ivv-trucks-and-buses.

[11] T. Tanaka, K. Teramura, K. Arakaki, T. Funabiki, *Chem. Commun.* **2002**, 2742-2743.

[12] K. Teramura, T. Tanaka, S. Yamazoe, K. Arakaki, T. Funabiki, *Appl. Catal. B* **2004**, *53*, 29-36.

[13] S. Yamazoe, T. Okumura, K. Teramura, T. Tanaka, *Catal. Today* **2006**, *111*, 266-270.

[14] A. Yamamoto, Y. Mizuno, K. Teramura, T. Shishido, T. Tanaka, *Catal. Sci. Technol.* **2013**, *3*, 1771-1775.

[15] K. Teramura, T. Tanaka, T. Funabiki, *Langmuir* **2003**, *19*, 1209-1214.

[16] K. Teramura, T. Tanaka, T. Funabiki, *Chem. Lett.* **2003**, *32*, 1184-1185.

[17] Y.-C. Chou, Y. Ku, *Chem. Eng. J.* **2010**, *162*, 696-701.

[18] Y. Chou, Y. Ku, *Front. Environ. Sci. Eng.* **2012**, *6*, 149-155.

[19] Y. Ji, Y. Luo, *J. Phys. Chem. C* **2014**, *118*, 6359-6364.

[20] A. Yamamoto, Y. Mizuno, K. Teramura, S. Hosokawa, T. Shishido, T. Tanaka, *Catal. Sci. Technol.* **2015**, *5*, 556-561.

[21] A. Kay, M. Graetzel, *J. Phys. Chem.* **1993**, *97*, 6272-6277.

[22] A. Hagfeldt, G. Boschloo, L. Sun, L. Kloo, H. Pettersson, *Chem. Rev.* **2010**, *110*, 6595-6663.

[23] N. Robertson, *Angew. Chem. Int. Ed.* **2006**, *45*, 2338-2345.

[24] R. Abe, K. Shinmei, N. Koumura, K. Hara, B. Ohtani, *J. Am. Chem. Soc.* **2013**, *135*, 16872-16884.

[25] R. Abe, K. Shinmei, K. Hara, B. Ohtani, *Chem. Commun.* **2009**, 3577-3579.

[26] R. Abe, K. Sayama, H. Arakawa, *J. Photochem. Photobiol. A* **2004**, *166*, 115-122.

[27] K. Takanabe, K. Kamata, X. Wang, M. Antonietti, J. Kubota, K. Domen, *PCCP* **2010**, *12*, 13020-13025.

[28] T. Hannappel, B. Burfeindt, W. Storck, F. Willig, *J. Phys. Chem. B* **1997**, *101*, 6799-6802.

[29] M. R. Waterland, D. F. Kelley, *J. Phys. Chem. A* **2001**, *105*, 4019-4028.

[30] R. Katoh, A. Furube, T. Yoshihara, K. Hara, G. Fujihashi, S. Takano, S. Murata, H. Arakawa, M. Tachiya, *J. Phys. Chem. B* **2004**, *108*, 4818-4822.

[31] B. O'Regan, M. Gratzel, *Nature* **1991**, *353*, 737-740.

[32] Y. Lu, D.-j. Choi, J. Nelson, O. B. Yang, B. A. Parkinson, *J. Electrochem. Soc.* **2006**, *153*, E131.

[33] H. Rensmo, S. Lunell, H. Siegbahn, *J. Photochem. Photobiol. A* **1998**, *114*, 117-124.

[34] M. K. Nazeeruddin, A. Kay, I. Rodicio, R. Humphry-Baker, E. Mueller, P. Liska, N. Vlachopoulos, M. Graetzel, *J. Am. Chem. Soc.* **1993**, *115*, 6382-6390.

[35] W. M. Campbell, A. K. Burrell, D. L. Officer, K. W. Jolley, *Coord. Chem. Rev.* **2004**, *248*, 1363-1379.

[36] H. Imahori, T. Umeyama, S. Ito, *Acc. Chem. Res.* **2009**, *42*, 1809-1818.

[37] T. Ma, K. Inoue, H. Noma, K. Yao, E. Abe, *J. Photochem. Photobiol. A* **2002**, *152*, 207-212.

[38] F. Odobel, E. Blart, M. Lagree, M. Villieras, H. Boujtita, N. El Murr, S. Caramori, C. Alberto Bignozzi, *J. Mater. Chem.* **2003**, *13*, 502-510.

[39] A. Yella, H.-W. Lee, H. N. Tsao, C. Yi, A. K. Chandiran, M. K. Nazeeruddin, E. W.-G. Diau, C.-Y. Yeh, S. M. Zakeeruddin, M. Grätzel, *Science* **2011**, *334*, 629-634.

[40] H. Hagiwara, N. Ono, T. Inoue, H. Matsumoto, T. Ishihara, *Angew. Chem. Int. Ed.* **2006**, *45*, 1420-1422.

[41] H. Hagiwara, T. Inoue, S. Ida, T. Ishihara, *PCCP* **2011**, *13*, 18031-18037.

[42] M. K. Nazeeruddin, R. Humphry-Baker, M. Gratzel, M. K. Nazeeruddin, R. Humphry-Baker, M. Gratzel, B. A. Murrer, *Chem. Commun.* **1998**, 719-720.

[43] S. Eu, T. Katoh, T. Umeyama, Y. Matano, H. Imahori, *Dalton Trans.* **2008**, 5476-5483.

[44] V. Aranyos, J. Hjelm, A. Hagfeldt, H. Grennberg, *J. Porphyrins Phthalocyanines* **2001**, *05*, 609-616.

[45] A. Morandeira, I. López-Duarte, M. V. Martínez-Díaz, B. O'Regan, C. Shuttle, N. A. Haji-Zainulabidin, T. Torres, E. Palomares, J. R. Durrant, *J. Am. Chem. Soc.* **2007**, *129*, 9250-9251.

[46] K. Hara, Z.-S. Wang, T. Sato, A. Furube, R. Katoh, H. Sugihara, Y. Dan-oh, C. Kasada, A. Shinpo, S. Suga, *J. Phys. Chem. B* **2005**, *109*, 15476-15482.

[47] T. Horiuchi, H. Miura, S. Uchida, *Chem. Commun.* **2003**, 3036-3037.

[48] S. Yamazoe, K. Teramura, Y. Hitomi, T. Shishido, T. Tanaka, *J. Phys. Chem. C* **2007**, *111*, 14189-14197.

[49] Y. J. Kim, H. J. Kwon, I. Heo, I.-S. Nam, B. K. Cho, J. W. Choung, M.-S. Cha, G. K. Yeo, *Appl. Catal. B* **2012**, *126*, 9-21.

[50] Y. Ooyama, Y. Harima, *Eur. J. Org. Chem.* **2009**, *2009*, 2903-2934.

[51] D. V. Pozdnyakov, V. N. Filimonov, *Kinet. Katal.* **1973**, *14*, 760.

[52] K. I. Hadjiivanov, *Cat. Rev. - Sci. Eng.* **2000**, *42*, 71-144.

[53] H. Knözinger, P. Ratnasamy, *Catal. Rev.* **1978**, *17*, 31-70.

[54] G. Munuera, V. Rives-Arnau, A. Saucedo, *J. Chem. Soc., Faraday Trans. 1* **1979**, *75*, 736-747.

[55] W. H. Quayle, J. H. Lunsford, *Inorg. Chem.* **1982**, *21*, 97-103.

[56] S. Das, P. V. Kamat, *J. Phys. Chem. B* **1998**, *102*, 8954-8957.

Chapter 4

Effects of SO_2 on Selective Catalytic Reduction of NO with NH_3 over a TiO_2 Photocatalyst

Abstract

The effect of SO_2 gas was investigated on the activity of the photo-assisted selective catalytic reduction of nitrogen monoxide (NO) with ammonia (NH_3) over a TiO_2 photocatalyst in the presence of excess oxygen (photo-SCR). Introduction of SO_2 (300ppm) greatly decreased the activity of the photo-SCR at 373 K. Increment of the reaction temperature enhanced the resistance to SO_2 gas and, at 553 K, the conversion of NO was stable for at least 300 min of the reaction. X-ray diffraction, Fourier transform infrared spectroscopy, thermogravimetry and differential thermal analysis, X-ray photoelectron spectroscopy, elemental analysis, and N_2 adsorption measurement revealed that the ammonium sulfate species were generated after the reaction. There was a strong negative correlation between the deposition amount of the ammonium sulfate species and the specific surface area. Based on the above relationship, we concluded that the deposition of the ammonium sulfate species decreased the specific surface area by plugging the pore structure of the catalyst and the decrease of the specific surface area resulted in the deactivation of the catalyst.

Introduction

The emission of nitrogen oxides (NO_x) causes air pollution problems such as acid rain and photochemical smog. Selective catalytic reduction (SCR) of NO_x with ammonia (NH_3) is a commercial de-NO_x process in the stationary and mobile NO_x emission sources. The main reaction is as follows:

$$4NO + 4NH_3 + O_2 \rightarrow 4N_2 + 6H_2O \qquad (1)$$

In the stationary emission sources, the industrial catalyst for the process is vanadium oxide based catalysts, such as V_2O_5–WO_3/TiO_2 [1-2]. The catalysts show the high activity and high selectivity to N_2 in the temperature window of 523–673 K. This type of catalyst has to be installed upstream the particulate collector and the flue-gas desulfurization unit in order to meet the optimum working temperature. However, the catalysts are not available in the diesel engine because of the wide temperature window (423–773 K) of the exhaust gas. A promising catalyst which shows high activity at low temperatures is strongly desired for the diesel engine.

Mn based catalysts were eagerly investigated due to the high activity at low temperatures [3-8]. The Mn based catalysts show almost 100% of the conversion in the temperature range of 373–473 K although the selectivity to N_2 is slightly low in some reaction conditions [3-4]. The problem of the Mn based catalysts is low resistance to SO_2 poisoning. Kijlstra et al. [9] proposed that the formation of $MnSO_4$ is the main reason for the deactivation of the MnO_x/Al_2O_3 catalysts. The formed sulfates decomposed at 1020 K, which means regeneration of the catalysts is only possible at much higher temperatures than the reaction temperature. On this point, the simultaneous pursuit of the operation at low temperatures and the high resistance to SO_2 gas is a challenging and important topic in the de-NO_x technology.

We have previously reported the photo-assisted SCR of NO with NH_3 over TiO_2 photocatalysts in the presence of excess oxygen (O_2) at ambient temperature. In the photocatalytic system, high conversion and high selectivity were achieved at the gas hourly space velocity (GHSV) of 25,000 h^{-1} (conversion of NO > 90%, selectivity to N_2 > 95%) [10]. We have carried out various investigations: the elucidation of the reaction mechanism using spectroscopic methods [11] and kinetic analysis [12], the improvement of the activity by metal doping [13] and combining the temperature effect with the photo-SCR [14], and the development of visible-light-sensitive photocatalyst with dye-sensitization [15]. Other research groups also carried out a theoretical study [16], which verified the proposed reaction mechanism by our group [11, 17], and a kinetic study using an annular fixed-film photoreactor [18]. However, the potential of the photocatalyst for the resistance to SO_2 gas has not been investigated yet although the resistance is essential to make the photo-SCR system practicable. Thus, our objective is to investigate the effect of SO_2 gas on the performance of the photo-SCR over the TiO_2 photocatalyst. In addition, the systematic characterization of the catalyst after the reaction was carried out to elucidate the deactivation mechanism of the TiO_2 photocatalyst.

Experimental

Materials

TiO_2 (ST-01) powder was purchased from Ishihara Sangyo Kaisha, Ltd. Before use, the TiO_2 power was hydrated in distilled water for 2 h at 353 K, and then evaporated to dryness at 353 K. The powder after the hydration was tableted (diameter 20 mm) and calcined at 673 K for 3 h in a furnace under a dry air flow. The tablet was granulated using 25 and 50 mesh sieves to obtain the granules with a diameter of 300–600 μm. Ammonium sulfate (wako), and sodium sulfate (wako) were used as reference samples without further purification.

Photocatalytic reaction

Photo-SCR was carried out using a conventional fixed bed flow reactor at an atmospheric pressure in the same way as in our previous reports [14]. A quarts reactor was used for the reaction and the reactor volume was 0.12 mL (12×10×1 mm). 110 mg of TiO_2 granules with a diameter of 300–600 μm were introduced to the reactor and pretreated at 673 K in a 10% O_2/He gas at a flow rate of 50 mL min^{-1} for 60 min. The reaction gas composition was as follows: NO (1000ppm), NH_3 (1000ppm), O_2 (2%), SO_2 (300ppm, if present), He balance. A 200 W Hg–Xe lamp equipped with fiber optics, collective lens, and a mirror (San-Ei Electric Co., Ltd., UVF-204S type B) was used as a light source. The measured light irradiance was 360 mW cm^{-2}. N_2 and N_2O products were analyzed by a SHIMADSU GC-8A TCD gas chromatograph with MS-5A and Porapak Q columns, respectively.

Characterization

Crystalline phase of the TiO_2 powder was determined by X-ray diffraction (XRD) technique using a Rigaku Ultima IV X-ray diffractometer with Cu-Kα radiation (λ = 1.5406 Å). The crystallite size was determined from the full width at half maximum (FWHM) of the diffraction peak of the anatase TiO_2 (101) plane (2θ=25.2°) using the Scherrer's equation. Fourier transform infrared (FTIR) transmission spectra were recorded on a JASCO FT/IR-4200 spectrometer at room temperature at a spectral resolution of 4 cm^{-1} accumulating 16 scans. The background spectrum was measured without any sample in air and was subtracted from the sample spectra. The catalysts before and after the reaction and the reference samples (ammonium sulfate and sodium sulfate) were diluted with KBr by the sample-to-KBr ratio of 1.5:98.5 and 0.2:99.8 (w/w), respectively, and then pressed into pellets. Thermo-gravimetric analysis (TG) and differential thermal analysis (DTA) were performed on a Rigaku Thermo plus TG 8120 apparatus at a heating rate of 5 K min^{-1} under a dry air flow condition at a flow rate of 80 mL min^{-1} in the range of 298–1173 K using Al_2O_3 pans. X-ray photoelectron spectroscopy (XPS) measurement was conducted on a Shimadzu ESCA-3400 spectrometer. Samples were mounted on a silver sample holder by using a conductive carbon tape and analyzed using Mg Kα radiation in a vacuum chamber in 0.1 eV steps. The position of the carbon peak (284.6 eV) for C1s was used to calibrate the binding energy for all the samples. The surface composition was estimated from the band areas of XP spectrum of S2p, N1s, Ti2p, and O1s and the corresponding relative sensitivity factors [19]. Elemental analyses (EA) were performed on two CHN analyzers (MT-5, Yanaco Co. Ltd. and JM10, J-Science Lab Co. Ltd.) to analyze the contents of C, H, and N and a combustion ion chromatography (Dionex ICS-1500, Mitsubishi Chemical Analytech AQF-2100H) to analyze the S content. N_2 adsorption/desorption isotherm was measured at 77 K using liquid nitrogen. The Brunauer–Emmett–Teller (BET) method was utilized to calculate the specific surface areas (S_{BET}). The total specific surface area (S_{tot}) and the external specific surface area (S_{ext}) were calculated from the linear fitting of the *V*–*t* plots (fitting range: 0–0.6 nm for the S_{tot}, and 3.6–4.6 nm for the S_{ext}. The internal specific surface (S_{int}) area for the mesoporous materials was obtained by subtracting the S_{ext} from the S_{tot}. The pore-size distribution was calculated from the Barrett–Joyner–Halenda (BJH) plots.

Results and discussion

Effect of SO_2 addition on the activity of the photo-SCR

Fig. 1 shows the time course of the photo-SCR over the TiO_2 photocatalyst under illumination in the presence or absence of SO_2 (300ppm) gas at various temperatures. The conversion of NO was stable for 300 min at 433 K in the absence of SO_2 gas as we reported previously [14]. In the presence of SO_2 at 433 K, the conversion of NO decreased with the reaction time, which indicates that the SO_2 poisoned the catalyst, as in the case of the Mn based catalysts [9]. The reaction temperature had a significant effect on the deactivation rate of the TiO_2 photocatalyst. At 373 K, the conversion decreased more rapidly than at 433 K and the conversion was almost stable for at least 300 min at 553 K. For simplification, the sample before the reaction was abbreviated as BR, and the samples after the reactions at 373 K, 433 K, and 553 K as AR-373K, AR-433K, and AR-553K, respectively.

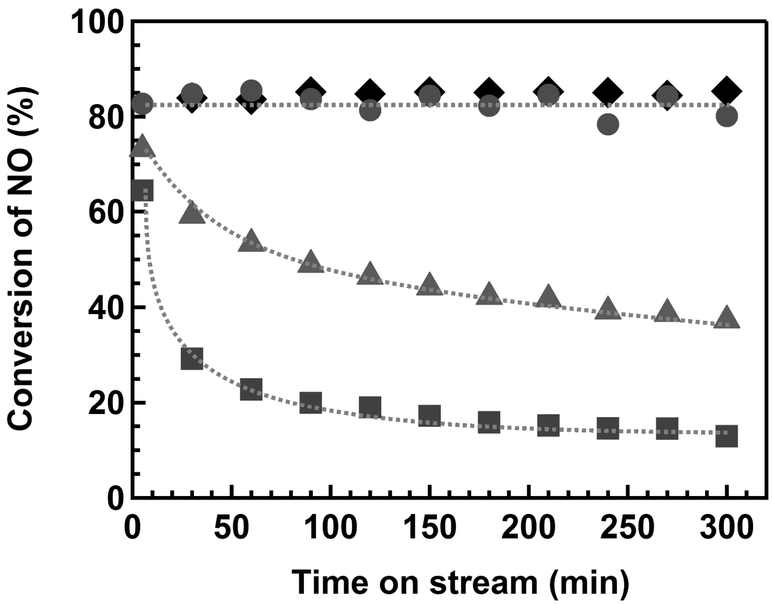

Figure 1. Time course of the photo-SCR in the presence or absence of SO_2 gas at various temperatures. (◆) SO_2: 0ppm, 433 K, (▲) SO_2: 300ppm, 373 K, (■) SO_2: 300ppm, 433 K, (●) SO_2: 300ppm, 553 K. NO: 1000 ppm, NH_3: 1000 ppm, O_2: 2 %, He: balance gas, flow rate: 200 mL min^{-1}, GHSV: 100,000 h^{-1}, Light source: 200 W Hg–Xe lamp.

XRD patterns

XRD patterns of the catalysts are shown in Fig. 2. In all the catalysts, only the diffraction pattern of anatase TiO_2 was observed. Crystalline sizes of anatase TiO_2 were estimated from Scherrer equation using the diffraction peaks of (101) and the results are listed in Table 1. The crystalline size did not change (ca. 15 nm) after the reaction, revealing that the aggregation of TiO_2 particles did not occur under the reaction conditions at the all reaction temperatures.

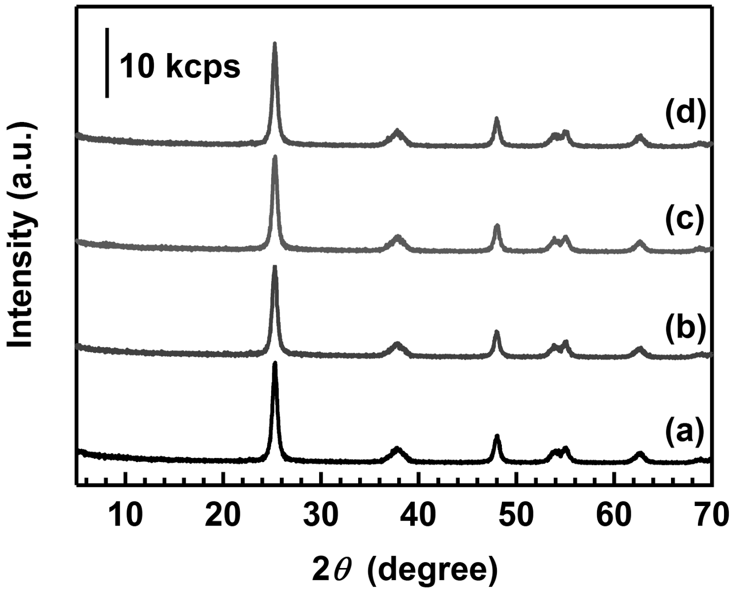

Figure 2. XRD patterns of the catalysts before and after the reaction. (a) BR, (b) AR-373K, (c) AR-433K, and (d) AR-533K. Patterns are offset for clarity.

Table 1. Crystalline size and specific surface area of catalysts.

Sample	d [a] (nm)	S_{BET} [b] (m^2 g^{-1})	S_{tot} [c] (m^2 g^{-1})	S_{ext} [d] (m^2 g^{-1})	S_{int} [e] (m^2 g^{-1})
BR	15.2	121	123	10.6	112
AR-373K	15.0	84.3	87.0	10.8	76.2
AR-433K	15.2	96.6	99.6	9.0	90.6
AR-553K	15.3	115	118	9.0	109

[a] Crystalline size calculated from the FWHM of the diffraction peak of the anatase TiO_2 (101) plane. [b] Specific surface area determined by N_2 adsorption isotherm at 77 K using the BET method. [c] Total specific surface area calculated from the *V*–*t* plots. [d] External specific surface area calculated from the *V*–*t* plots. [e] Internal specific surface area calculated by subtracting the external specific surface area from the total specific surface area.

N_2 adsorption/desorption experiments

In N_2 adsorption/desorption experiments at 77 K (Fig. 3), all the samples exhibited a typical IV-type isotherm and had a vertically long hysteresis loop in the relative pressure (P/P_0) range of 0.8–1.0, suggesting that all the samples had a porous structure. The pore-size distribution of the catalyst before the reaction had a sharp peak at 10 nm (Fig. 4A) and the size was the same order of the crystalline size of TiO_2 (15 nm). These results indicate that the mesopores were formed by the gaps between primary TiO_2 particles. The peak became smaller after the reaction in the presence of SO_2 gas. The specific surface area calculated from the *V*–*t* plots (Fig. 4B) is summarized in Table 1. The S_{tot} calculated from the *V*–*t* plots was in good agreement in the S_{BET}. The S_{ext} of all the samples were estimated from the *V*–*t* plots as 9.0–10.8 m^2 g^{-1}. The S_{int} was calculated by subtracting the S_{ext} from the S_{tot}. The S_{int} was 76.2–112 m^2 g^{-1}, which shows that the most part of the S_{tot} was derived from the mesopores.

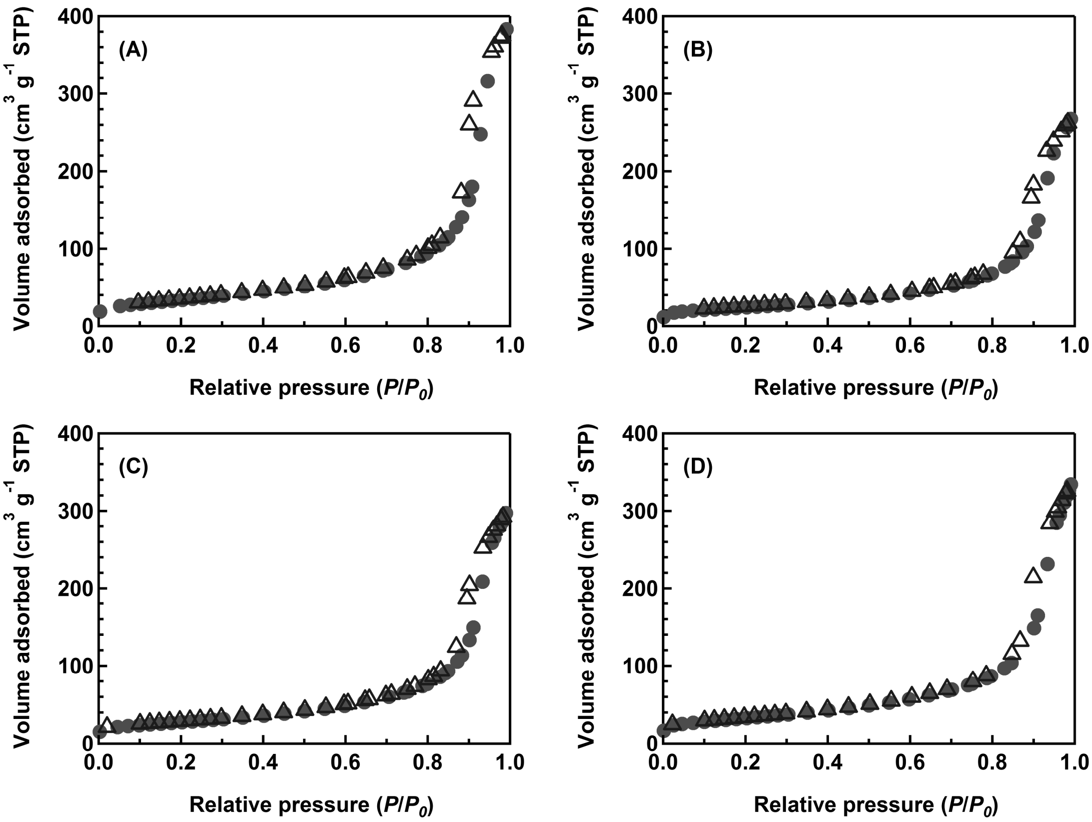

Figure 3. N_2 adsorption/desorption isotherms at 77 K of (A) BR, (B) AR-373K, (C) AR-433K, and (D) AR-533K. ●: adsorption, △: desorption, pretreatment: evacuation at 398 K for 2 h.

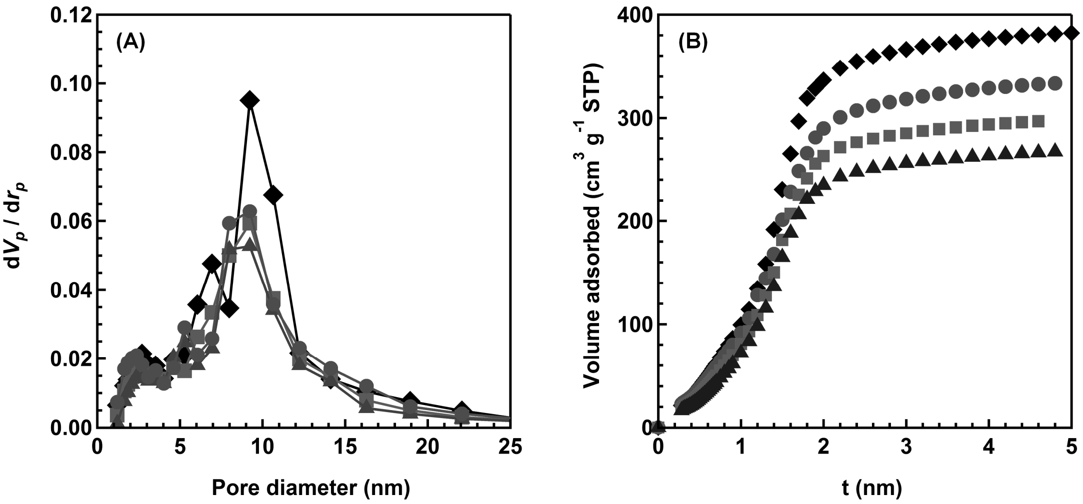

Figure 4. (A) BJH (Barrett-Joyner-Halenda) pore size distribution plots, and (B) *V–t* plots of the catalysts. ◆: BR, ▲: AR-373 K, ■: AR-433 K, ●: AR-553 K.

FTIR spectra

Fig. 5A shows the FTIR spectra of the catalysts in the region of 900–1800 cm^{-1}. In all the catalysts, a band at 1633 cm^{-1} was observed and was attributed to the deformation vibration of water molecules adsorbed on the TiO_2 surface. New bands at 1401, 1242, 1116, 1054, and 978 cm^{-1} appeared after the reaction in the presence of SO_2 at 373 K. The sharp band at 1401 cm^{-1} was assigned to the bending vibration of ammonium (NH_4^+) ions [20] and was also observed in the case of the reference $(NH_4)_2SO_4$ powder. Free sulfate ions (SO_4^{2-}, T_d symmetry) show two infrared peaks at 1104 (ν_3) and 613 (ν_4) cm^{-1} [20]. The band at 1116 cm^{-1} was due to ν_3 vibration of free sulfate ions, and was also observed in both the cases of $(NH_4)_2SO_4$ and Na_2SO_4. When a SO_4^{2-} ion is bound to the TiO_2 surface, the symmetry can be lowered to either C_{3v} or C_{2v}. The lowering symmetry causes the split of the ν_3 vibration band into two peaks for a C_{3v} symmetry and splits into three peaks for a C_{2v} symmetry [20]. Thus, the bands at 1242, 1054, and 978 $cm^{-1}$are assigned to the surface coordinated SO_4^{2-} ions. The surface coordinated SO_4^{2-} ions could have the C_{2v} symmetry based on the number of bands. The SO_4^{2-} ion with a C_{2v} configuration is either chelating bidentate or bridge bidentate [20]. In AR-433K, the shape of the spectrum was similar to that of AR-373K although the absorbance of the bands at 1401 and 1116 cm^{-1} were slightly weaker than those of AR-373K. In AR-553K, the band at 1116 cm^{-1} disappeared, which means that the deposition of free sulfates was inhibited in the reaction at 553 K although the other bands at 1401, 1054, and 978 cm^{-1} remained. In the region of 2400–4000 cm^{-1} (Fig. 5B), three adsorption bands at 3425, 3136, 3023 cm^{-1} were observed after the reaction at 373 K. The broad band between 3600–2800 cm^{-1} is the stretching vibration of OH groups derived from surface hydroxyl groups and adsorbed water molecules, which also appeared in the sample before the reaction. The other two bands were observed in the catalysts after the reaction. The bands at 3136 and 3023 cm^{-1} are attributed to the asymmetric stretching vibration (ν_3) and symmetric stretching vibration (ν_1) of NH_4^+ ions, respectively. The two bands also appeared in the case of $(NH_4)_2SO_4$, which strongly advocated the generation of NH_4^+ ions after the reaction. The peak intensity at 3136 and 3023 cm^{-1} decreased as the reaction temperature increased, which was consistent with the decrease of the band at 1401 cm^{-1} in Fig. 5A. The FTIR results clearly revealed generation of the free and surface coordinated SO_4^{2-} ions and NH_4^+ ions on the TiO_2 surface after the reaction. The conversion of NO after 300 min of the reaction decreased in the following order:

AR-553K (80.1%) > AR-433K (37.2%) > AR-373K (12.9%). The order was consistent with that of the peak intensities of the free SO_4^{2-} ions and NH_4^+ ions, which suggests that generation of ammonium sulfate species (*e.g.* $(NH_4)_2SO_4$ and $(NH_4)HSO_4$) induced the deactivation of the catalyst.

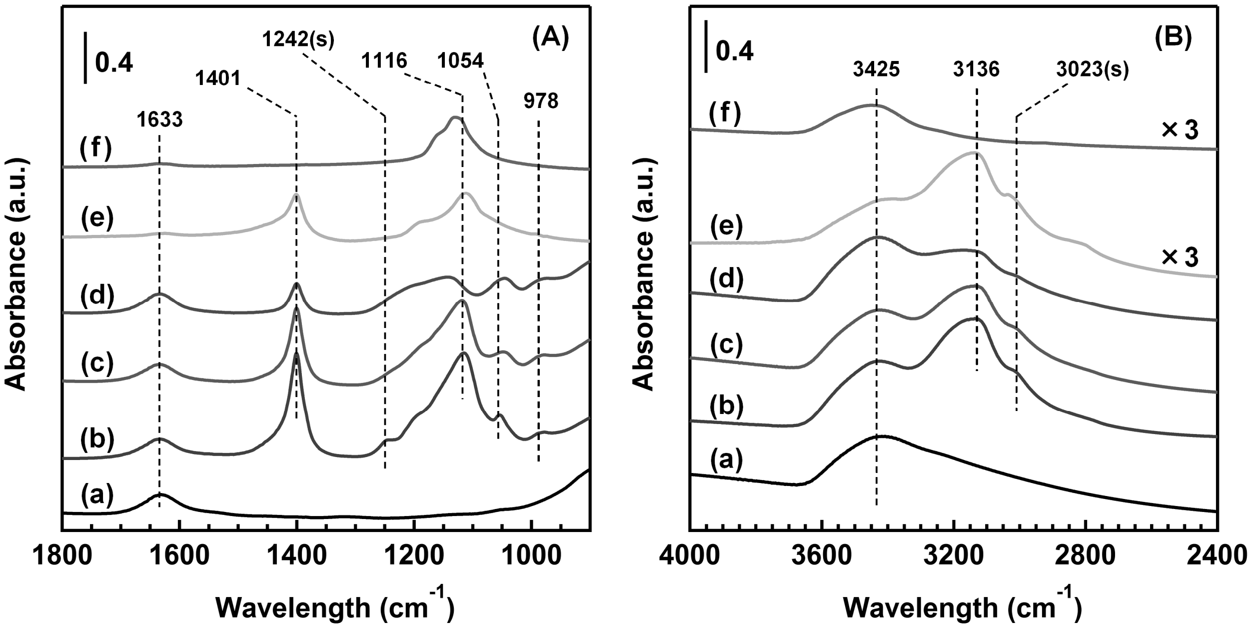

Figure 5. FTIR spectra of the catalysts and the reference samples in the region of (A) 900–1800 cm^{-1} and (B) 2400–4000 cm^{-1}. (a) BR, (b) AR-373K, (c) AR-433K, (d) AR-533K, (e) $(NH_4)_2SO_4$, and (f) Na_2SO_4. Spectra are offset for clarity.

TG-DTA analysis

TG profiles of the catalysts are shown in Fig. 6A. Several steps of the weight loss were observed in all the catalysts after the reaction, although the TiO_2 has only one step of the weight loss around 330 K. From room temperature to 1173 K, the weights of BR, AR-373K, AR-433K, and AR-553K decreased by 3.9, 16.1, 12.5, 8.1%, respectively. Fig. 6B shows the DTA profiles of the catalysts. All the profiles had a strong exothermic band around 1150 K without a weight loss, which was derived from the phase transition of TiO_2 from anatase to rutile. In the DTA profile of BR (see inset of Fig. 6B), a broad exothermic band was observed around 820 K without the weight loss. The peak was observed in all the catalysts before and after the reaction and was possibly due to the crystallization of TiO_2 [21]. Besides, other exothermic bands were observed around 500 and 700 K in the case of the catalysts after the reaction.

Fig. 6C shows the first derivatives of the TG profiles (DTG) in Fig. 6A. The negative band around 330 K was observed in all the catalysts and assigned to desorption of molecular water. Other weight loss peaks were observed around 496 K, 648 K, 740 K, and 940 K. DTG profiles of the $(NH_4)_2SO_4$ powder and a physical mixture sample of the $(NH_4)_2SO_4$ powder and the TiO_2 powder are also shown in Fig. 6C. In the $(NH_4)_2SO_4$ powder, two peaks were observed at 530 K and 620 K, which were attributed to the following reactions (2) and (3), respectively [22].

$$2(NH_4)_2SO_4 \rightarrow (NH_4)_2S_2O_7 + 2NH_3 + H_2O \qquad (2)$$

$$3(NH_4)_2S_2O_7 \rightarrow 6SO_2 + 2NH_3 + 2N_2 + 9H_2O \qquad (3)$$

In the physical mixture sample of the $(NH_4)_2SO_4$ powder and the TiO_2 powder, the weight loss profile had negative peaks around 313 K, 508 K, 648 K, 760 K, and 940 K and the peak positions were in good agreement with those of the profile of AR-373K. The analogy of the profiles strongly supports the generation of $(NH_4)_2SO_4$ species on the TiO_2 surface after the reaction at 373 K. The bands around 500, and 650 K decreased as the reaction temperature increased from 373 K to 553 K, which suggests that the increase of the reaction temperature inhibits the deposition of the $(NH_4)_2SO_4$ species on the TiO_2 surface.

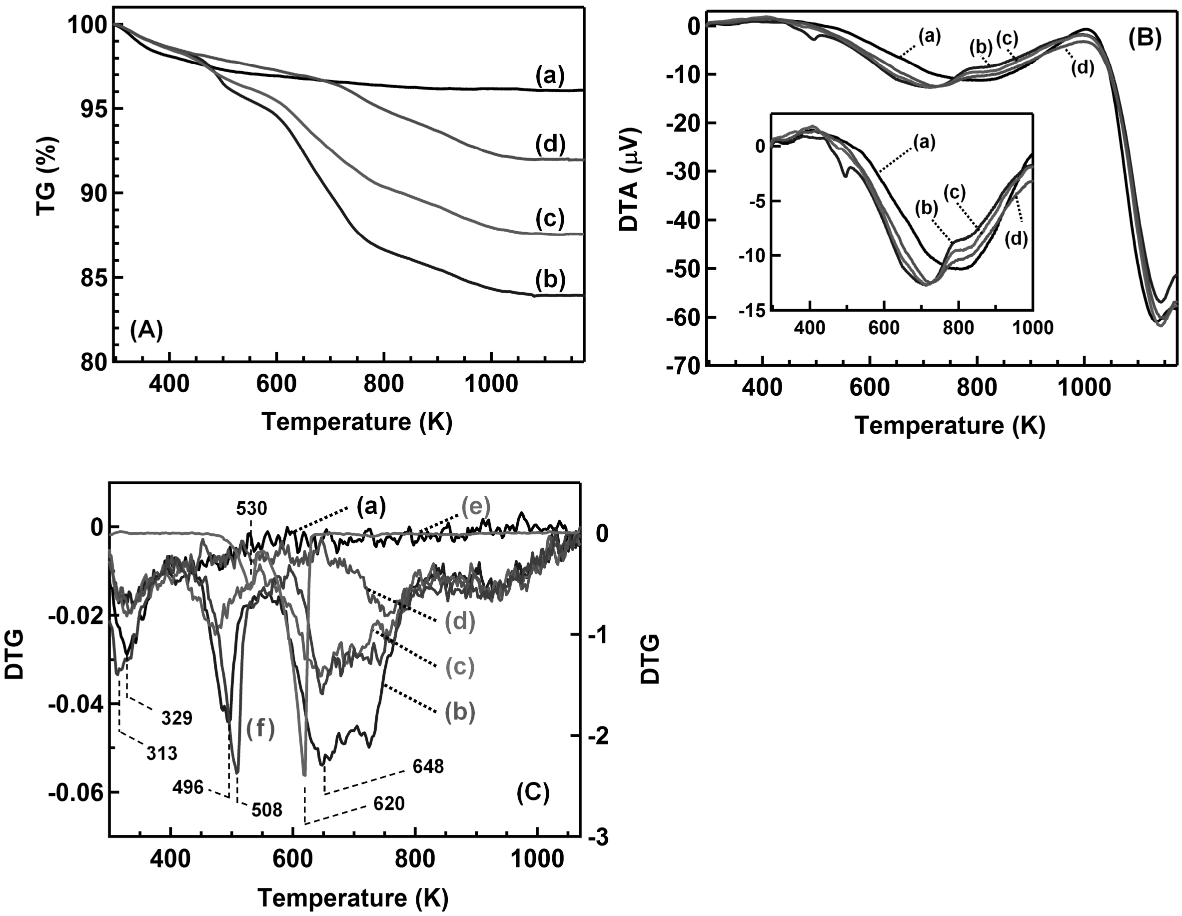

Figure 6. (A) TG profiles, (B) DTA profiles, and (C) derivative thermogravimetry (DTG) profiles of the catalysts and the reference samples. (a) BR, (b) AR-373K, (c) AR-433K, (d) AR-533K, (e) $(NH_4)_2SO_4$, and (f) physical mixture of $(NH_4)_2SO_4$ and TiO_2 ($(NH_4)_2SO_4$: 10 % by weight).

XPS

In the S 2p XP spectra of BR (Fig. 7A), no band was observed in the range of 165–175 eV. In all the catalysts after the reaction, asymmetric bands were observed at the peak position of 168.6–168.8 eV. The asymmetry of the bands is because of the overlap of the split sublevels of $2p_{3/2}$ and $2p_{1/2}$ states of S atoms (separation of bands: 1.2 eV) by spin-orbit coupling [23]. The spectra of the catalysts after the reaction were reasonably fitted using two Gaussian functions (Fig. 8 and Table 2). In all the catalysts after the reaction, the peak positions were 168.5–168.6 and 169.7–169.9 eV, which corresponded to the peak positions of S $2p_{3/2}$ and S $2p_{1/2}$ of sulfate (SO_4^{2-}) species, respectively [20]. The ratios of the peak areas of S $2p_{3/2}$ to those of S $2p_{1/2}$ were 1.96–1.99 in all the catalysts after the reaction and the values were in good agreement with the theoretical value of 2. The FWHM of the each peak was the same in all the catalysts (ca. 1.6 eV), which suggests that the S 2p XP spectra of the catalysts are derived from a single sulfur species of SO_4^{2-} (S^{6+}). N 1s XP spectra are shown in Fig. 7B. The peak positions of N bands of NO_2^- and NO_3^- species on the TiO_2 surface were reported to be 403.5 eV and 407.0 eV, respectively [24-25]. There was no band in the region of 403.5–407.0 eV, indicating that the NO_2^- and NO_3^- species did not exist in all the catalysts after the reaction. In AR-373K, there were two bands with the peak positions at 399.9 and 401.8 eV. The shoulder band at 399.9 eV was attributed to N atoms of NH_3 adsorbed on Lewis acid sites of TiO_2, and the band at 401.8eV was N atoms of NH_4^+ specie adsorbed on Brønsted acid sites and/or ammonium salts [20]. The band at 401.8 eV decreased with increasing the reaction temperature and disappeared in the spectrum of AR-533 K. In Ti 2p XP spectra (Fig. 7C), the binding energies of the band of Ti $2p_{3/2}$ and $2p_{1/2}$ were 458.6–458.8 and 464.4–464.6 eV in all the catalysts before and after the reaction (Table 3). The values were consistent with those reported in the literature [20].

Table 4 shows the surface composition estimated from the XPS analysis. The ratio of S atoms to Ti atoms (S/Ti) decreased in the order of AR-373K > AR-433K > AR-553K. The N atoms to Ti atoms (N/Ti) ratio also decreased with increasing the reaction temperature. The decreases of S/Ti and N/Ti ratio should be mainly due to the decomposition of $(NH_4)_2SO_4$ species based on the FTIR and TG-DTA analyses. The ratio of N atoms to S atoms (N/S) decreased from 0.41 (373K) to 0.10 (553K) with the reaction temperature. The N/S values of the catalysts were lower than that of $(NH_4)_2SO_4$ powder (0.85). The low N/S values of the catalysts suggests the existence of sulfur species other than $(NH_4)_2SO_4$. From the XPS analysis, SO_3^{2-} species were not detected and the valence of all the sulfur species was +6. The FTIR spectroscopy revealed the generation of the surface coordinated SO_4^{2-} species with the C_{2v} and/or C_{3v} symmetries. Thus, the low N/S values were due to the generation of the surface coordinated SO_4^{2-} species. Based on the above discussion, the decease of the N/S values with the increase of the reaction temperature is interpreted by the preferential decrease of the $(NH_4)_2SO_4$ species compared to the surface coordinated SO_4^{2-} species with increasing the reaction temperature.

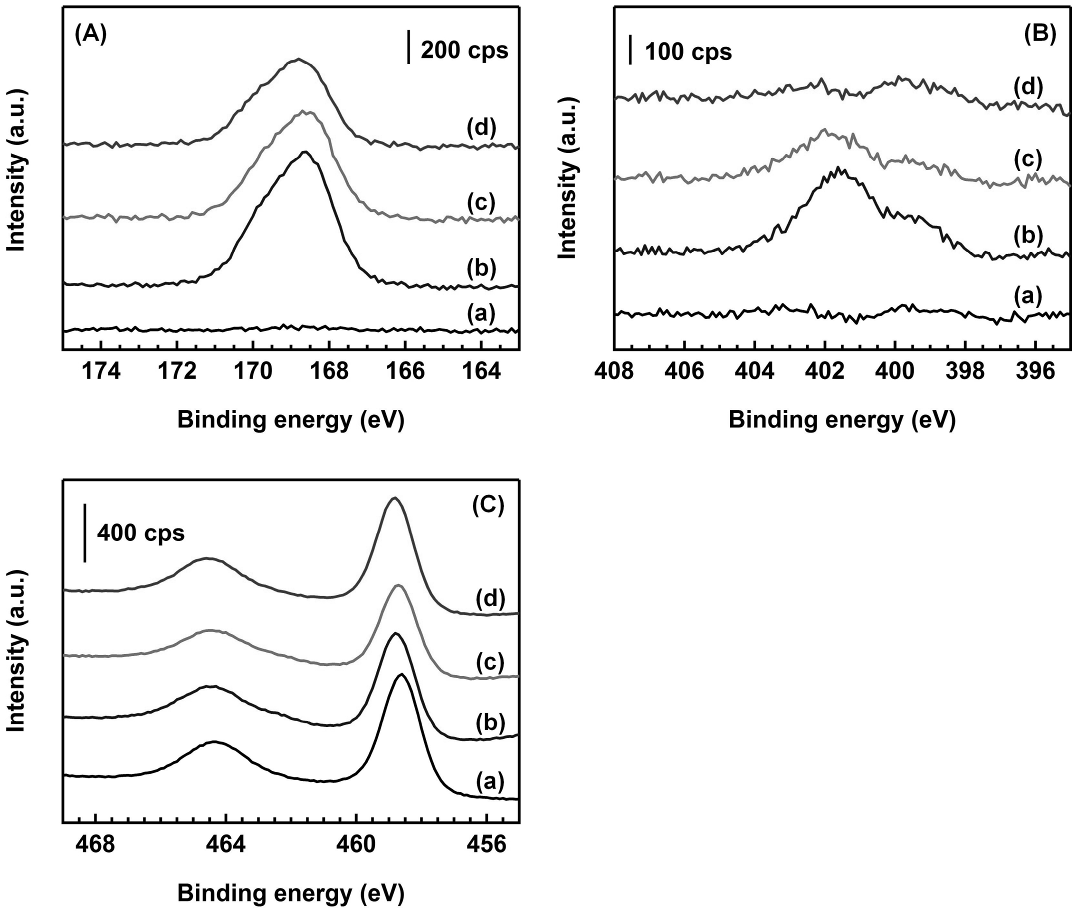

Figure 7. XP spectra of (A) S 2p, (B) N 1s, and (C) Ti 2p of the catalysts. (a) BR, (b) AR-373K, (c) AR-433K, and (d) AR-533K. Patterns are offset for clarity.

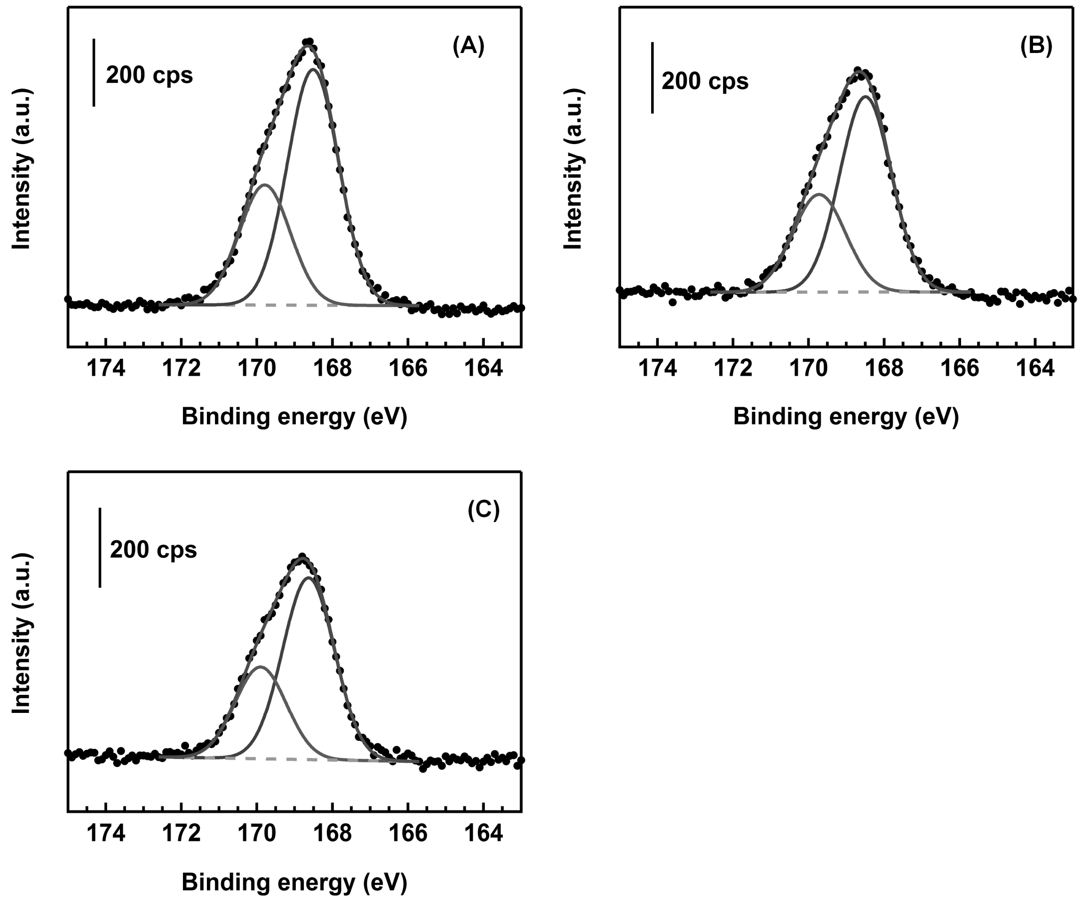

Figure 8. Result of the peak fitting of S 2p XP spectra of AR-373K (A), AR-433K (B), and AR-533K (C). Back circles: experimental data, dashed line: base line (linear function), solid lines: the result of the peak fitting.

Table 2. Results of the peak fitting of S 2p XP spectra.

Sample	Position (eV)		Area (cps [a]・eV)			FWHM (eV)	
	$2p_{3/2}$	$2p_{1/2}$	$2p_{3/2}$	$2p_{1/2}$	Ratio [b]	$2p_{3/2}$	$2p_{1/2}$
AR-373 K	168.5	169.8	1180	599	1.97	1.6	1.59
AR-433 K	168.5	169.7	937	478	1.96	1.61	1.64
AR-553 K	168.6	169.9	780	391	1.99	1.61	1.60

[a] Counts per second

[b] Ratio of the peak area of S $2p_{3/2}$ to that of S $2p_{1/2}$.

Table 3. Peak positions of XP spectra of Ti $2p_{3/2}$ and Ti $2p_{1/2}$.

Sample	Peak position (eV)	
	Ti $2p_{3/2}$	Ti $2p_{1/2}$
BR	458.6	464.4
AR-373 K	458.8	464.5
AR-433 K	458.7	464.5
AR-553 K	458.8	464.6

Table 4. Surface composition estimated from XPS.

Sample	S/Ti	N/Ti	N/S
BR	0	0	–
AR-373K	0.28	0.11	0.41
AR-433K	0.27	0.07	0.26
AR-553K	0.14	0.01	0.10
$(NH_4)_2SO_4$	–	–	0.85

Elemental analysis (EA)

Concentrations of sulfur atoms and nitrogen atoms were estimated from EA (Table 5). The concentration of S atoms and N atoms increased after the reaction and decreased with increasing the reaction temperature. The tendency corresponded to the results of XPS analysis. Surface densities of each atom were calculated by dividing the concentrations by the BET specific surface area of BR (Table 1). The surface density of Ti atoms was calculated to be 7.0 nm^{-2} using a (100) plane of anatase TiO_2 [26] and the BET specific surface area of BR. In AR-373K, the surface densities of sulfur atoms and nitrogen atoms were 5.5 and 9.3 nm^{-2}, respectively, and the sum of the values were almost twice as much as that of Ti atoms. The result suggests the generation of a bulk $(NH_4)_2SO_4$ species. The N/S ratio estimated from EA (Table 5) had a same tendency as that evaluated by XPS: the N/S ratio decrease with increasing the reaction temperature. In AR-373K, the N/S ratio was 1.7 and was close to 2, which was the theoretical value of chemical composition of $(NH_4)_2SO_4$. Thus, most part of SO_4^{2-} species is present as a $(NH_4)_2SO_4$ salt in AR-373K. However, the N/S ratio by the XPS analysis is 0.41, which was almost half of the experimental value of the reference $(NH_4)_2SO_4$ powder (Table 4). The discrepancy between N/S ratios estimated from EA and XPS could be interpreted by considering the generation of the bulk $(NH_4)_2SO_4$ species. XPS analysis is more sensitive to surface-coordinated SO_4^{2-} species than bulk $(NH_4)_2SO_4$ species. The N/S ratio estimated from XPS should be lower than the real amount of the $(NH_4)_2SO_4$ species, which was estimated from the EA, when the $(NH_4)_2SO_4$ species has a bulk structure. Thus, the lower N/S ratio by XPS than that by EA also implies the generation of the bulk $(NH_4)_2SO_4$ species.

Table 5. Results of elemental analysis

Sample	Concentration (wt%)		Surface density (nm^{-2})		N/S
	S	N	S	N	(atom/atom)
BR	0.06	0	0.09	0	0
AR-373K	3.5	2.6	5.5	9.3	1.7
AR-433K	2.6	1.6	4.1	5.6	1.4
AR-553K	1.7	0.64	2.7	2.3	0.85

Structure of the ammonium sulfate species and deactivation mechanism

N_2 adsorption/desorption experiments revealed the decrease of the S_{tot} after the reaction, which was mainly due to the decrease of the S_{int}. The decrease of the S_{int} is not due to the aggregation of the TiO_2 particles during the reaction because the crystalline size of the TiO_2 particles did not change after the reaction (Table 1). FTIR, TG-DTA, XPS, and EA revealed the generation of the bulk $(NH_4)_2SO_4$ species on the TiO_2 surface after the reaction. The amount of $(NH_4)_2SO_4$ in AR-373K, which contains the largest amount of S and N atoms among the three catalyst after the reaction, is calculated to be 12wt% assuming that the all the N atoms, which were estimated from EA, exist in the $(NH_4)_2SO_4$ form. However, the XRD diffraction peak of the bulk $(NH_4)_2SO_4$ species was not observed in AR-373K, which implies that the generated bulk $(NH_4)_2SO_4$ species has amorphous structure. Thus, the generated bulk $(NH_4)_2SO_4$ species plugged the pores of the catalysts, which resulted in the decrease of the S_{int} (Fig. 9).

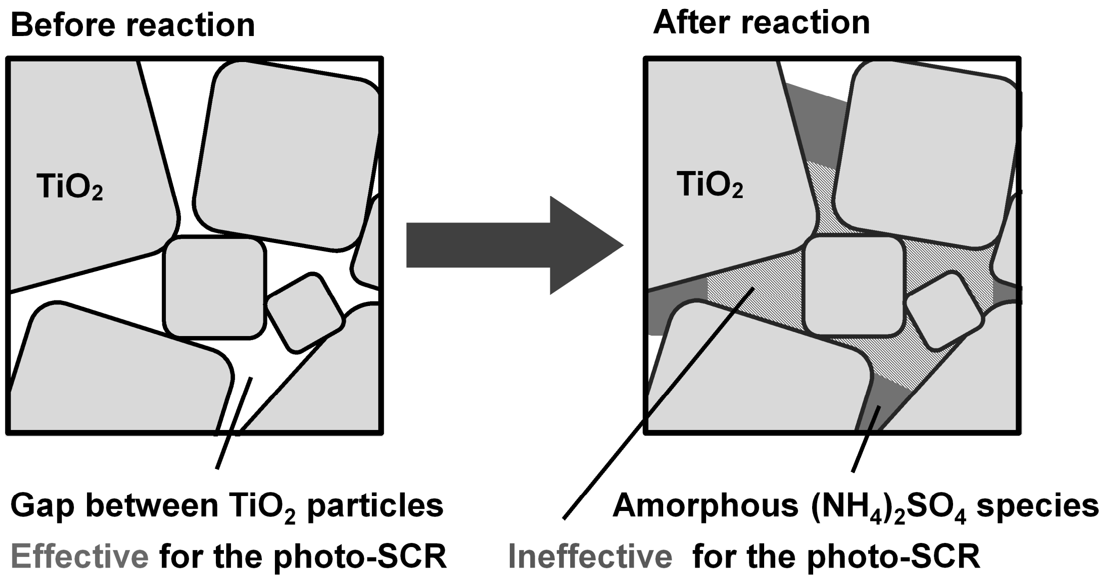

Figure 9. Deposition model of sulfate species of the catalysts.

The amount of the $(NH_4)_2SO_4$ species decreased with increasing the reaction temperature. Fig. 10 shows a correlation between the S_{tot} and the contents of N and S estimated from the EA. The increment of the contents of S and N drastically decreased the S_{tot}. FTIR analysis revealed two SO_4^{2-}

species: one is the $(NH_4)_2SO_4$ species and the other is the surface coordinated SO_4^{2-} species. The negative linear correlation for N contents strongly suggests that the decrease of the S_{tot} is because of the generation of not the surface coordinated SO_4^{2-} species but the bulk $(NH_4)_2SO_4$ species. The conversion of NO after 300 min of the reaction was plotted vs. the S_{tot} (Fig. 11). The strong positive and linear correlation was obtained, which indicates that the decrease of the S_{tot} results in the decrease of the conversion of NO. Based on the above discussion, we concluded that the generation of the $(NH_4)_2SO_4$ species plugged a part of the mesopores derived from the gap between the TiO_2 particles, which resulted in the decrease of the S_{tot} and the deactivation of the catalyst.

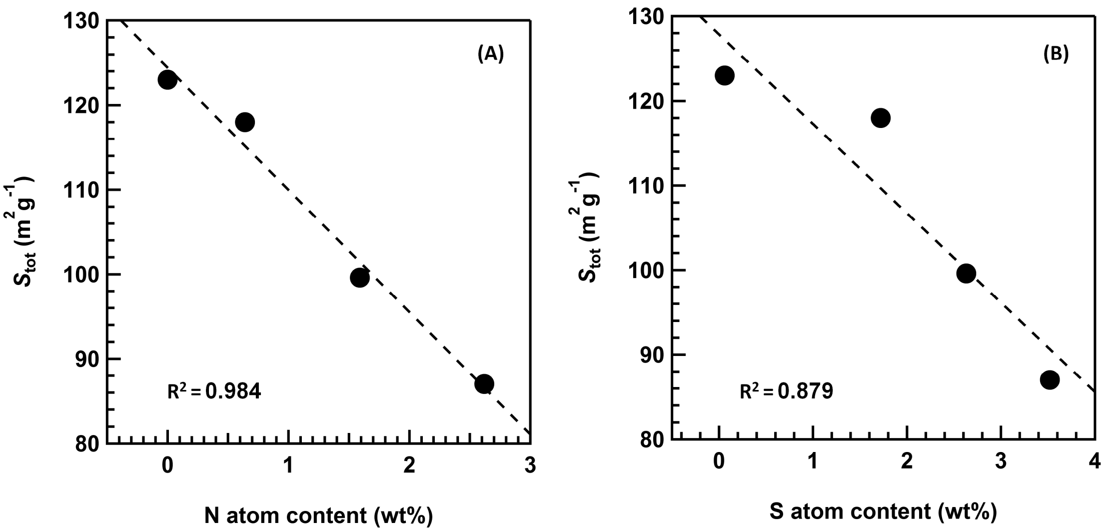

Figure 10. Effect of the contents of N atoms (A) and S atoms (B) on the S_{tot} estimated from the *V–t* plots.

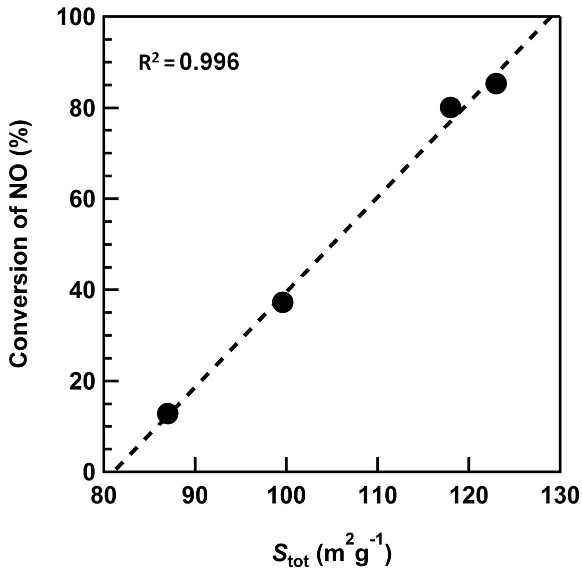

Figure 11. Effect of the the S_{tot} estimated from the *V–t* plots on the conversion of NO after 300 min of the photo-SCR at various temperatures.

Conclusions

In this study, tolerance to SO_2 gas was investigated in the photo-SCR of with NH_3 over the TiO_2 photocatalyst. Introduction of SO_2 drastically decreased the conversion of NO at 373 K. The increment of the reaction temperature drastically improved the stability of the catalyst and, at 553 K, the deactivation was not observed for 300 min of the reaction. FTIR and XPS results suggest that two SO_4^{2-} species exist on the TiO_2 surface: the surface coordinated SO_4^{2-} species and the free SO_4^{2-} species as a bulk $(NH_4)_2SO_4$ formed after the photocatalytic reaction. The deactivation occurs due to a pore plugging by the deposition of $(NH_4)_2SO_4$ species on the TiO_2 surface on the basis of the correlation among the contents of N and S atoms after reaction, the S_{tot} estimated from *V–t* plots, and the photocatalytic activity.

References

[1] H. Bosch, F. Janssen, *Catal. Today* **1988**, *2*, 369-379.

[2] G. Busca, L. Lietti, G. Ramis, F. Berti, *Appl. Catal. B* **1998**, *18*, 1-36.

[3] L. Singoredjo, R. Korver, F. Kapteijn, J. Moulijn, *Appl. Catal. B* **1992**, *1*, 297-316.

[4] F. Kapteijn, L. Singoredjo, A. Andreini, J. A. Moulijn, *Appl. Catal. B* **1994**, *3*, 173-189.

[5] R. Q. Long, R. T. Yang, R. Chang, *Chem. Commun.* **2002**, 452-453.

[6] J. Li, J. Chen, R. Ke, C. Luo, J. Hao, *Catal. Commun.* **2007**, *8*, 1896-1900.

[7] X. Tang, J. Hao, H. Yi, J. Li, *Catal. Today* **2007**, *126*, 406-411.

[8] J. Li, H. Chang, L. Ma, J. Hao, R. T. Yang, *Catal. Today* **2011**, *175*, 147-156.

[9] W. Sjoerd Kijlstra, M. Biervliet, E. K. Poels, A. Bliek, *Appl. Catal. B* **1998**, *16*, 327-337.

[10] S. Yamazoe, T. Okumura, K. Teramura, T. Tanaka, *Catal. Today* **2006**, *111*, 266-270.

[11] K. Teramura, T. Tanaka, T. Funabiki, *Langmuir* **2003**, *19*, 1209-1214.

[12] K. Teramura, T. Tanaka, S. Yamazoe, K. Arakaki, T. Funabiki, *Appl. Catal. B* **2004**, *53*, 29-36.

[13] S. Yamazoe, Y. Masutani, K. Teramura, Y. Hitomi, T. Shishido, T. Tanaka, *Appl. Catal. B* **2008**, *83*, 123-130.

[14] A. Yamamoto, Y. Mizuno, K. Teramura, T. Shishido, T. Tanaka, *Catal. Sci. Technol.* **2013**, *3*, 1771-1775.

[15] A. Yamamoto, Y. Mizuno, K. Teramura, S. Hosokawa, T. Shishido, T. Tanaka, *Catal. Sci. Technol.* **2015**, *5*, 556-561.

[16] Y. Ji, Y. Luo, *J. Phys. Chem. C* **2014**, *118*, 6359-6364.

[17] S. Yamazoe, K. Teramura, Y. Hitomi, T. Shishido, T. Tanaka, *J. Phys. Chem. C* **2007**, *111*, 14189-14197.

[18] Y. Chou, Y. Ku, *Front. Environ. Sci. Eng.* **2012**, *6*, 149-155.

[19] J. H. Scofield, *J. Electron. Spectrosc. Relat. Phenom.* **1976**, *8*, 129-137.

[20] J. P. Chen, R. T. Yang, *J. Catal.* **1993**, *139*, 277-288.

[21] D. C. Hague, M. J. Mayo, *J. Am. Ceram. Soc.* **1994**, *77*, 1957-1960.

[22] W. D. Halstead, *J. Appl. Chem.* **1970**, *20*, 129-132.

[23] B. J. Lindberg, *Acta Chem. Scand.* **1970**, *24*, 3661-3671.

[24] J. A. Rodriguez, T. Jirsak, G. Liu, J. Hrbek, J. Dvorak, A. Maiti, *J. Am. Chem. Soc.* **2001**, *123*, 9597-9605.

[25] J. Haubrich, R. G. Quiller, L. Benz, Z. Liu, C. M. Friend, *Langmuir* **2010**, *26*, 2445-2451.

[26] Y. Lu, D.-j. Choi, J. Nelson, O. B. Yang, B. A. Parkinson, *J. Electrochem. Soc.* **2006**, *153*, E131.

Chapter 5

Noble-metal-free NO_x Storage over Ba-modified TiO_2 Photocatalysts under UV-light Irradiation at Low Temperatures

Abstract

Photo-assisted nitrogen oxides (NO_x) storage was investigated over the barium-modified titanium dioxide (Ba/TiO_2) photocatalysts under UV-light irradiation at a high concentration of nitrogen monoxide (NO) of 200 ppm and a high gas hourly space velocity (GHSV) of 50,000 h^{-1}. The NO removal efficiency was kept > 99% during the 1020 s interval from the start of the reaction over the Ba/TiO_2 photocatalyst. The temperature-programed desorption (TPD) measurement and X-ray diffraction (XRD) technique revealed that barium oxide (BaO) species functioned as a NO_x storage material even at low temperatures, which result in improvement of the performance of the photo-assisted NO_x storage.

Introduction

Lean-burn and diesel engines are one of the most important technologies to improve the fuel efficiency of internal combustion engines and reduce carbon dioxide (CO_2) emissions. Significant fuel economy can be achieved when the engines operate under lean conditions of an air-to-fuel (A/F) ratio of approximately 20–65.[1] The conventional three-way catalyst is not capable of efficiently decomposing NO_x in the exhaust gas from the engines, although it can reduce NO_x in the stoichiometric condition at an A/F ratio of 14.7.[2-3] The NO_x removal at high A/F ratios was performed using catalytic processes such as selective catalytic reduction (SCR)[4-5] and NO_x storage and reduction (NSR).[6-8]

In the SCR system, urea is injected into the exhaust gas and decomposes into ammonia (NH_3) and CO_2. The NH_3 reacts with NO_x in the exhaust gas to form harmless nitrogen (N_2) under the lean condition. This technology is widely used in diesel engines and motor vehicles using Fe- or Cu-zeolite catalysts.[9-13] Alternatively, the NSR catalyst (typically, $Pt/BaO/Al_2O_3$) operates under lean and rich conditions. NO_x was oxidised over Pt and stored as nitrite (NO_2^-) or nitrate (NO_3^-) species under the lean condition, where barium oxide (BaO) functions as a NO_x storage material.[14] After the NO_x storage period under the lean condition (approximately 60–90 s), the engines are switched to the fuel-rich condition for a short period (approximately 3–5 s) by injecting fuels, where the stored NO_x is released and reduced into harmless N_2 over Pt.[14] The cycling operation of the lean and rich conditions provides high NO_x removal efficiency.[15] However, these SCR and NSR catalysts cannot reduce NO_x efficiently below 423 K.[16-18] In the urea-SCR system, according to the reports of the International Council for Clean Transportation (ICCT), urea injection could not start for approximately 800 s during the cold start test in the world harmonized transient cycle (WHTC) because the temperature of the exhaust gas was too low.[16] Controlling the NO_x emission under the cold start condition is a key and urgent task to lower the total emission of NO_x.

We have focused on TiO_2 photocatalysts as NO_x storage materials to reduce NO_x emissions in the cold start condition from the viewpoint of non-toxicity, low operating temperature, and rapid response to light. Under the cold start condition, utilising the photocatalysts enable the de-NO_x system to work at the same time that the engine starts. There are many reports concerning the oxidation of NO over TiO_2-based photocatalysts under light irradiation.[19-28] In these reports, NO in the gas phase was oxidised to NO_2 and surface NO_x^- species and stored on the TiO_2 surface. Most of the researchers investigated the oxidation of NO over TiO_2 photocatalysts at very low concentrations of NO (less than 10 ppm) and/or at low gas hourly space velocity (GHSV) of 10–1000 h^{-1} because their objective was the removal of NO_x in air [22, 29] and elucidation of the reaction mechanism of NO oxidation.[24-25, 30-32] These conditions were quite different from those of practical exhaust gas in lean-burn engines (typically, concentration of NO > 200 ppm and GHSV > 50,000 h^{-1}). Thus, the potential of the TiO_2 photocatalyst for NO_x storage materials in the cold start condition has not been investigated. In this research, we investigated photo-assisted NO_x storage at a high concentration of NO and high GHSV to assess the potential of the TiO_2 photocatalyst. In addition, the role of Ba modification was examined in the performance of the photo-assisted NO_x storage.

Experimental

Catalyst preparation

TiO_2 powder (ST-01, anatase) was purchased from Ishihara Sangyo Kaisha, Ltd. $Ba(NO_3)_2$ (wako, 99.9%) was used without further purification. $Ba(NO_3)_2$ was impregnated on the TiO_2 powder using a 20 mL of water as a solvent. The catalyst powder was tabletted and grinded into granules with a diameter of 300–600 μm using 25 and 50 mesh sieves.

Photocatalytic reaction

Photo-assisted NO_x storage was carried out using a conventional fixed bed flow system at an atmospheric pressure. A quarts reactor (H12 mm × W10 mm × D1.0 mm, the reactor volume: 0.12 mL) was used for the reaction. 0.13 g of the catalyst granules were introduced to the reactor and then pretreated at various temperatures (298–873 K) in a 10% O_2/He gas mixture at a flow rate of 50 mL min^{-1} for 1 h. The reaction gas composition was as follows: NO (200ppm), O_2 (3%), He (balance). A 300 W Xe lamp (Perkin-Elmer PE300BF) was used as a light source. The outlet concentration of NO_x ($NO+NO_2$) was measured using a portable gas analyzer (Horiba PG-335). N_2 and N_2O products were analyzed by Shimadzu GC-8A TCD gas chromatographs. The dead time was obtained as the time at which the concentration of NO_x exceeded 2 ppm (99% of the conversion of NO) in the outlet gas. NO_x storage capability (NSC) was calculated as the total amount of the NO_x stored for 1 h from the start of the reaction.

Characterization

The specific surface areas (SSA) was obtained by Brunauer–Emmett–Teller (BET) method using N_2 adsorption isotherm measured at 77 K. X-ray diffraction (XRD) measurement was performed on a Rigaku Ultima IV X-ray diffractometer with Cu-Kα radiation (λ = 1.5418 Å). The crystallite size was determined by the Scherrer's equation using the diffraction peak of anatase TiO_2 (101) plane (2θ = 25.2°) by the Scherrer equation:

$$d = \frac{K\lambda}{\beta \cos\theta}$$

where d is the crystallite size, λ is the wavelength of the X-ray radiation (CuKα, λ = 1.5406 Å), K is the taken as 0.89, and β is the full width at half maximum (FWHM) of the diffraction peak. A diffraction peak of single-crystal silicon (111) (2θ = 28.4°) was used as the standard material to estimate instrumental peak broadening. Temperature-programed desorption (TPD) experiments were performed using the same experimental set-up as the reaction in a 10% O_2/He gas mixture at a flow rate of 50 mL min^{-1}. After the temperature was kept at 373 K for 30 min, the TPD measurement was started at a heating rate of 5 K min^{-1} up to 923 K.

Results and discussion

Fig. 1 shows the time course of the outlet concentrations of NO_x (= NO + NO_2) for NO_x storage under various reaction conditions after the pretreatment at 773 K in a 10% O_2/He gas mixture. Without a catalyst, the concentration of NO_x increased with the introduction of NO and immediately became 200 ppm. However, the concentration of NO was less than 2 ppm during the initial 530 s of the reaction (conversion of NO > 99%) over TiO_2. After the dead time for the breakthrough of NO_x, the concentration of NO gradually increased with the reaction time and became 175 ppm after 3 h (not saturated), where N_2 and N_2O products were not detected by the TCD-GCs. The concentration of NO became 200 ppm after 20 h of the reaction, where the inlet NO gas slipped through the catalyst possibly because of the saturation of the TiO_2 surface by the adsorbed NO_x species. The total amount of the stored NO_x species after 20 h was calculated to be 426 μmol g^{-1}. The surface density of NO_x species was calculated to be 1.4 nm^{-2}. When the TiO_2 (100) surface is considered, the density of the surface Ti atoms was 7.0 nm^{-2}, and 20% of the surface Ti sites are occupied by the adsorbed NO_x species assuming a one-to-one relationship between the stored NO_x species and surface Ti sites.

The addition of Ba drastically enhanced the dead time of the NO_x slip to 1020 s, which was almost twice as long as that of the TiO_2 photocatalyst. The dead time value meets the demand (800 s) for the cold start condition reported by the ICCT.[16] The NO_x storage capability (NSC) is defined as the amount of stored NO_x after 1 h from the start of the reaction and was calculated to be 252 μmol g^{-1}. For the typical NSR catalyst, Pt/Ba/Al_2O_3, the NSC at 473 and 573 K was reported to be 177 and 581 μmol g^{-1}, respectively. The NSC of the Ba/TiO_2 photocatalyst was comparable to that of the typical NSR catalyst containing precious noble metals (Pt). Thus, the utilisation of photocatalysts enables us to eliminate the use of expensive and rare precious metals from the de-NO_x catalyst.

The NO_x storage was hardly observed without UV-light irradiation (Fig. 1, no dead time), and the NSC was calculated to be 88.4 μmol g^{-1}. The result clearly indicates that the UV-light irradiation accelerated the activity of the NO_x storage. In the absence of O_2, the reaction hardly proceeded, as observed in Fig. 1. In previous reports, active oxygen radicals derived from molecular O_2 (*e.g.*, O_2^-, O^-, and OH radicals) reacted with the NO gas to form NO_x species on the TiO_2 surface.[24-25, 29] The significant impact of UV-light and O_2 gas on the activity suggests that the reaction proceeded via O_2 radicals generated under UV-light irradiation, as displayed in the previous reports.[24]

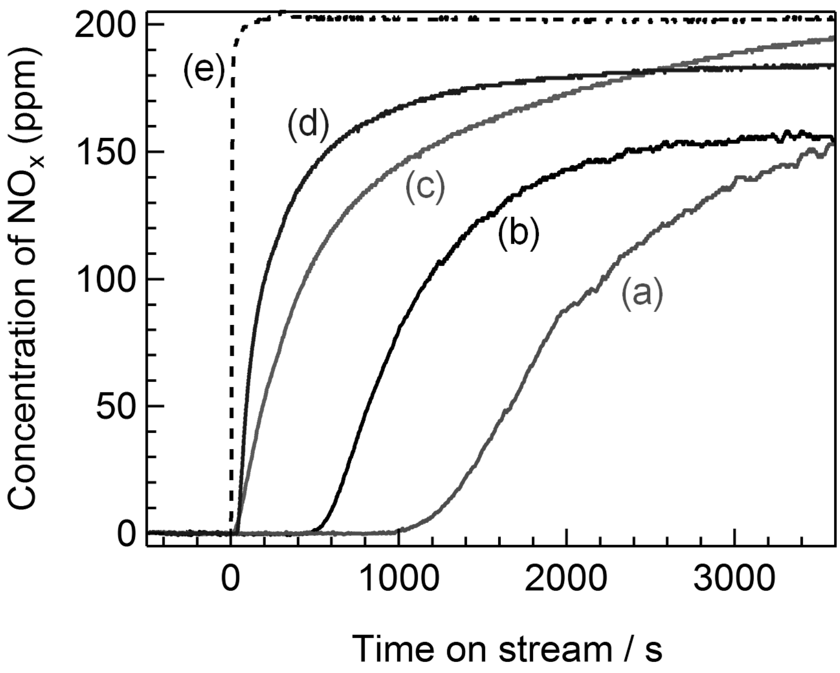

Figure 1. Time course of the NO_x storage under various reaction conditions after the pretreatment at 773 K. (a): over 500 μmol g^{-1} Ba/TiO_2 catalyst under UV-light irradiation, (b): over TiO_2 catalyst under UV-light irradiation, (c): over 500 μmol g^{-1} Ba/TiO_2 catalyst in the dark, (d): over 500 μmol g^{-1} Ba/TiO_2 catalyst under UV-light irradiation without O_2 gas, and (e): without catalyst.

Fig. 2 shows the time course of the NO_x storage at various pretreatment temperatures over the TiO_2 and Ba/TiO_2 catalysts. The NSC and dead time drastically decreased with the pretreatment temperature using the TiO_2 photocatalyst. Only the diffraction pattern of anatase TiO_2 was observed in the XRD patterns of all the TiO_2 samples before and after the reaction (the date is not shown). As observed in Table 1 (Entries 1–3), the crystalline size of TiO_2 increased from 8.9 to 28 nm, and the specific surface area (SSA) of the catalysts decreased from 292 to 50.7 m^2 g^{-1} after the pretreatment at 873 K. The positive correlation of the NSC and SSA strongly indicates that the SSA has a significant effect on the NSC for the TiO_2 photocatalyst.

Ba/TiO_2 exhibits high resistance to the high-temperature pretreatment; the decrease in the activity of the Ba/TiO_2 catalysts by elevating the pretreatment temperature was smaller than that observed for the TiO_2 catalyst (Fig. 2 and Entry 8, 10, and 11 in Table 1). The SSA of the Ba/TiO_2

catalyst was almost stable up to 773 K and then decreased at 873 K. The pretreatment at 873 K slightly decreased the crystalline size of TiO_2 in the Ba/TiO_2 photocatalyst from 7.7 to 12 nm, although this value largely decreased for the TiO_2 photocatalyst. This result clearly indicates that the Ba modification suppressed the growth of TiO_2 particles. Similar effects were previously reported for metal doping into TiO_2 (*e.g.,* Si, Zr,[33] La,[34] and Al[35]). The Ba loading enhanced the thermal stability of the catalyst, which should be one of the reasons for the higher NSC of the Ba/TiO_2 catalyst than that of the TiO_2 catalyst. The thermal stability is an advantage in the practical use of lean-burn engines.

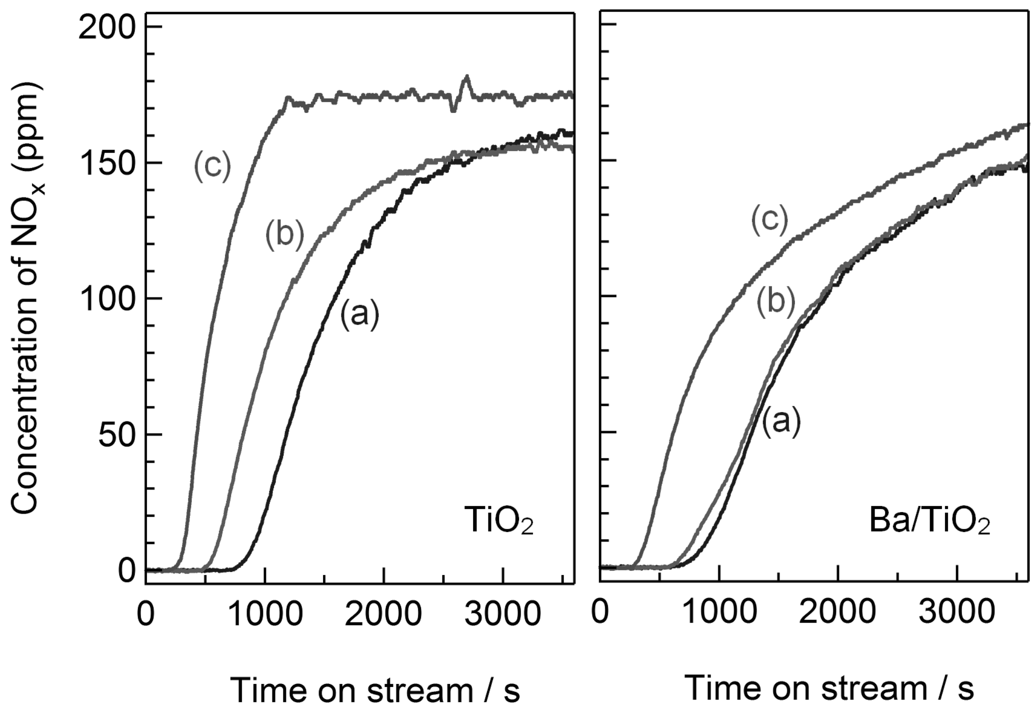

Figure 2. Time course of the NO_x storage at the pretreatment temperatures of 673 K (a), 773 K (b), and 873 K (c). NO: 200ppm, O_2: 3%, He balance.

Table 1. The result of the NO_x storage, the BET specific surface area, and the crystalline size of the TiO_2 particle.

Entry	Catalyst	Temp.[a] / K	SSA[b] / m^2 g^{-1}		d [c] / nm		NSC [f] / µmol g^{-1}	Dead time [g] / s
			as-syn.[d]	AR[e]	as-syn.[d]	AR[e]		
1	TiO_2	673	292	235	7.7	8.9	203	573
2	TiO_2	773	292	185	7.7	11	177	530
3	TiO_2	873	292	50.7	7.7	28	83.6	58
4	Ba/TiO_2[h]	298	180	188	7.7	7.9	156	97
5	Ba/TiO_2[h]	473	180	188	7.7	7.8	124	33
6	Ba/TiO_2[h]	573	180	187	7.7	8.0	108	100
7	Ba/TiO_2[h]	623	180	166	7.7	7.9	125	170
8	Ba/TiO_2[h]	673	180	155	7.7	8.3	230	727
9	Ba/TiO_2[h]	723	180	166	7.7	8.3	228	629
10	Ba/TiO_2[h]	773	180	154	7.7	8.8	225	650
11	Ba/TiO_2[h]	873	180	108	7.7	12	175	306

[a] Pretreatment temperature. [b] Specific surface area determined by the BET methods. [c] Crystalline size of the TiO_2 particles. [d] As-synthesized. [e] After the NO_x storage reaction. [f] NO_x storage capacity after 1 h of the reaction. [g] Reaction time after which the outlet concentration of NO_x was less than 2 ppm. [h] Ba loading: 1000 µmol g^{-1}.

The effect of the pretreatment temperature on the activity of the Ba/TiO_2 catalyst is summarised in Table 1. In the pretreatment temperature range of 298–573 K, the NSC of the Ba/TiO_2 catalyst (Entries 4–6 in Table 1) was lower than that of the bare TiO_2 catalyst after the pretreatment at 773 K (Entry 2) even though the crystalline size of TiO_2 in the Ba/TiO_2 catalyst was smaller than that in the TiO_2 catalyst. The generation of crystalline $Ba(NO_3)_2$ was observed in the as-prepared Ba/TiO_2 catalyst using XRD (Fig. 3), which suggests that the decrease in the NSC occurs because the TiO_2 surface is covered with the impregnated $Ba(NO_3)_2$ species. The NSC increased drastically upon increasing the pretreatment temperature from 573 to 673 K. The increase in the NSC was not due to the change in the SSA because the SSA decreased from 187 to 155 m^2 g^{-1}. The crystalline size of TiO_2 did not change in the pretreatment temperature region of 573–673 K, which indicates that the growth of TiO_2 particles did not occur during the pretreatment in this temperature region. To investigate the effect of the pretreatment temperature, temperature programed desorption (TPD) experiments were performed using the same experimental set-up as the reaction in a 10% O_2/He gas mixture, and the result of the as-prepared Ba/TiO_2 catalysts is presented in Fig. 4 (experimental detail in the ESI). By integrating the TPD profiles, the total desorption amount of NO_x (NO+NO_2) was calculated to be 242 μmol, which was consistent with the loading amount of NO_3^- ions in the Ba/TiO_2 catalyst (260 μmol). The TPD spectrum was reasonably fitted using three Gaussian functions with peaks at 694, 806, and 840 K (the fitting result is presented in Fig. 5). The intensity of crystalline $Ba(NO_3)_2$ in Fig. 3 decreased after the pretreatment at 773 K and completely disappeared at 873 K. The XRD results reveal that the TPD peaks at the higher temperatures of 806 and 840 K were due to the decomposition of crystalline $Ba(NO_3)_2$ observed in the XRD patterns. The peak at temperatures below 694 K can possibly be attributed to $Ba(NO_3)_2$ on the TiO_2 surface. The desorption of NO started at approximately 600 K, which corresponded to the uptake temperature of the NSC of 623 K. The generation of NO was observed in TPD experiments, as shown in Fig. 4. In addition, the concentration of NO in thermal equilibrium was calculated using the concentration of NO_x and O_2 (3%) (TPD experimental condition) and thermodynamic parameters of the following equation from the NIST Chemistry WebBook[36]:

$$NO + 1/2O_2 \rightleftarrows NO_2 \qquad K = P_{NO2}/P_{NO}P_{O2}^{1/2} \tag{1}$$

where, P_x is the partial pressure of species x. The concentration of NO detected was much lower than that calculated especially at temperatures below 760 K, which indicates that NO_2 was first generated at temperatures below 850 K. Thus, the decomposition of $Ba(NO_3)_2$ proceeds as described in the following reaction (2).[37-38]

$$Ba(NO_3)_2 \rightarrow BaO + 2NO_2 + 1/2O_2 \tag{2}$$

Thus, we concluded that the increase of the NSC between 623 and 673 K was due to the generation of BaO, as observed in Eq. (2), and the generated BaO functions as a NO_x storage material in the photo-assisted NO_x storage as well as the typical NSR catalyst. The NSC decreased at the pretreatment temperature of 873 K. At this temperature, the SSA decreased, and the crystalline size of TiO_2 increased. In addition, the diffraction peaks of the $BaTiO_3$ mixed oxide appeared (Fig. 3). Thus, the decrease in the NSC at 873 K could be due to the decrease in the SSA of the catalyst and/or the generation of the $BaTiO_3$ mixed oxide.

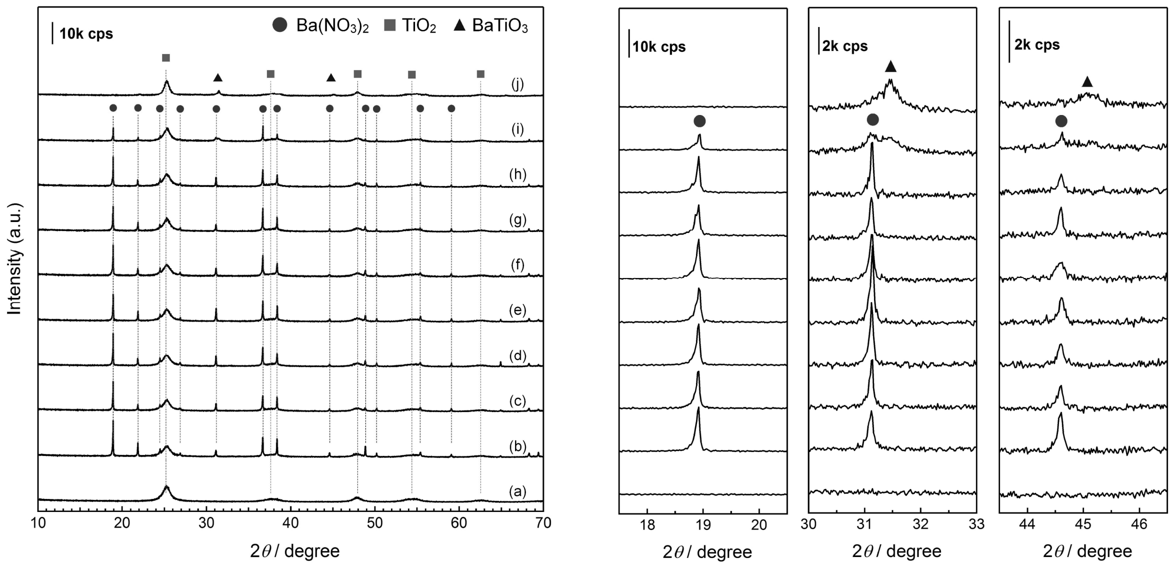

Figure 3. XRD patterns of the catalysts before and after the reaction at various pretreatment temperatures. TiO_2 before the reaction (a), Ba/TiO_2 before the reaction (b), and Ba/TiO_2 after the reaction at pretreatment temperatures of 298 K (c), 573 K (d), 623 K (e), 673 K (f), 723 K (g), 773 K (h), and 873 K (i).

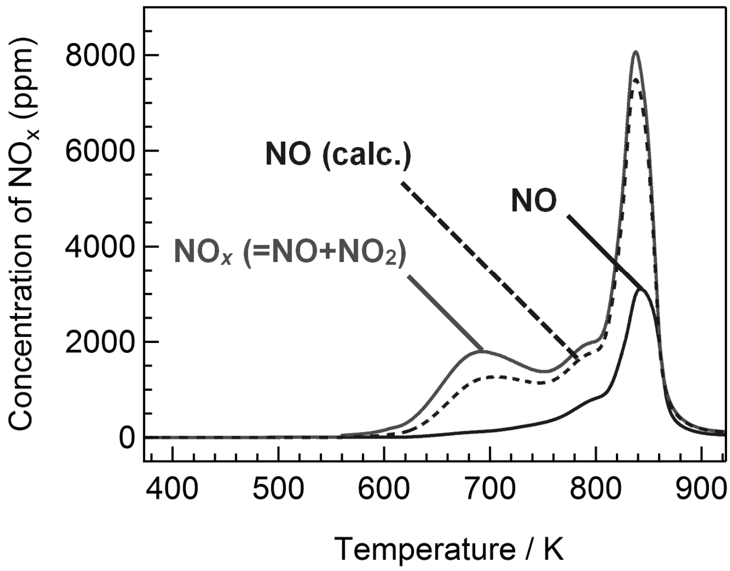

Figure 4. TPD profiles of 1000 μmol g^{-1} Ba/TiO_2 catalyst in a 10% O_2/He gas mixture. NO (calc.) was calculated using the equilibrium constants of eq. (1) and the concentration of NO_x and O_2 (3%) in the TPD experiment.

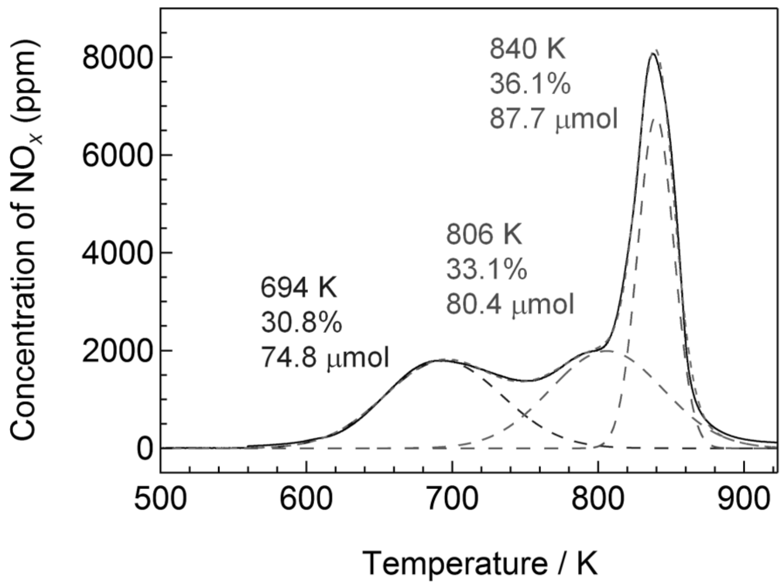

Figure 5. Peak deconvolution of the TPD profile of 1000 μmol g^{-1} Ba/TiO_2 using three Gaussian functions.

Conclusions

In summary, we have developed an effective NO_x storage method at a low temperature using TiO_2-based photocatalysts under UV-light irradiation. We observed that the Ba modification on a TiO_2 surface drastically improved the performance of the catalyst. The Ba/TiO_2 photocatalyst exhibited 1020 s of dead time, which is sufficient for the desired value (800 s) reported by the ICCT. The effect of the pretreatment temperature was also studied, and two positive effects of Ba modification on the NSC were proposed: (i) the Ba modification inhibits the densification of TiO_2 particles, which helped to maintain the high SSA of TiO_2 and (ii) the BaO species, which was generated from the decomposition of $Ba(NO_3)_2$, works as a NO_x storage material over the photocatalysts at low temperatures. We concluded that TiO_2 and Ba/TiO_2 are promising for NO_x storage materials at low temperatures and have the potential to reduce NO_x emissions in the cold start condition.

Reference

[1] N. Takahashi, H. Shinjoh, T. Iijima, T. Suzuki, K. Yamazaki, K. Yokota, H. Suzuki, N. Miyoshi, S.-i. Matsumoto, T. Tanizawa, T. Tanaka, S.-s. Tateishi, K. Kasahara, *Catal. Today* **1996**, *27*, 63-69.

[2] G. Centi, G. E. Arena, S. Perathoner, *J. Catal.* **2003**, *216*, 443-454.

[3] J. Kašpar, P. Fornasiero, N. Hickey, *Catal. Today* **2003**, *77*, 419-449.

[4] M. Koebel, M. Elsener, M. Kleemann, *Catal. Today* **2000**, *59*, 335-345.

[5] J. Baik, S. Yim, I.-S. Nam, Y. Mok, J.-H. Lee, B. Cho, S. Oh, *Top. Catal.* **2004**, *30-31*, 37-41.

[6] E. Fridell, M. Skoglundh, B. Westerberg, S. Johansson, G. Smedler, *J. Catal.* **1999**, *183*, 196-209.

[7] L. Lietti, P. Forzatti, I. Nova, E. Tronconi, *J. Catal.* **2001**, *204*, 175-191.

[8] E. C. Corbos, M. Haneda, X. Courtois, P. Marecot, D. Duprez, H. Hamada, *Appl. Catal. A* **2009**, *365*, 187-193.

[9] J. A. Sullivan, J. Cunningham, M. A. Morris, K. Keneavey, *Appl. Catal. B* **1995**, *7*, 137-151.

[10] G. Busca, L. Lietti, G. Ramis, F. Berti, *Appl. Catal. B* **1998**, *18*, 1-36.

[11] R. Q. Long, R. T. Yang, *J. Am. Chem. Soc.* **1999**, *121*, 5595-5596.

[12] A.-Z. Ma, W. Grunert, *Chem. Commun.* **1999**, 71-72.

[13] R. Q. Long, R. T. Yang, *J. Catal.* **2002**, *207*, 274-285.

[14] G. Liu, P.-X. Gao, *Catal. Sci. Technol.* **2011**, *1*, 552-568.

[15] W. S. Epling, L. E. Campbell, A. Yezerets, N. W. Currier, J. E. Parks, *Cat. Rev. - Sci. Eng.* **2004**, *46*, 163-245.

[16] L. Dana, K. Fanta, *Urban off-cycle NO_x emissions from Euro IV/V trucks and buses* **2012**, http://www.theicct.org/urban-cycle-nox-emissions-euro-ivv-trucks-and-buses.

[17] N. Takahashi, K. Yamazaki, H. Sobukawa, H. Shinjoh, *Appl. Catal. B* **2007**, *70*, 198-204.

[18] J. Li, H. Chang, L. Ma, J. Hao, R. T. Yang, *Catal. Today* **2011**, *175*, 147-156.

[19] J. S. Dalton, P. A. Janes, N. G. Jones, J. A. Nicholson, K. R. Hallam, G. C. Allen, *Environ. Pollut.* **2002**, *120*, 415-422.

[20] S. Yin, H. Yamaki, M. Komatsu, Q. Zhang, J. Wang, Q. Tang, F. Saito, T. Sato, *Solid State Sciences* **2005**, *7*, 1479-1485.

[21] Y. Ohko, Y. Nakamura, N. Negishi, S. Matsuzawa, K. Takeuchi, *J. Photochem. Photobiol. A* **2009**, *205*, 28-33.

[22] K. Hashimoto, K. Sumida, S. Kitano, K. Yamamoto, N. Kondo, Y. Kera, H. Kominami, *Catal. Today* **2009**, *144*, 37-41.

[23] K. Hashimoto, K. Wasada, M. Osaki, E. Shono, K. Adachi, N. Toukai, H. Kominami, Y. Kera, *Appl. Catal. B* **2001**, *30*, 429-436.

[24] K. Hashimoto, K. Wasada, N. Toukai, H. Kominami, Y. Kera, *J. Photochem. Photobiol., A* **2000**, *136*, 103-109.

[25] J. Lasek, Y.-H. Yu, J. C. S. Wu, *J. Photochem. Photobiol. C: Photochem. Rev.* **2013**, *14*, 29-52.

[26] Y. Ishibai, J. Sato, S. Akita, T. Nishikawa, S. Miyagishi, *J. Photochem. Photobiol. A* **2007**, *188*, 106-111.

[27] M. M. Ballari, M. Hunger, G. Hüsken, H. J. H. Brouwers, *Appl. Catal. B* **2010**, *95*, 245-254.

[28] B. N. Shelimov, N. N. Tolkachev, O. P. Tkachenko, G. N. Baeva, K. V. Klementiev, A. Y. Stakheev, V. B. Kazansky, *J. Photochem. Photobiol. A* **2008**, *195*, 81-88.

[29] T. Ibusuki, K. Takeuchi, *J. Mol. Catal.* **1994**, *88*, 93-102.

[30] R. Dillert, A. Engel, Gro, P. Lindner, D. W. Bahnemann, *PCCP* **2013**, *15*, 20876-20886.

[31] A. Folli, S. B. Campbell, J. A. Anderson, D. E. Macphee, *J. Photochem. Photobiol. A* **2011**, *220*, 85-93.

[32] Q. Wu, R. van de Krol, *J. Am. Chem. Soc.* **2012**, *134*, 9369-9375.

[33] X. Fu, L. A. Clark, Q. Yang, M. A. Anderson, *Environ. Sci. Technol.* **1996**, *30*, 647-653.

[34] J. Liqiang, S. Xiaojun, X. Baifu, W. Baiqi, C. Weimin, F. Honggang, *J. Solid State Chem.* **2004**, *177*, 3375-3382.

[35] A. M. Soylu, M. Polat, D. A. Erdogan, Z. Say, C. Yıldırım, Ö. Birer, E. Ozensoy, *Appl. Surf. Sci.* **2014**, *318*, 142-149.

[36] P. Linstrom, W. Mallard, Eds., National Institute of Standards and Technology, Gaithersburg MD, 20899, http://webbook.nist.gov, (retrieved November 20826, 22014).

[37] G. Zhou, T. Luo, R. J. Gorte, *Appl. Catal. B* **2006**, *64*, 88-95.

[38] X. Wang, Y. Yu, H. He, *Appl. Catal. B* **2010**, *100*, 19-30.

Chapter 6

NO_x Storage over Ba-modified TiO_2 Photocatalysts under UV-light Irradiation: Effect of Ba Loading and Structure of Ba Oxide Species

Abstract

Effect of Ba loading in photo-assisted NO_x storage over Ba-modified TiO_2 photocatalysts under UV-light irradiation was investigated by temperature programed desorption (TPD), X-ray diffraction (XRD), X-ray photoelectron spectroscopy (XPS), transmission electron microscopy (TEM), and diffuse reflectance infrared Fourier transform spectroscopy (DRIFT). The Ba loading had a significant effect on the activity of NO_x storage; the activity increased with increasing the Ba loading up to 500 μmol g^{-1}, and the further increase of the Ba loading decreased the activity. Based on the TPD results, there were at least two $Ba(NO_3)_2$ species in the as-synthesized catalysts: surface and bulk $Ba(NO_3)_2$. The surface $Ba(NO_3)_2$ was decomposed to Ba oxide species during the pretreatment at 773 K, and the generated Ba oxide species improved the activity. On the other hand, the amount of the bulk $Ba(NO_3)_2$ increased with the Ba loading over 500 μmol g^{-1}, which caused the decrease of the activity. DRIFT investigations revealed that bulk BaO was not generated on a TiO_2 surface because nitrate species adsorbed on Ba sites were not observed in NO/O_2 gas under UV-light irradiation. DRIFT, XRD, XPS, and TEM results suggested that the surface Ba–Ti mixed oxides with an amorphous structure was generated during the pretreatment. Combined with the results of NO_x storage, the formed Ba–Ti mixed oxides functioned as an effective NO_x storage material, which improved the NO_x storage capacity.

Introduction

Control of NO_x emission in exhaust gas from engines is strongly required in terms of air purification. Many researchers and engineers have been challenged to develop efficient de-NO_x technologies.[1] At the stoichiometric air-to-fuel (A/F) ratio of 14.7, three way catalysts are used for the NO_x removal.[2-3] However, under lean conditions (air-rich, A/F ratio: 20–65), typical three way catalysts cannot efficiently decompose the NO_x to harmless N_2 although the lean operation of the engines leads to fuel economy and decreases of CO_2 emission.[4-5] Two technologies have been developed for the removal of NO_x under the lean condition: selective catalytic reduction (SCR) and NO_x storage and reduction (NSR). In the SCR, NH_3, which is produced by decomposition of urea, is introduced into the exhaust gas, and the introduced NH_3 reduces the NO_x to N_2. The SCR have been investigated by many researchers since 1970s. V_2O_5-based catalysts[6-8] and Fe- or Cu- zeolite catalysts[9] show high activity over 473 K. This technology is widely used in stationary emission sources and mobile emission sources including diesel engines in vehicles and trucks. However, the NO_x removal efficiency is low below 473 K.

Low-temperature removal of NO_x is highly desired in exhaust gas from vehicle engines. Regulation of NO_x emission has become severe year by year,[10] and a recent report by the International Council for Clean Transportation (ICCT) pointed out the impact of the NO_x emission in the initial stage of engine start-up on the total emission amounts; in the cold start condition below 473 K (approximately 800 s), urea cannot be injected because of the low activity of the catalyst to avoid ammonia slip.[11] Thus, development of low temperature technology for NO_x removal is urgent task to improve the total removal efficiency of NO_x in the cold start condition.

On the other hand, the NSR technology was firstly reported by Toyota researchers in 1995.[5, 12] The NSR catalyst is composed of three components: precious metals, alkali or alkali earth oxides, and supports (e.g., Pt/BaO/Al_2O_3).[4] In the lean condition, NO is oxidized on Pt sites and stored as nitrite (NO_2) or nitrate (NO_3^-) species. At that time, BaO functions as a NO_x storage material. After the NO_x storage in the lean condition, the engine is switched to the fuel-rich condition for a short time by injecting the fuels, and the stored NO_x^- is reduced by the injected fuels into N_2 over Pt sites.[4]

The lean and rich cycle operation provides the high NO_x removal efficiency.[13] However, the NSR catalysts also cannot reduce the NO_x efficiently at low temperatures below 473 K.[14]

Photocatalysts are promising materials in terms of such a low temperature operation. Until now, several photocatalysts have been reported in the NO oxidation: TiO_2,[15] N-doped TiO_2,[16] metal-modified TiO_2,[17-18], TiO_2–Al_2O_3 binary oxide.[19-20] The reaction mechanism of NO oxidation was also investigated over the TiO_2 photocatalysts.[21-28] Recently, we demonstrated the Ba-modified TiO_2 photocatalysts showed high activity at a practical condition (gas hourly space velocity: 50,000 h^{-1}, NO concentration: 200 ppm) under UV-light irradiation, and Ba modification of TiO_2 greatly enhanced the activity of NO_x storage at low temperature.[29] The activity was improved after the pretreatment in O_2/He gas over 673 K, and the temperature corresponded to the decomposition temperature of $Ba(NO_3)_2$ used as a Ba precursor. Thus, the activated Ba oxide species were generated during the pretreatment. The structure and the role of Ba oxide species is still unclear as the case now stands.

In Pt/BaO/Al_2O_3 system of a typical NSR catalyst, classically, BaO and $BaCO_3$ species were assumed to be NO_x storage materials.[4,13] On the other hand, BaO and Al_2O_3 react at high temperature (>1073 K) to form an aluminate phase, $BaAl_2O_4$.[30-32] It was previously reported that the $BaAl_2O_4$ was a better NO_x storage material than BaO and/or $BaCO_3$,[30-31] although other groups reported that the generation of $BaAl_2O_4$ decreased the performance.[33] In addition, TiO_2 was added to the NSR catalyst to improve the dispersion of Ba species using a strong interaction between Ba and Ti atoms,[34] and the tolerance to sulfur poisoning,[35-37] where the high temperature operations resulted in the generation of mix-oxide phase of Ti and Ba.[34,38] (e.g., $BaTiO_3$) In our photocatalytic system, $BaTiO_3$ phase was observed after the pretreatment in O_2/He at 873 K, and the generation caused the decrease of NO_x storage activity.[29] Thus, the generation of mixed oxide phase and the effect on the activity should be considered to explain the role of Ba oxide species. In the present paper, the structure and role of Ba oxide species were investigated in the photo-assisted NO_x storage at low temperature to elucidate the Ba oxide species active for the NO_x storage.

Experimental

Materials

TiO_2 (ST-01, Ishihara Sangyo Kaisha, Ltd) powder was used as purchased. Barium nitrate ($Ba(NO_3)_2$, 99.9%) and barium titanate ($BaTiO_3$) were purchased from Wako co. ltd. (japan). 100–1000 μmol g^{-1} Ba/TiO_2 catalysts were prepared by impregnation using a $Ba(NO_3)_2$ precursor and a water (20 mL) as a solvent.

Activity tests

Photo-assisted NO_x storage was carried out using a fixed bed flow system. The detail was shown elsewhere.[29] Briefly, 0.13 g catalyst granules (diameter: 300–600 μm) were added to a quarts reactor (12 mm × 10 mm × 1 mm, volume: 0.12 mL), and then pretreated at 773 K in 10% O_2/He gas at 50 mL min^{-1} for 1 h. The reaction gas (NO: 200ppm, O_2: 3%, He: balance) was flowed at 100 mL min^{-1}. A 300 W Xe lamp (Perkin-Elmer PE300BF) was used as a light source. The NO_x (NO+NO_2) in the outlet gas was analyzed using a portable gas analyzer (HORIBA PG-335). Dead time for NO_x breakthrough, which was defined as a time when the outlet concentration of NO_x reached to 2 ppm (conversion of NO: 99%), was used for NO_x breakthrough in the present research.

Characterization

N_2 adsorption measurement was performed on a Belsorp-miniII (BEL, Japan) at 77 K. The specific surface area (S_{BET}) was estimated from the N_2 adsorption isotherm using Brunauer–Emmett–Teller (BET) method. X-ray diffraction (XRD) measurement was carried out using a Rigaku Ultima IV X-ray diffractometer with Cu-Kα radiation (λ = 1.5406 Å). The crystallite size was determined by the Scherrer equation using the full width at half maximum (FWHM) of the diffraction peak of anatase TiO_2 (101) plane. Temperature-programed desorption (TPD) experiment was performed on the same experimental set-up as the activity test in 10% O_2/He gas at 50 mL min^{-1}. After the temperature was kept at 373 K for 30 min, the TPD measurement was started at a heating rate of 5 K min^{-1} up to 973 K. The increase of temperature was also monitored using a thermocouple and an integrator. In situ diffuse reflectance infrared Fourier transform (DRIFT) spectra were measured using an ISDR-600 FTIR spectrometer (JASCO, Japan) equipped with a mercury-cadmium-tellurium (MCT) detector cooled by liquid nitrogen at a resolution of 4 cm^{-1} with 16 co-added scans. The sample powder (50 mg) was placed in a diffuse reflectance cell, which was fitted by a potassium bromide (KBr) window at the top. The gas compositions of the pretreatment and the DRIFT experiment were the same as the activity tests. The catalyst was pretreated at 773 K, and then cooled to 373 K. A 200 W Hg–Xe lamp equipped with a collective lens (San-Ei Electric Co. Ltd., UVF-204S type C) was used as a light source. The background spectrum was measured after the pretreatment under a He gas flow at the 373 K. X-ray photoelectron spectroscopy (XPS) measurement was conducted on an ESCA-3400 spectrometer (Shimadzu, Japan). Sample was mounted on a silver sample holder by using a conductive carbon tape, and analyzed using Mg Kα radiation in a vacuum chamber in 0.1 eV steps. The position of the carbon peak (284.6 eV) for C1s was used to calibrate the binding energy for all the samples. The surface atomic ratio was estimated from the band areas of XPS of Ba 3d, and Ti 2p, and the corresponding relative sensitivity factors.[39] Transmission electron microscopy (TEM) observation was carried out with JEOL-1400 TEM (JEOL, Japan)

Result and discussions

Effect of Ba loading

Fig. 1A represents the time course of NO_x storage over Ba/TiO_2 catalysts with various Ba loadings. Without a catalyst, NO_x concentration increased to 200 ppm immediately at the same time as NO/O_2 gas was introduced to the reactor. TiO_2 showed activity for NO_x storage under UV-light irradiation, and the dead time for the NO_x breakthrough was 530 s. Loading of Ba drastically extended the dead time for NO_x breakthrough for all the Ba loadings investigated as compared to TiO_2. Fig. 1B shows the dead time in Fig. 1A as a function of Ba loading. The dead time increased with increasing the Ba loading up to 500 μmol g^{-1}, and deceased over 500 μmol g^{-1}. The dead time in 500 μmol g^{-1} Ba/TiO_2 was 1020 s, which was longer than the period during the cold start condition (800 s) reported by ICCT.[11] After the reaction after 12 h, the rates of NO_x storage were saturated, and the total amounts of stored NO_x for 12 h of 500 μmol g^{-1} Ba/TiO_2 and TiO_2 were 560 and 389 μmol g^{-1}, respectively. The modification of TiO_2 with Ba oxides species improved both the dead time and the total adsorption amount of NO_x.

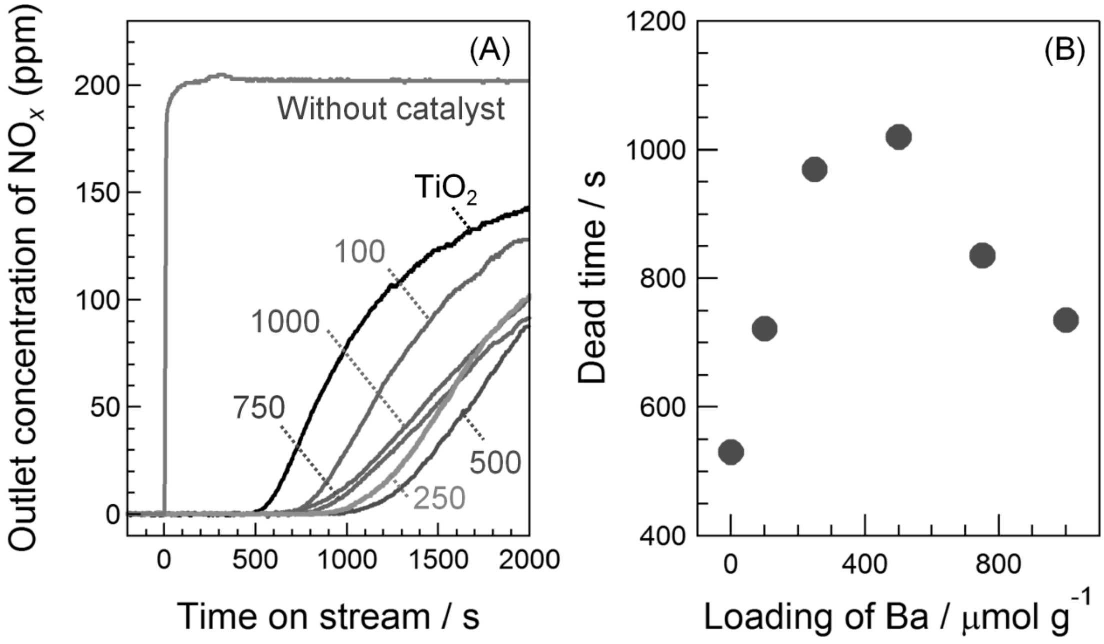

Figure 1. (A) Time course of the photo-assisted NO_x storage over Ba/TiO_2 catalysts. Pretreatment temperature: 773 K, NO: 200 ppm, O_2: 2%, He: balance. The numbers represent Ba loadings (μmol g^{-1}). (B) Effect of Ba loading on the dead time for the NO_x breakthrough.

In the XRD patterns of TiO_2 and as-synthesized Ba/TiO_2 with various Ba loading showed diffraction peaks of anatase TiO_2 (Fig. 2). Diffraction peaks of cubic $Ba(NO_3)_2$ appeared in the as-synthesized Ba/TiO_2 catalysts over 250 μmol g^{-1} of Ba loading, which indicates that the Ba species are loaded on TiO_2 as a nitrate form after the impregnation. Table 1 represents the crystalline size of TiO_2 and S_{BET} of the catalysts with various Ba loading. In the as-synthesized catalysts, S_{BET} decreased with increasing the Ba loading although the crystalline size of TiO_2 did not change after the Ba loading. The decrease of the surface area is possibly due to a plugging of pores derived from gaps of TiO_2 particles.[40] Without Ba loading (bare TiO_2), the pretreatment at 773 K and the following reaction drastically decreased S_{BET} from 292 to 185 m^2 g^{-1} and increased the crystalline sizes of TiO_2 from 7.7 to 10.9 nm, which was due to sintering of TiO_2 particles after the pretreatment at 773 K. The crystalline sizes of TiO_2 (8.5–9.3 nm) in Ba/TiO_2 after the reaction were smaller than that of TiO_2 after the reaction (10.9 nm). Thus, the Ba loading clearly suppressed the sintering of TiO_2 particles. To investigate of the effect of S_{BET}, the dead time was plotted as a function of S_{BET} as shown in Fig. 3. The dead time increased with increasing S_{BET} in the case of TiO_2 after the pretreatment at 673, 773, and 873 K (blue triangles). In the several photocatalytic reactions,[21, 41] the activity strongly depends on the surface area of the photocatalyst especially when the adsorption step of substrates is relatively slow. In this reaction, the strong positive correlation between the dead time and S_{BET} was clearly observed, which suggests that the increase of S_{BET} would be effective to improve the activity. On the other hand, Ba/TiO_2 photocatalyst (red circles) showed the significantly higher activity than those of TiO_2 with similar S_{BET}. The activity improvement by the Ba loading cannot be explained by the surface area (i.e., sintering of TiO_2 particles). In addition, there was no correlation between the dead time and S_{BET} in Ba/TiO_2 with various Ba loading, which suggests that the dead time is dependent on the amount and state of Ba species. The total amount of stored NO_x for 12 h of 500 μmol g^{-1} Ba/TiO_2 was 1.4 times higher than that of TiO_2 although S_{BET} was almost the same as shown in Table 1. The results suggested that the Ba oxide species generated after the pretreatment at 773 K functioned as an effective NO_x storage material.

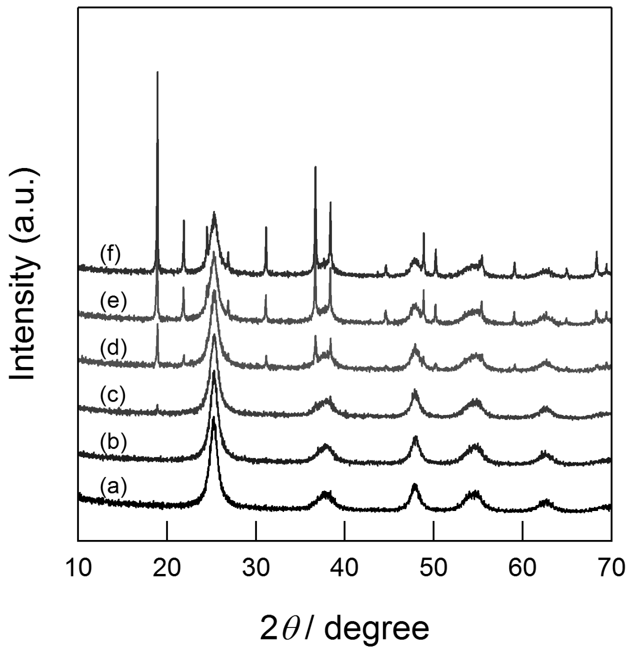

Figure 2. XRD patterns of the as-synthesized Ba/TiO_2 catalysts with various Ba loading. (a) 0, (b) 100, (c) 250, (d) 500, (e) 750, and (f) 1000 μmol g^{-1}.

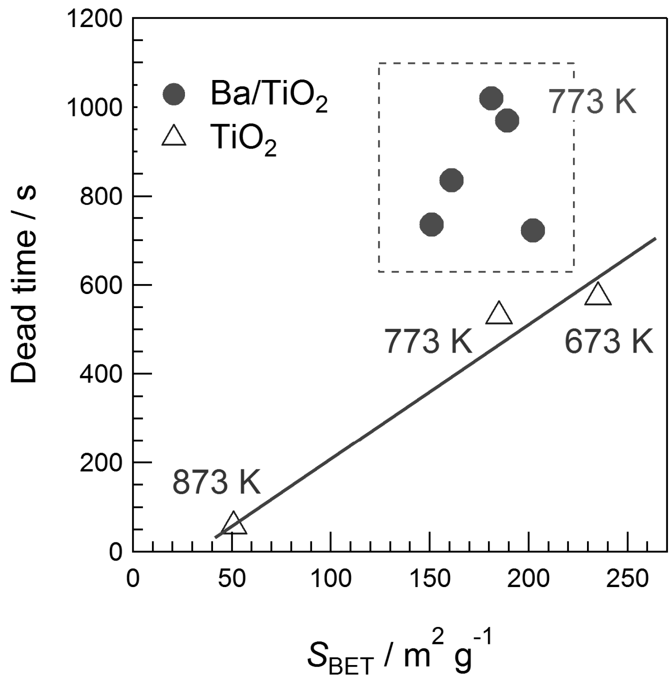

Figure 3. Correlation between S_{BET} and the dead time for the NO_x breakthrough. Pretreatment temperatures were shown next to the symbols.

Table 1. Crystalline size of TiO_2 and BET specific surface area before and after the pretreatment and reaction.

Ba loading / μmol g^{-1}	d [a] / nm		S_{BET} [b] / m^2 g^{-1}	
	As-syn.[c]	AR[d]	As-syn.	AR
0	7.7	10.9	292	185
100	7.6	9.3	272	202
250	7.6	9.2	254	189
500	7.5	8.8	228	181
750	7.7	8.5	204	161
1000	7.7	8.5	181	151

[a] Crystalline size of TiO_2. [b] Specific surface area estimated from the BET method. [c] As-synthesized. [d] After the pretreatment at 773 K and the following NO_x storage reaction.

Correlation between the activity and TPD peak areas

TPD experiments were carried out using the as-synthesized Ba/TiO_2 catalysts to identify the active Ba precursors (Fig. 4A). Three desorption peaks were observed around 710, 800, and 850 K (referred to as peaks 1, 2, and 3, respectively). The peak 1 was assigned to the decomposition of $Ba(NO_3)_2$ in contact with a TiO_2 surface, and the peaks 2 and 3 were due to the decomposition of bulk $Ba(NO_3)_2$.[29] Two desorption peaks were observed in the TPD experiment using a $Ba(NO_3)_2$ reference powder at 840 and 910 K, and the desorption temperatures were higher than those of Ba/TiO_2. The low desorption temperatures in the Ba-modified catalysts were due to the interaction between TiO_2 and Ba species.[38] The peaks 2 and 3 were possibly due to the decomposition of the surface and inner part of bulk $Ba(NO_3)_2$.[29] The areas of peaks 1, 2, and 3, which were estimated from a peak fitting using three Gaussians, were plotted against the Ba loading (Fig. 4B). The area of peak 1 increased with the Ba loading up to 500 μmol g^{-1}, and was saturated over 500 μmol g^{-1}. On the other hands, the areas of peaks 2 and 3 showed the same tendency; the areas of two peaks were low below 250 μmol g^{-1}, and the further increase of the Ba loading rapidly increased the areas of the two peaks. The same tendency supports the above assignment that peaks 2 and 3 were derived from the bulk $Ba(NO_3)_2$. As shown above, there are at least two $Ba(NO_3)_2$ species in the as-synthesized Ba/TiO_2; one is the surface $Ba(NO_3)_2$ in contact with a TiO_2 surface, and the other one is the bulk $Ba(NO_3)_2$ without a contact with a TiO_2 surface.

The effect of the Ba loading on the activity was explained by the amount of two $Ba(NO_3)_2$ species estimated from the TPD spectra. The dead time in Fig. 1 increased with increasing the area of peak 1 derived from the surface $Ba(NO_3)_2$. The correspondence between activity and the amount of surface $Ba(NO_3)_2$ indicated that the surface $Ba(NO_3)_2$ on a TiO_2 is a precursor of active Ba oxide species for the NO_x storage. On the other hand, over 500 μmol g^{-1}, the activity decreased in spite of the fact that the amount of the surface $Ba(NO_3)_2$ (i.e., area of peak 1) did not change. The bulk $Ba(NO_3)_2$, which was inactive for the reaction,[29] was generated, and the amount increased with the Ba loading. The increase of the Ba loading from 500 to 1000 μmol g^{-1} decreased the TiO_2 content in the catalyst by 13 wt% because the 500 and 1000 μmol g^{-1} corresponded to 13 and 26 wt%, respectively. The decrease of TiO_2 should decrease the activity because TiO_2 works as an oxidation site in the reaction. Thus, amounts of the surface $Ba(NO_3)_2$ and the inactive bulk $Ba(NO_3)_2$ affected the activity, which resulted in the non-correlation between S_{BET} and the activity in Ba/TiO_2 in Fig. 3.

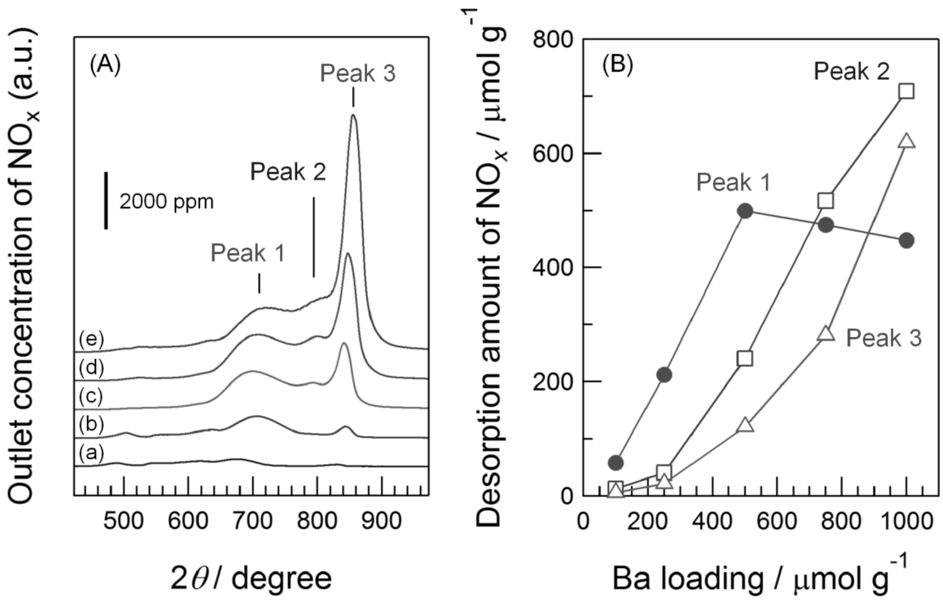

Figure 4. (A) TPD profiles of as-synthesized Ba/TiO_2 catalyst with various Ba loadings of (a) 100, (b) 250, (c) 500, (d) 750, and (e) 1000 μmol g^{-1}. (B) Desorption amounts of NO_x estimated from the peaks 1, 2, and 3 as a function of Ba loading.

DRIFT investigation

DRIFT spectra were recorded at various exposure times of NO/O_2 gas in the dark. In the case of TiO_2 (Fig. 5A), the peaks at 1622, 1480, 1322, and 1194 cm^{-1} increased with the exposure time of NO/O_2 gas. The peaks at 1480, 1322, and 1194 cm^{-1} were assignable to NO_2^- species, and the peak at 1622 cm^{-1} to NO_3^- species.[42] The co-adsorption of NO and O_2 produced NO_2^- and NO_3^- species via adsorption and oxidation, which was in line with previous reports using several transition metals including TiO_2.[42-45] After the irradiation, the peak intensity at 1194 cm^{-1} monotonically decreased with the irradiation time, which indicates that the NO_2^- species are consumed under irradiation. On the other hand, the intensities of new peaks at 1603, 1582, 1496, 1302, and 1249 cm^{-1} increase and are saturated after 20 min of irradiation, which is due to the generation of NO_3^- species with bridging (1603, 1249 cm^{-1}), chelating (1582, 1302 cm^{-1}), and monodentate (1496 cm^{-1}) forms.[21, 42-43] Thus, the NO_2^- species are an intermediate in NO_x storage, and are oxidized into the NO_3^- species under irradiation (eqs. 1 and 2).

$$NO \xrightarrow{O_2,\,dark} NO_2^-,\, NO_3^- \tag{1}$$

$$NO_2^- \xrightarrow{O_2,\,h\nu} NO_3^- \tag{2}$$

DRIFT spectra in 500 μmol g^{-1} Ba/TiO_2 were shown in Fig. 5B. In the dark, peaks at 1620, 1477, 1379, and 1210 appeared after 30 min of an NO/O_2 gas flow, and attribute to NO_2^- and NO_3^- species adsorbed on Ti sites because the peaks were observed in the case of TiO_2. Other peaks was also observed at 1379 cm^{-1} and around 1200 cm^{-1} (shoulder peaks) in Ba/TiO_2, which is possibly due to the NO_2^- species based on the wavenumber.[42] Although a small difference was observed in the DRIFT spectra between TiO_2 and Ba/TiO_2 in the dark, the difference was not a direct evidence of the improvement of the activity by Ba loading under irradiation because the activity of NO_x storage was quite low (no dead time) in the dark over Ba/TiO_2.[29] The DRIFT spectra of Ba/TiO_2 after irradiation in NO/O_2 gas were similar to that in the case of TiO_2; adsorption peaks at 1601, 1580, 1502, 1295, and 1254 cm^{-1} increase with increasing the irradiation time for 3 h. The previous reports using BaO/Al_2O_3 catalyst showed that NO_2 adsorbed on a BaO surface as ionic and bidentate NO_3^- species and the adsorbed NO_3^- show the IR peaks at 1550 cm^{-1} (bidentate), and 1320 and 1410 cm^{-1}

(ionic).[34, 45] In our DRIFT investigations, the bands were not observed under irradiation. The results clearly indicates that the bulk BaO is not generated after the pretreatment. Absence of bulk BaO species suggests that Ba species are strongly interacted with TiO_2 as reported previously.[38]

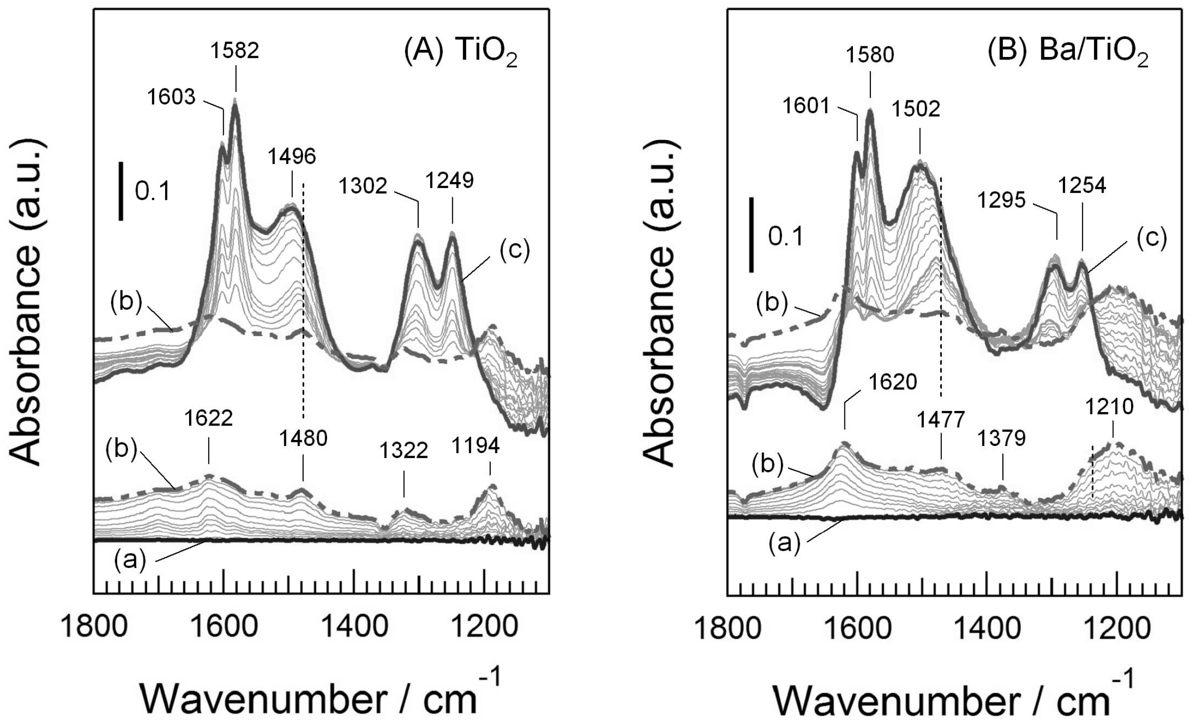

Figure 5. DRIFT spectra of (A) TiO_2 and (B) 500 μmol g^{-1} Ba/TiO_2. (a): after the pretreatment at 773 K, (b): after addition of NO/O_2 gas for 30 min in the dark, (c): after irradiation for 3 h in NO/O_2 gas.

XRD pattern and TEM image

Fig. 6 shows the XRD patterns of TiO_2 and 500 μmol g^{-1} Ba/TiO_2. In all the catalysts, the diffraction peaks of anatase TiO_2 were observed. In as-synthesized Ba/TiO_2, the diffraction patterns of $Ba(NO_3)_2$ was observed, and the pretreatment at 773 K deceaseed the peak intensities. The decrease of the peak intensities is due to the decomposition of $Ba(NO_3)_2$ on a TiO_2 surface based on the TPD results. No other peak was observed after the pretreatment at 773 K, which suggests the Ba oxide species had an amorphous structure. After the NO_x storage, the peaks derived from $Ba(NO_3)_2$

did not change compared to Ba/TiO_2 after the pretreatment. From TEM images (Fig. 7), the particle size of TiO_2 in the as-synthesized Ba/TiO_2 was approximately 7–9 nm, which accorded to the crystalline size estimated from XRD (Table 1). The particle size hardly changed after the pretreatment at 773 K, and the following reaction.

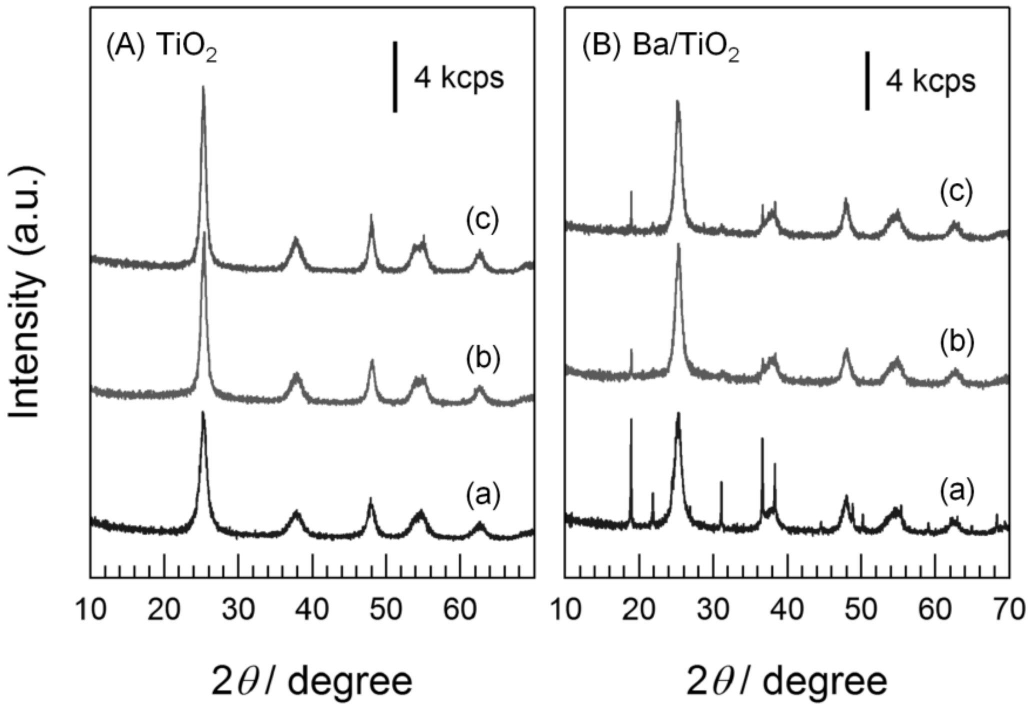

Figure 6. XRD patterns of (A) TiO_2 and (B) 500 μmol g^{-1} Ba/TiO_2. (a): as-synthesized, (b): after the pretreatment at 773 K, (c): after the reaction.

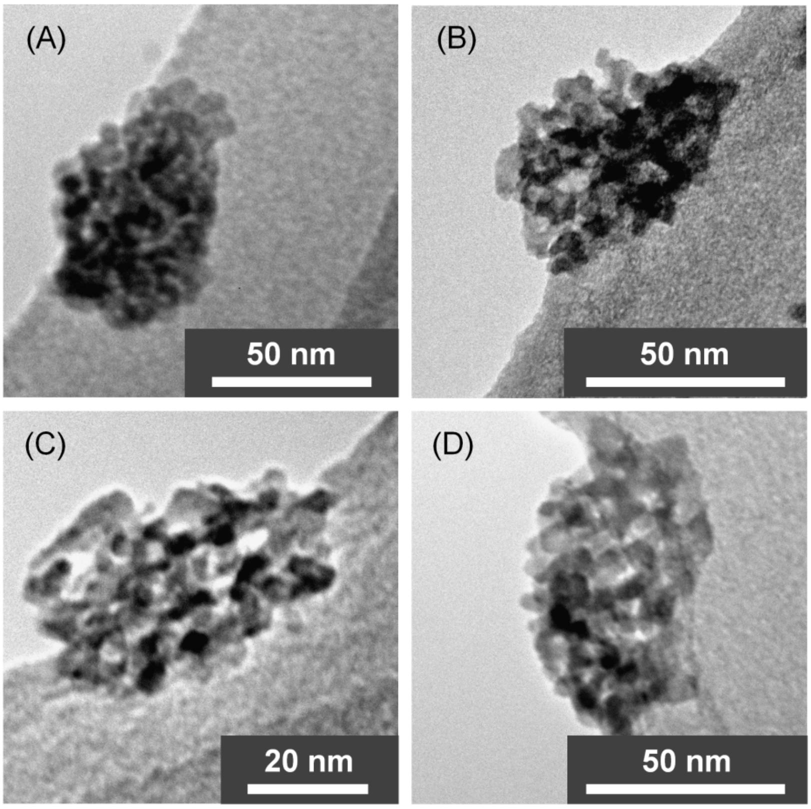

Figure 7. TEM images of (A) TiO_2, (B) as-synthesized Ba/TiO_2, (C) Ba/TiO_2 after the pretreatment, and (D) Ba/TiO_2 after the reaction. Ba loading: 500 μmol g^{-1}.

XPS measurement

Fig. 8A shows Ba $3d_{5/2}$ XPS of the Ba-modified catalysts. The peak positon of Ba $3d_{5/2}$ XPS of the as-synthesized Ba/TiO_2 was 779.9 eV. The peak positions in Ba/TiO_2 after the pretreatment and the following reaction were 780.2 and 780.1 eV, respectively, and peak shift was hardly observed. The positons in the Ba-modified catalysts were different from that in the $BaTiO_3$ reference sample (778.8 eV). In all the Ba-modified catalysts, the peak positions of Ti $2p_{3/2}$ were 458.4–458.5 eV (Fig. 8B), which were equal to that in TiO_2 (458.4 eV). In the case of $BaTiO_3$, the peak position was 458.1 eV and was higher by 0.3–0.4 eV compared to the Ba-modified catalysts. The results indicate that the $BaTiO_3$ phase do not generated both after the pretreatment and the following reaction. The Ba/Ti surface atomic ratio was calculated from XPS. The pretreatment drastically increased the Ba/Ti ratio from 0.03 to 0.19, and decreased to 0.12 after the reaction. The increase in the Ba/Ti ratio clearly evidenced the structural change of Ba oxide species after the pretreatment, and can be explained by a 2D layer structure of Ba oxide species. The 2D structure of Ba species accorded with a model proposed by Ozensoy et al. using a substrate,[46] and suggested the above-mentioned strong interaction between Ba oxide species and TiO_2.

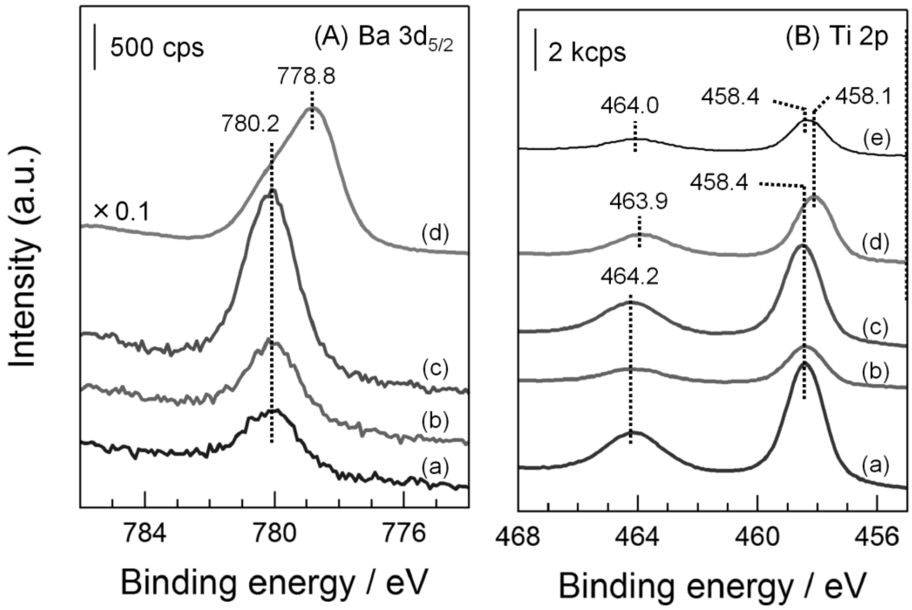

Figure 8. XPS of (A) Ba $3d_{5/2}$ and (B) Ti 2p. (a): as-synthesized, (b): after the pretreatment at 773 K, (c): after the reaction, (d): $BaTiO_3$, (e): TiO_2.

Active Ba species in photo-assisted NO_x storage

NO_x storage model is shown in Scheme 1. $Ba(NO_3)_2$ is loaded on a TiO_2 surface after impregnation. The O_2/He pretreatment at 773 K decomposes the surface $Ba(NO_3)_2$ to active Ba oxide species with releasing the NO_x. The active Ba oxide species has an amorphous and 2D layer structure based on the XRD and XPS analysis. The DRIFT revealed that the NO_3^- species were adsorbed on Ti sites after NO_x storage over Ba/TiO_2, which suggests that the generated NO_x species do not adsorb to Ba atoms directly. In the previous report, barium orthotitanate (Ba_2TiO_4) was observed during the reaction between BaO/$BaCO_3$ and TiO_2 (110) rutile single crystal by XRD technique, and proposed that Ba_2TiO_4 was an intermediate phase for $BaTiO_3$ formation.[47] In addition, generation of perovskite-type Ba–Ti surface species (e.g., $BaTiO_3$, and Ba_2TiO_4) was reported after Ba deposition over TiO_2/Pt(111) and following oxidation with O_2 at 573–973 K by XPS, and their LEED images showed that the Ba–Ti surface species has an amorphous structure.[46] In our previous reports, $BaTiO_3$

was observed by increasing the pretreatment temperature from 773 to 873 K and at the temperature, the activity of NO_x storage decreased because S_{BET} decreased at the same time of the generation.[29] Accordingly, Ba–Ti surface species can be generated in the O_2/He pretreatment at 773 K with an amorphous structure in our photocatalytic system. Besides, adsorption of NO_x on perovskite compounds including $BaTiO_3$ was investigated, and these perovskites showed a large NO_x storage capacity in spite of low S_{BET}, (i.e., surface density of NO_x^- species was high on $BaTiO_3$).[48] Based on the relationship between the NO_x storage capacity and S_{BET}, they proposed that the perovskite structure was partially decomposed during NO_2 adsorption process and releasing the stored NO_x lead to the recovery of the perovskite structure, which resulted in the high NO_x storage capacity. In our experiments, 500 μmol g^{-1} Ba/TiO_2 showed 1.4 times higher NO_x storage capacity than that of TiO_2 despite similar S_{BET} (Table 1). Thus, the amorphous Ba–Ti mixed oxides are formed on a TiO_2 surface after the pretreatment and stored NO_x^- more densely than TiO_2. We concluded that the generation of Ba–Ti mixed oxides leads to the high storage capacity of NO_x under UV-light irradiation.

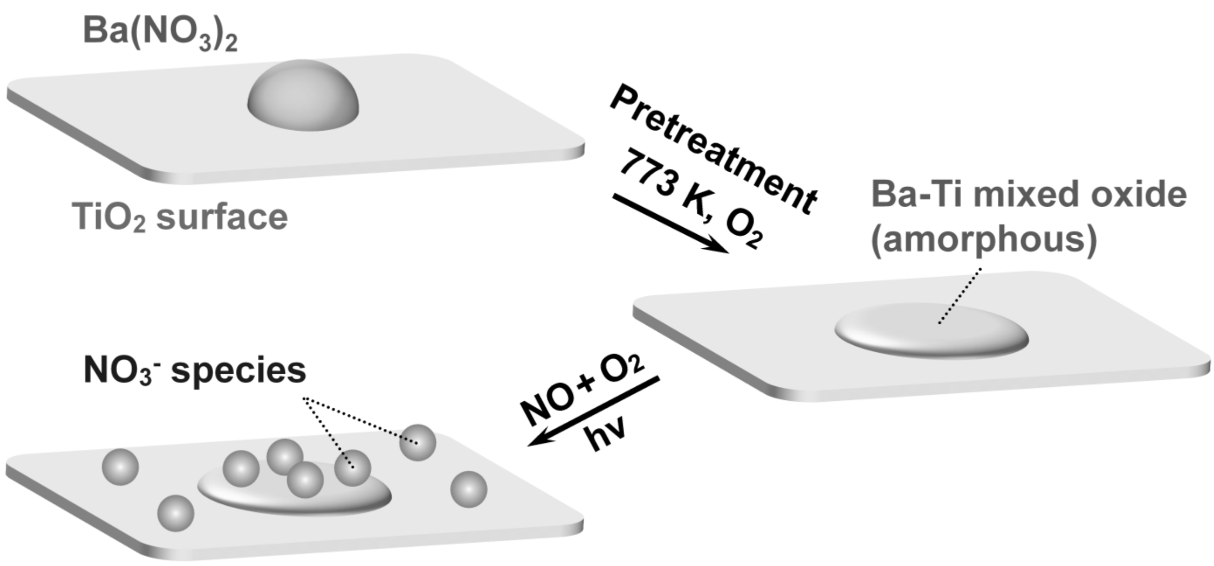

Scheme 1. Surface model of Ba oxide species.

Conclusions

We investigated the effect of Ba loading and active Ba oxide species in photo-assisted NO_x storage over Ba-modified TiO_2 photocatalyst under UV-light irradiation. The Ba loading affected the amounts of the surface and bulk $Ba(NO_3)_2$ species in the as-synthesized catalysts with various Ba loadings, and the amounts predominated the activity. The surface $Ba(NO_3)_2$ was decomposed after the pretreatment at 773 K into an active Ba–Ti mixed oxides with an amorphous structure. It was firstly proposed that the surface amorphous Ba–Ti mixed oxides functioned as an effective NO_x storage material.

References

[1] S. Roy, A. Baiker, *Chem. Rev.* **2009**, *109*, 4054-4091.

[2] G. Centi, G. E. Arena, S. Perathoner, *J. Catal.* **2003**, *216*, 443-454.

[3] J. Kašpar, P. Fornasiero, N. Hickey, *Catal. Today* **2003**, *77*, 419-449.

[4] G. Liu, P.-X. Gao, *Catal. Sci. Technol.* **2011**, *1*, 552-568.

[5] N. Takahashi, H. Shinjoh, T. Iijima, T. Suzuki, K. Yamazaki, K. Yokota, H. Suzuki, N. Miyoshi, S.-i. Matsumoto, T. Tanizawa, T. Tanaka, S.-s. Tateishi, K. Kasahara, *Catal. Today* **1996**, *27*, 63-69.

[6] G. Busca, L. Lietti, G. Ramis, F. Berti, *Appl. Catal. B* **1998**, *18*, 1-36.

[7] V. I. Pârvulescu, P. Grange, B. Delmon, *Catal. Today* **1998**, *46*, 233-316.

[8] P. Forzatti, *Appl. Catal. A* **2001**, *222*, 221-236.

[9] J. Li, H. Chang, L. Ma, J. Hao, R. T. Yang, *Catal. Today* **2011**, *175*, 147-156.

[10] T. Johnson, *Platinum Met. Rev.* **2008**, *52*, 23-37.

[11] L. Dana, K. Fanta, *Urban off-cycle NO_x emissions from Euro IV/V trucks and buses* **2012**, http://www.theicct.org/urban-cycle-nox-emissions-euro-ivv-trucks-and-buses.

[12] S. i. Matsumoto, Y. Ikeda, H. Suzuki, M. Ogai, N. Miyoshi, *Appl. Catal. B* **2000**, *25*, 115-124.

[13] W. S. Epling, L. E. Campbell, A. Yezerets, N. W. Currier, J. E. Parks, *Cat. Rev. - Sci. Eng.* **2004**, *46*, 163-245.

[14] N. Takahashi, K. Yamazaki, H. Sobukawa, H. Shinjoh, *Appl. Catal. B* **2007**, *70*, 198-204.

[15] Y. Ohko, Y. Nakamura, N. Negishi, S. Matsuzawa, K. Takeuchi, *J. Photochem. Photobiol. A* **2009**, *205*, 28-33.

[16] S. Yin, H. Yamaki, M. Komatsu, Q. Zhang, J. Wang, Q. Tang, F. Saito, T. Sato, *Solid State Sciences* **2005**, *7*, 1479-1485.

[17] Y. Ishibai, J. Sato, S. Akita, T. Nishikawa, S. Miyagishi, *J. Photochem. Photobiol. A* **2007**, *188*, 106-111.

[18] K. Hashimoto, K. Sumida, S. Kitano, K. Yamamoto, N. Kondo, Y. Kera, H. Kominami, *Catal. Today* **2009**, *144*, 37-41.

[19] B. N. Shelimov, N. N. Tolkachev, O. P. Tkachenko, G. N. Baeva, K. V. Klementiev, A. Y. Stakheev, V. B. Kazansky, *J. Photochem. Photobiol. A* **2008**, *195*, 81-88.

[20] A. M. Soylu, M. Polat, D. A. Erdogan, Z. Say, C. Yıldırım, Ö. Birer, E. Ozensoy, *Appl. Surf. Sci.* **2014**, *318*, 142-149.

[21] K. Hashimoto, K. Wasada, N. Toukai, H. Kominami, Y. Kera, *J. Photochem. Photobiol., A* **2000**, *136*, 103-109.

[22] J. Lasek, Y.-H. Yu, J. C. S. Wu, *J. Photochem. Photobiol. C: Photochem. Rev.* **2013**, *14*, 29-52.

[23] R. Dillert, A. Engel, Gro, P. Lindner, D. W. Bahnemann, *PCCP* **2013**, *15*, 20876-20886.

[24] A. Folli, S. B. Campbell, J. A. Anderson, D. E. Macphee, *J. Photochem. Photobiol. A* **2011**, *220*, 85-93.

[25] Q. Wu, R. van de Krol, *J. Am. Chem. Soc.* **2012**, *134*, 9369-9375.

[26] J. Zhang, T. Ayusawa, M. Minagawa, K. Kinugawa, H. Yamashita, M. Matsuoka, M. Anpo, *J. Catal.* **2001**, *198*, 1-8.

[27] J. C. S. Wu, Y.-T. Cheng, *J. Catal.* **2006**, *237*, 393-404.

[28] J. S. Dalton, P. A. Janes, N. G. Jones, J. A. Nicholson, K. R. Hallam, G. C. Allen, *Environ. Pollut.* **2002**, *120*, 415-422.

[29] A. Yamamoto, Y. Mizuno, K. Teramura, S. Hosokawa, T. Tanaka, *ACS Catalysis* **2015**, *in press*.

[30] S. Hodjati, P. Bernhardt, C. Petit, V. Pitchon, A. Kiennemann, *Appl. Catal. B* **1998**, *19*, 209-219.

[31] S. Hodjati, P. Bernhardt, C. Petit, V. Pitchon, A. Kiennemann, *Appl. Catal. B* **1998**, *19*, 221-232.

[32] D. H. Kim, J. H. Kwak, J. Szanyi, S. D. Burton, C. H. F. Peden, *Appl. Catal. B* **2007**, *72*, 233-239.

[33] D. Uy, A. O'Neill, J. Li, W. H. Watkins, *Catal. Lett.* **2004**, *95*, 191-201.

[34] S. M. Andonova, G. k. S. Şentürk, E. Ozensoy, *J. Phys. Chem. C* **2010**, *114*, 17003-17016.

[35] T. Tanaka, K. Amano, K. Dohmae, N. Takahashi, H. Shinjoh, *Appl. Catal. A* **2013**, *455*, 16-24.

[36] H. Imagawa, N. Takahashi, T. Tanaka, S. i. Matsunaga, H. Shinjoh, *Appl. Catal. B* **2009**, *92*, 23-29.

[37] I. S. Pieta, W. S. Epling, M. García-Diéguez, J. Y. Luo, M. A. Larrubia, M. C. Herrera, L. J. Alemany, *Catal. Today* **2011**, *175*, 55-64.

[38] S. M. Andonova, G. S. Şentürk, E. Kayhan, E. Ozensoy, *J. Phys. Chem. C* **2009**, *113*, 11014-11026.

[39] J. H. Scofield, *J. Electron. Spectrosc. Relat. Phenom.* **1976**, *8*, 129-137.

[40] A. Yamamoto, K. Teramura, S. Hosokawa, T. Tanaka, *Science and Technology of Advanced Materials* **2015**, *16*, 024901.

[41] S. Yamazoe, T. Okumura, T. Tanaka, *Catal. Today* **2007**, *120*, 220-225.

[42] K. I. Hadjiivanov, *Cat. Rev. - Sci. Eng.* **2000**, *42*, 71-144.

[43] G. Ramis, G. Busca, V. Lorenzelli, P. Forzatti, *Appl. Catal.* **1990**, *64*, 243-257.

[44] I. Nova, L. Castoldi, L. Lietti, E. Tronconi, P. Forzatti, F. Prinetto, G. Ghiotti, *J. Catal.* **2004**, *222*, 377-388.

[45] F. Prinetto, G. Ghiotti, I. Nova, L. Castoldi, L. Lietti, E. Tronconi, P. Forzatti, *PCCP* **2003**, *5*, 4428-4434.

[46] E. Emmez, E. I. Vovk, V. I. Bukhtiyarov, E. Ozensoy, *J. Phys. Chem. C* **2011**, *115*, 22438-22443.

[47] A. Lotnyk, S. Senz, D. Hesse, *Solid State Ionics* **2006**, *177*, 429-436.

[48] S. Hodjati, K. Vaezzadeh, C. Petit, V. Pitchon, A. Kiennemann, *Appl. Catal. B* **2000**, *26*, 5-16.

Summary

In this thesis, the author investigated the two types of photocatalytic de-NO_x reactions at low temperature over TiO_2-based photocatalysts; part I is concerned with photo-assisted selective catalytic reduction (photo-SCR), and part II deals with photo-assisted NO_x storage. In both of these photocatalytic reactions, NO was removed efficiently under UV and/or visible light irradiation. the author successfully improved the photocatalytic activities by surface modification of TiO_2 with organic and inorganic materials to put these photocatalytic systems into practical use. Besides, the nature of the high activity and the working mechanism were stated on the basis of the mechanistic and structural analyses using the various spectroscopic methods.

In Chapter 1, the author found the reaction temperature had a significant effect on the photo-SCR activity of a TiO_2 photocatalyst under irradiation. Optimization of the reaction temperature significantly increased the conversion up to 84% with selectivity to N_2 of 100% at a high GHSV of 100,000 h^{-1} (at 433 K). Kinetic analysis revealed that the rate-determining step of the photo-SCR was decomposition of surface NH_2NO intermediates in all the range of the reaction temperature investigated (353–593 K). The author concluded that the activity improvement was due to the acceleration of the rate determining step based on the kinetic analysis. The above result suggests the utilization of residual heat from engines is effective to obtain high activity.

In Chapter 2, the author established that modification of a TiO_2 photocatalyst with porphyrin dyes was effective for the development of visible-light-sensitive photocatalysts. Tetra(p-carboxyphenyl)porphyrin (TCPP) was the most effective photosensitizer among the five porphyrin derivatives investigated. NO conversion and N_2 selectivity of 79% and 100% respectively, were achieved at a GHSV of 50,000 h^{-1} under visible-light irradiation. UV–Vis and photoluminescence spectroscopies showed that the aggregation of TCPP drastically decreased the activity. Thus, suppression of the aggregation is one of the methods to improve the photo-SCR activity of the dye-sensitized TiO_2 photocatalysts.

In Chapter 3, the screening of dyes significantly enhanced the photocatalytic activity in the photo-SCR over the dye-sensitized TiO_2 photocatalysts under visible-light irradiation. Among the 15

dyes investigated, the maximum conversion was achieved using a Ru(2,2'-bipyridyl-4,4'-dicarboxylic acid)$_2$(NCS)$_2$ complex (N3-dye) for the modification of TiO_2 (NO conversion > 99%, N_2 selectivity > 99%). The reasonable reaction mechanism was proposed using several spectroscopic methods; surface nitrite (NO_2^-) intermediates was found to be responsible for the high selectivity to N_2. The conversion obtained was enough for practical use in mobile NO_x emission sources such as buses and trucks.

In Chapter 4, the effect of SO_2 gas was investigated on the activity in the photo-SCR over a TiO_2 photocatalyst in the presence of excess oxygen. Introduction of SO_2 (300ppm) decreased the activity at 373 K. Increment of the reaction temperature enhanced the tolerance to SO_2 gas, and a stable conversion of NO was obtained at 553 K. Based on the characterization of the catalysts after reactions, we concluded that the deposition of ammonium sulfate species decreased the specific surface area by plugging the pore structure of the catalysts and the decrease of the specific surface area resulted in the deactivation of the catalysts. Suppression of the generation of the ammonium sulfate species is a strategy to improve the tolerance to SO_2 in photo-SCR.

In Chapter 5, the photo-assisted NO_x storage was investigated over the Ba/TiO_2 photocatalysts under UV-light irradiation at a high GHSV of 50,000 h^{-1}. The author clearly demonstrated that the Ba loading enhanced the activity after the O_2 pretreatment at 673 K. The NO removal efficiency was kept > 99% during the 1020 s interval from the start of the reaction over the Ba/TiO_2 photocatalyst. The TPD and XRD measurement revealed that barium oxide species functioned as a NO_x storage material even at low temperatures, which resulted in the improvement of the performance of the photo-assisted NO_x storage.

In Chapter 6, the author investigated the structure of Ba species active for the NO_x storage under UV-light irradiation. The DRIFT investigation revealed that bulk BaO was not generated on a TiO_2 surface because nitrate (NO_3^-) species adsorbed on Ba sites were not observed in NO/O_2 gas under UV-light irradiation. Considering the DRIFT, XRD, XPS, and TEM results, the author proposed that the surface Ba–Ti mixed oxides with an amorphous structure was generated during the O_2 pretreatment and the formed Ba–Ti mixed oxides functioned as an effective NO_x storage material.

In summary, TiO_2-based photocatalysts exhibited high activity for the photo-SCR and photo-assisted NO_x storage under high GHSV conditions. The author clearly demonstrated the effectiveness of photocatalysts for the NO_x emission control at low temperature in the exhaust gas. The reasonable working mechanisms were proposed throughout the researches. These findings are believe to be contribute to the development of low-temperature de-NO_x systems for the exhaust gas in the future.

Appendix

Effect of a Crystalline Phase of TiO_2 Photocatalysts on the Photodeposition of Rh Metal Nanoparticles

Abstract

Effect of a crystalline phase of TiO_2 is investigated in the photodeposition processes of Rh metal nanoparticles on TiO_2 photocatalysts having anatase and rutile phase by means of in–situ time–resolved energy dispersive X–ray absorption fine structure spectroscopy (DXAFS), transmission electron microscopy (TEM), and X–ray photoelectron spectroscopy (XPS). The important factor was neither its crystallite size nor its specific surface area, and was the crystalline phase. In situ time–resolved DXAFS analysis clarified that the Rh metal nanoparticles with a uniform size appear on both anatase and rutile phases of TiO_2, whereas the appearance rate of Rh metal nanoparticles decreases with the photoirradiation time only on the rutile phase of TiO_2. The TEM observation and XPS depth analysis revealed that the bare surface of photodeposited Rh metal nanoparticles on the rutile is exposed, although that on the anatase is partially covered with TiO_2 due to strong metal–support interaction (SMSI) between Rh metal nanoparticle and $TiO_{2-\delta}$.

Introduction

It has widely been recognized that the photodeposition, which Bard et al. have reported in 1978,[1] is a very valuable method to recover of noble metals,[2-4] to remove metal cations from aqueous effluent,[5-7] and to prepare metal−supported catalysts[8-9] and metal–promoted photocatalysts.[10-13] Photoexcited electrons in a photocatalyst reduce metal cations that have more positive reduction potential than the conduction–band level of the photocatalyst. The simultaneously generated holes in the valence band are consumed with oxidation of a reactant such as alcohol, aldehyde, or carboxylic acid.[1, 5] In the several studies, it is found that the metal species were photodeposited on specific sites on a photocatalyst, for example, an edge or plane of a photocatalyst crystallite.[14-16] Interestingly, the morphology of the resulting metal nanoparticles greatly varies among the kinds of photocatalyst. These phenomena inspire us to study the systematic kinetics and mechanism for the formation of nanoparticles as well as the structure of resulting metal species. X–ray absorption fine structure (XAFS) spectroscopy is a powerful method to elucidate the formation process of the metal nanoparticles and reactivity of surface species.[17-22] Fernandez et al. have observed the photodeposition of Au nanoparticles by an in situ XAFS measurement, where the suspension composed of an Au precursor and TiO_2 was pumped out from the photochemical reactor to the XAFS measurement cell under photoirradiation.[23-24] We have also successfully observed the photodeposition process of Rh metal nanoparticles on TiO_2 using in situ time–resolved energy dispersive X–ray absorption fine structure spectroscopy (DXAFS), and proposed unique particle–formation mechanism that Rh metal nanoparticles with a uniform size constantly appear one after another on the surface of TiO_2.[25-26] We have also successfully observed the formation process of Rh and Au nanoparticles by means of time–resolved Quick XAFS experiments.[27-31]

Recently, we reported that photodeposited Rh and Pt metal nanoparticles on TiO_2 (JRC–TIO–8, anatase) were modified with $TiO_{2-\delta}$ which is well–known as a key species in the strong metal–support interaction (SMSI).[32-33] Generally, the SMSI can be observed when group VIII noble metals (e.g., Pt, Rh, Pd, and Ir) on reducible oxide supports (e.g., TiO_2 and Nb_2O_5) are treated with H_2 at high temperature and causes the modification of metal nanoparticles with reduced supports (e.g., $TiO_{2-\delta}$) generated by H_2 treatment. It is both interesting and incredible that the SMSI take places by photoirradiation at room temperature as well as by H_2 treatment at high temperature. Most probably, $TiO_{2-\delta}$ generated by the photoirradiation of TiO_2 cause the modification and the disorganized structure of Rh and Pt metal nanoparticles. Amount, type and property of $TiO_{2-\delta}$, therefore, may have an effect on the SMSI in the photodeposition process. Li et al. reported that the SMSI occurs by H_2 reduction at lower temperature on anatase TiO_2 than on rutile,[34] suggesting that the crystalline phase of TiO_2 photocatalysts affects the interaction of Rh metals and TiO_2. In this study, we investigated the photodeposition processes of Rh metal nanoparticles on TiO_2 photocatalysts having anatase and rutile phases, and their structure by means of in situ time–resolved DXAFS spectroscopy, XPS with sputtering, TEM observation.

Experimental

Materials

TiO_2 samples used in this study (JRC–TIO–1, 3, 6, 8, and 10) were kindly supplied from the Japan Catalysis Society. All the samples were calcined in air at 673 K for 3 h before use. Crystalline phase of each TiO_2 was determined by X–ray diffraction technique (XRD). The crystallite size was estimated from the use of the Scherrer's equation. The specific surface area of sample was determined using N_2 adsorption isotherm at 77 K. Crystalline phases, surface areas, and crystallite sizes of TiO_2 used in this study were listed in Table 1. In this paper, for simplicity, we denote the phase and the catalyst like **N**–**X** where **N** is the catalyst name JRC–TIO–**N**, and **X** is **A** or **R** meaning anatase or rutile, respectively; i.e., JRC–TIO–8 (anatase) to **8–A** and JRC–TIO–3 (rutile) to **3–R**.

Photodeposition

The photodeposition of Rh nanoparticles on TiO_2 was carried out in a closed batch system. As a typical photodeposition method, 500 mg of TiO_2 was suspended in 3.2 mL of methanol in a batch reactor made of Pyrex glass with a flat ceiling window for irradiation, followed by the addition of 0.8 mL of an aqueous solution of $RhCl_3$ (Wako Pure Chemical Industries, Ltd., 0.076 mmol of Rh). The suspension was irradiated with a 200 W Hg–Xe lamp equipped with fiber optics, a collective lens, and a mirror (San–Ei Electric Co., Ltd., UVF–204S type C) after N_2 bubbling for 10 min. Then the suspension was filtered, and the residual powder was washed with 100 mL of purified water and was placed in an oven at 353 K.

Time–resolved dispersive XAFS measurements

In situ time–resolved DXAFS measurements at the Rh–K edge (~23.2 keV) were performed at the BL28B2 beamline of the SPring–8. The DXAFS measurement system consists of a polychromator set to a Laue configuration with a Si (422) net plane and a position–sensitive detector (PSD) mounted on a θ–2θ diffractometer.[25, 27] The X–ray energy was calibrated by the spectrum of a Rh foil. The above–mentioned Pyrex reactor with the suspension was set at the X–ray focal spot. Light irradiation of the reactor was synchronized with exposure to X–rays. The exposure time of the PSD was 249 ms. Fifty shots were accumulated; 12.45 s per a spectrum. We programmed the collection of 500 snapshot spectra (124.5 s) in the dark and then 7000 snapshot spectra (1743 s) under photoirradiation consecutively. The measurement program was repeated four times to obtain the spectral change at 116.2 min under photoirradiation. Analysis of XAFS spectra was performed using the REX2000 program (version 2.5.9, Rigaku Corp.). The k^3–weighted EXAFS oscillation in the range of 2.78–10.7 Å was Fourier–transformed.

Characterization

XPS spectra were acquired using an ULVAC PHI 5500MT system. Samples mounted on indium foil were analyzed using Mg K$\alpha_{1,2}$ radiation (15 kV, 400 W) in a vacuum chamber ($<1\times10^{-8}$ Torr). The electron takeoff angle was set at 45°. Binding energies were referenced to C 1s peak of residual carbon at 284.6 eV. Sputtering was performed by a Xe ion beam (3.0 kV) with raster size 1.1 mm$\times$2.1 mm. TEM, STM, and EDX mapping images were obtained with a JEOL JEM–2100F transmission electron microscope operating at an accelerating voltage of 200 kV. TEM samples were prepared by depositing drops of a methanol suspension containing small amounts of the powders onto a carbon–coated copper grid (Okenshoji Co. Ltd.) .

Table 1. Properties of various TiO_2 photocatalysts.

	Crystalline phase	Crystallite size (nm)	Specific surface area (m^2 g^{-1})
JRC-TIO-8	Anatase	15.5	91.0
JRC-TIO-1	Anatase	18.7	75.1
JRC-TIO-10	Anatase	16.9	128
JRC-TIO-3	Rutile	21.9	47.1
JRC-TIO-6	Rutile	24.0	50.5

Results and Discussion

XANES spectra

Fig. 1 shows a series of Rh–K edge XANES spectra of the suspension comprised of a methanol aqueous solution of $RhCl_3$ and **3–R** under photoirradiation. The edge energy of XANES shifted to lower photon energy with the elongation of photoirradiation time. The XANES spectrum after 116 min of photoirradiation was almost identical to that of the Rh foil. This result indicates that Rh^{3+} ions are reduced to Rh^0 metals by photoirradiation. There is no change in the spectrum from $RhCl_3$ without TiO_2 or photoirradiation. The XANES spectral change corresponding to the reduction of Rh^{3+} ions to Rh^0 metals exhibits the isosbestic points, which indicates that Rh^{3+} ions are reduced to Rh^0 metals without any intermediates within the measurable time. All the Rh–K edge XANES spectra can be represented with the linear combination of the two XANES spectra; one is that of Rh^{3+} ions in the initial state and the other is that of Rh^0 metals in the final state. The least–squares fitting of each XANES spectrum with the linear combination allowed us to obtain the fractions of the Rh^0 metals and Rh^{3+} ions using **3–R** and **8–A** as shown in Fig. 2. The fraction of Rh^0 metals increased with the photoirradiation time in both the cases. In the case of **3–R**, the rate of an increase in Rh^0 metals decelerated with the photoirradiation time and the fraction of Rh^0 metals was saturated after 90 min. The deceleration of the increasing rate of Rh^0 metals means that the rate of reduction of

Rh^{3+} ions to Rh^0 metals was lowered with photoirradiation time. In the case of **8–A**, the Rh^0 metal fraction linearly increased with photoirradiation time and became constant at 75 min,[35] which means that the Rh^{3+} ions are reduced to Rh^0 metals at a constant rate. On the other hand, the behavior of reduction of Rh^{3+} ions to Rh^0 metals on **3–R** is different from that on **8–A**. When the other rutile phase of TiO_2 was used, the reduction rate of Rh^{3+} ions decreased with photoirradiation time as represented by the case of **3–R**, whereas, the reduction rate of Rh^{3+} ions on the anatase phase of TiO_2 were constant with photoirradiation time as represented by the case of **8–A** (Fig. 3). The behavior of reduction of Rh^{3+} ions to Rh^0 metals on the rutile is different from that on the anatase. These results strongly suggest that the crystalline phase of TiO_2 has an effect on the formation rate of Rh^0 metals for the photodeposition.

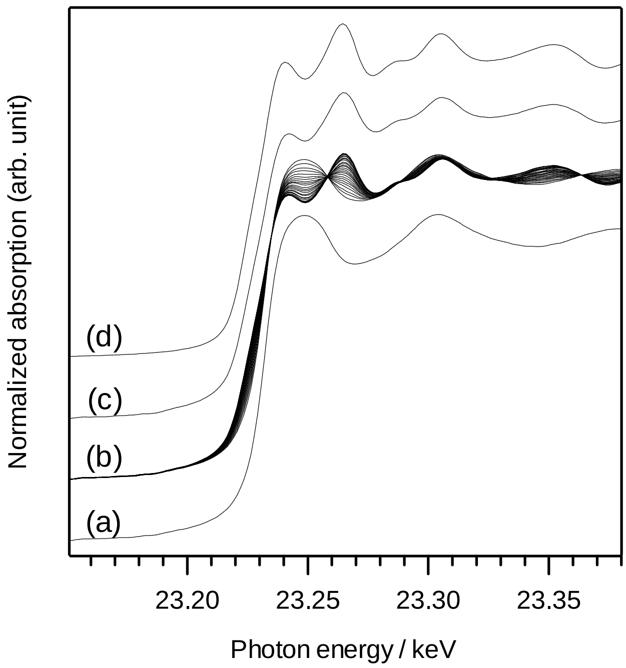

Figure 1. XANES spectra at the Rh–K edge of reference samples and the suspension consisting of a methanol aqueous solution of $RhCl_3$ and 3–R: (a) before irradiation, (b) under irradiation, (c) after irradiation for 116 min, and (d) Rh foil.

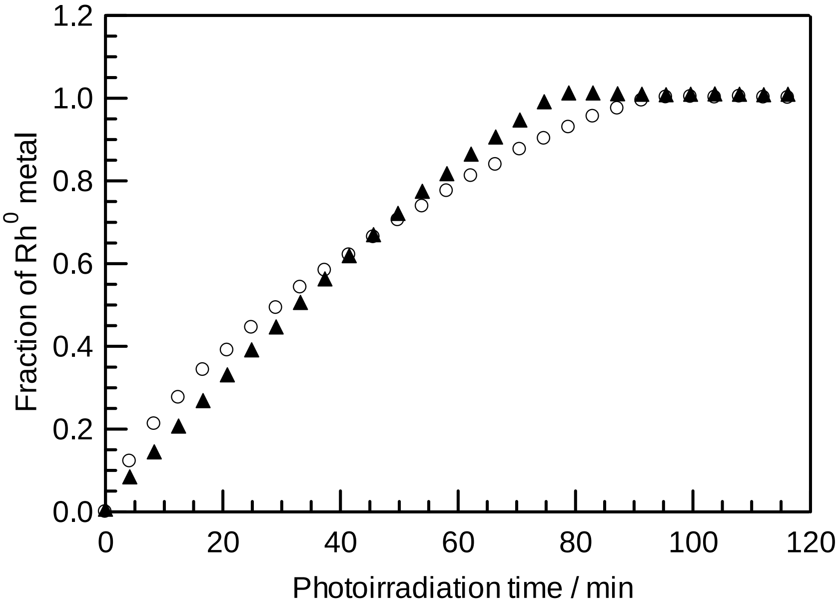

Figure 2. Dependence of the fraction of Rh^0 metals in the case of 3–R (○) and 8–A (▲).

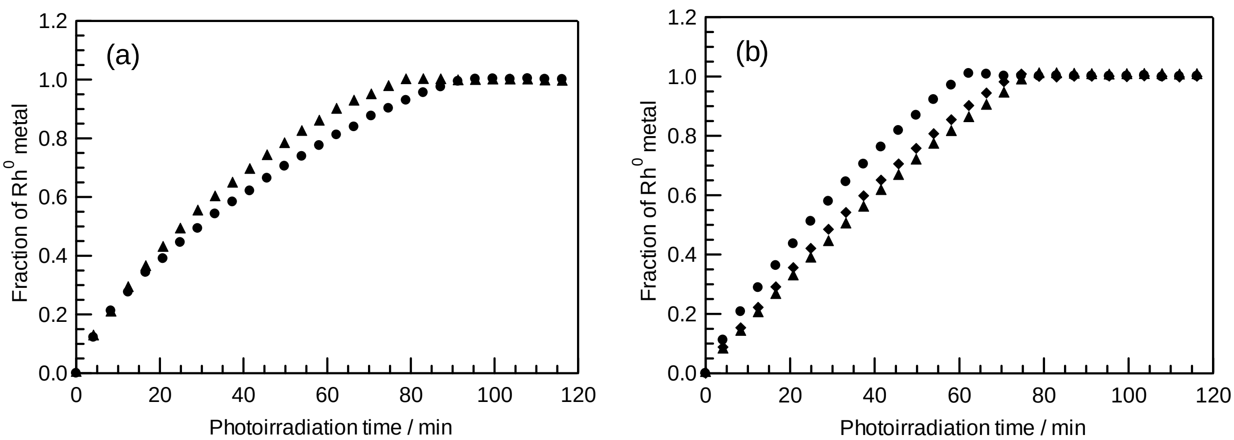

Figure 3. Dependence of the fraction of Rh^0 metal in the case of (a) TiO_2 (rutile), 3-R (●), 6-R (▲) and (b) TiO_2 (anatase), 1-A (●), 8-A (▲), 10-A (♦).

EXAFS spectra

Figs. 4 and 5 show a series of Rh–K edge EXAFS spectra of Rh species for photodeposition on **3–R** and Fourier transforms (FTs) of them. In Fig. 5, the peak located at 1.73 Å is assignable to the mixture of Rh–Cl and Rh–O scattering of $RhCl_3$ in solution and adsorbed on TiO_2.[26] The height of the peak at 1.73 Å decreased with increasing photoirradiation time, and an alternative peak appeared at 2.45 Å. The peak at 2.45 Å is assigned to the Rh–Rh scattering of Rh^0 metal nanoparticles generated by photoirradiation. The peak height at 2.45 Å rose with photoirradiation time and saturated at 90 min. The structural parameters (coordination number, interatomic distance, energy shift, and Debye-Waller factor) were obtained by a curve-fitting analysis. The structural parameters at the selected photoirradiation times are listed in Table 2. Fig. 6 demonstrates dependence of the C.N.(Rh–Rh) estimated from a curve fitting analysis of EXAFS spectra in the case of **3–R** and **8–A** on the photoirradiation time. In the case of **3–R**, the increase in the amount of change of C.N.(Rh–Rh) value was getting sluggish with the photoirradiation time and the value was saturated after 90 min of photoirradiation. In the case of **8–A**, the C.N.(Rh–Rh) increased proportionally to the photoirradiation time, and attained to 10 after 75 min of photoirradiation.[25] In both the cases, the behaviors of the C.N.(Rh–Rh) change perfectly corresponded to those of the fraction of Rh^0 metals estimated from analyses of XANES spectra.

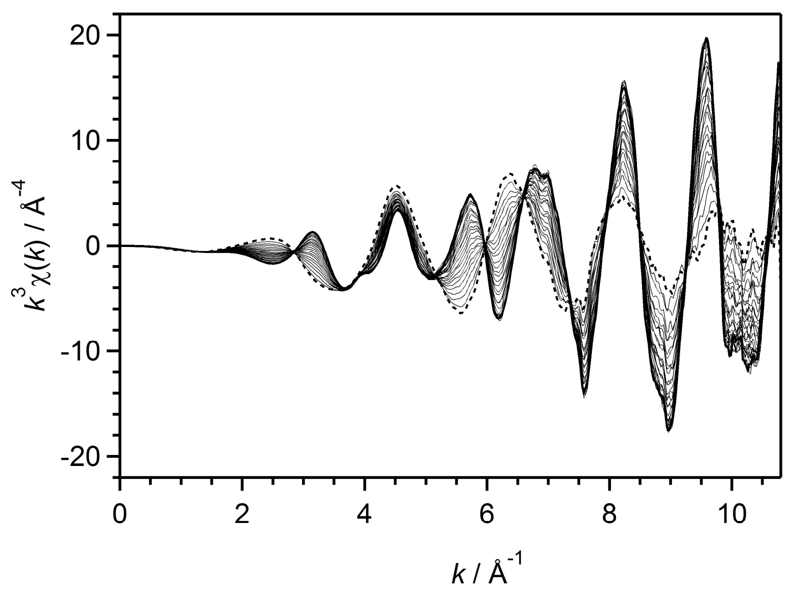

Figure 4. Series of k^3-weighted Rh-K edge EXAFS spectra of Rh species during the photodeposition on 3-R. Before irradiation: a dotted line, and after irradiation for 116 min: a black solid line.

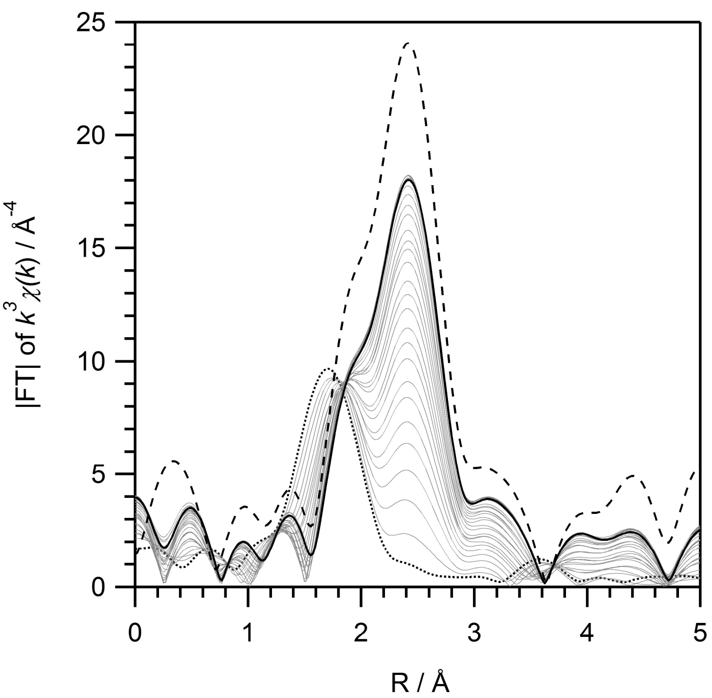

Figure 5 Series of the FT of k^3-weighted Rh-K edge EXAFS spectra of Rh species during the photodeposition in the case of 3–R. Before irradiation: a dotted line, after irradiation for 116 min: a black solid line, and Rh foil: a dashed line.

Table 2. Curve-Fitting Results of the Rh-Rh Scattering of the FT of EXAFS Spectra at Selected Photoirradiation Times[a]

TiO_2	photoirradiation time / min	C.N.(Rh-Rh)[b]	r/Å[c]	ΔE_0/eV[d]	σ/Å[e]	R[f]
3-R	29.1	4.5	2.69	0.3	0.061	0.47
3-R	58.1	7.1	2.68	0	0.060	0.18
3-R	87.2	9.3	2.69	0.5	0.062	0.05
3-R	116.2	9.6	2.69	0.4	0.063	0.07
8-A	29.1	4.5	2.70	0.8	0.062	0.19
8-A	58.1	8.4	2.69	1.3	0.062	0.03
8-A	87.2	10.6	2.69	0.7	0.062	0.02
8-A	116.2	10.4	2.69	0.5	0.061	0.02

[a]A Rh foil is used as a reference. The R fitting range is 2.07-3.66 Å. [b]C.N.(Rh-Rh): coordination number of Rh-Rh. [c]r: interatomic distance. [d] ΔE_0: energy shift [e] σ: Debye-Waller factor. [f] So-called R factor.

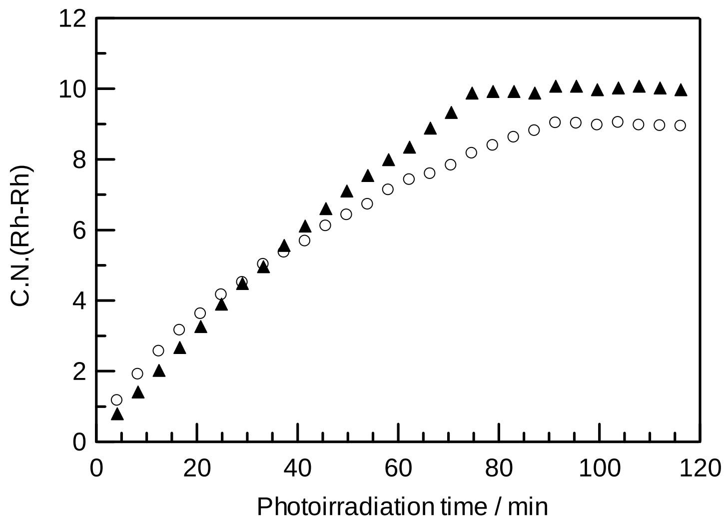

Figure 6. Photoirradiation time dependence of the C.N.(Rh–Rh) in the case of 3–R (○) and 8–A (▲).

Generation model of Rh nanoparticles

The C.N.(Rh–Rh) estimated from EXAFS analysis are the average for all the existing Rh^{3+} ions and Rh^0 atoms. Only Rh^0 atoms have Rh-Rh bonds and Rh^{3+} ions do not have. Thus, the C.N.(Rh–Rh) is given by

$$\text{C.N.(Rh–Rh)} = \text{C.N}_{Rh0} X_{Rh0} \quad (1)$$

where the C.N._{Rh0} is the coordination number of Rh^0 in the nanoparticles and the X_{Rh0} is the fraction of Rh^0 in the suspension. By using Eq. 1, the photoirradiation time dependence of the C.N._{Rh0} in the case of **3–R** and **8–A** is calculated from the Rh^0 metal fraction and the C.N.(Rh–Rh) shown in Fig. 2 and Fig. 6. As a result, the C.N._{Rh0} on **3–R** and **8–A** were constant with photoirradiation time (Fig. 7). This result indicates that Rh metal nanoparticles with a uniform size appear one after another on both kinds of TiO_2 during the photodeposition and the sizes never grow up. It is concluded that the difference in variation of C.N.(Rh–Rh) between **3–R** and **8–A** resulted from the difference in the appearance rate of Rh metal nanoparticles. In other words, the Rh metal nanoparticles with a uniform size appear both on the anatase and rutile, whereas the appearance rate decreases with the photoirradiation time only on the rutile.

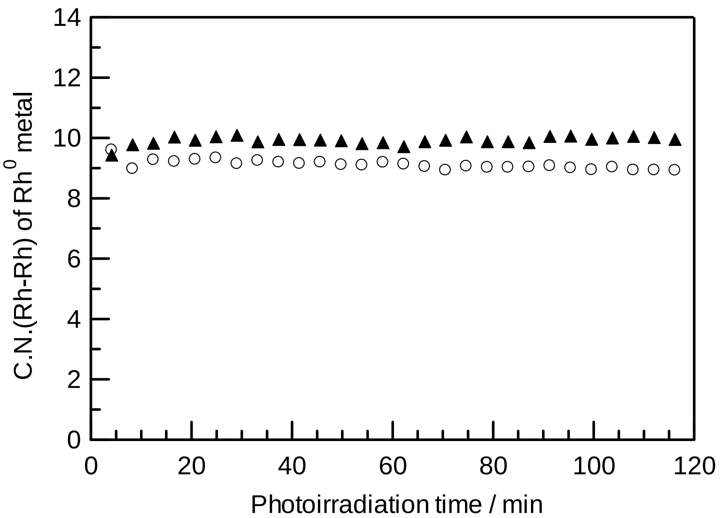

Figure 7. Photoirradiation time dependence of the C.N.(Rh–Rh) of Rh^0 metal in the case of 3–R (○) and 8–A (▲).

TEM, STEM and EDS analysis

Fig. 8a shows a TEM image of Rh–8A. Rh particles with a spherical shape were not observed. The particle boundaries of the Rh metal species are not identified in the TEM image although the existence of an Rh metal species is identified as green dots in the overlay of an EDS mapping image on a STEM image (Fig. 8b). Thus, we concluded that the Rh species on anatase phase of TiO_2 had a disordered structure, which would be due to the SMSI.[32] On the other hand, aggregated Rh species were observed on **3–R** as shown in Figs. 8c and 8d. The aggregated Rh species were composed of primary Rh nanoparticles. The particle size of the primary Rh nanoparticles was smaller than 5 nm, which corresponded to the diameter estimated from EXAFS spectra. In addition, the secondary Rh metal species were not decorated by TiO_2, suggesting the interaction between Rh metal and rutile phase of TiO_2 was lower than that between Rh metal and anatase phase of TiO_2.

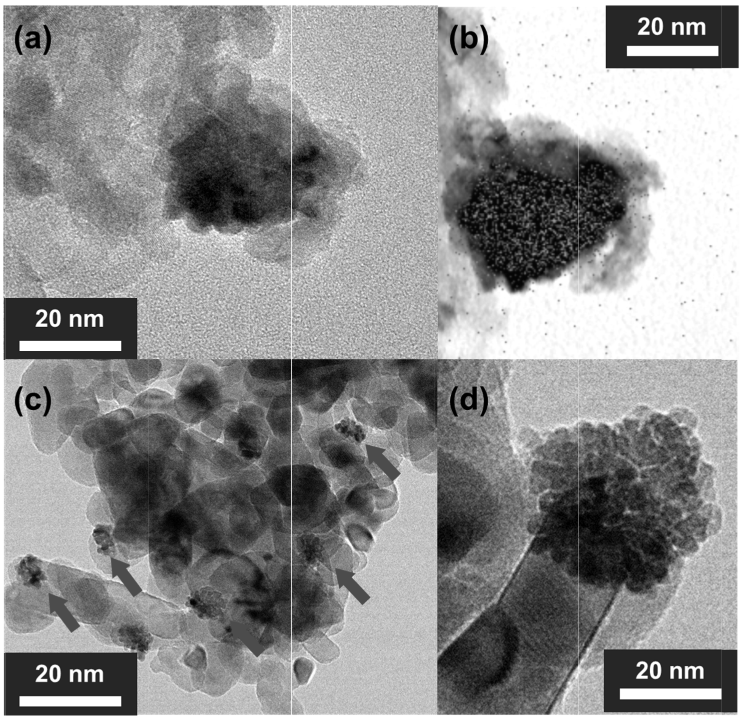

Figure 8. (a) TEM image and (b) overlay of EDS mapping image on STEM image of Rh–8–A, (c,d) TEM image of Rh–3–R.

XPS and sputtering by Xe ions

Fig. 9 shows the Rh 3d XPS of Rh metal nanoparticles photodeposited on **8–A** (**Rh–8–A**) and **3–R** (**Rh–3–R**). The peak of Rh $3d_{5/2}$ XPS of **Rh–8–A** appeared at 306.6 eV, which was lower energy than that of the Rh foil at 307.0 eV.[36] The lower energy position of the peak indicates the more electron–rich surface of metal nanoparticles. It was reported that the peak of Rh $3d_{5/2}$ XPS of Rh metal nanoparticles modified by $TiO_{2-\delta}$ was found to be located at lower energy than that of the Rh foil.[32, 37] **Rh–8–A** is reasonably assumed to be in the SMSI state. On the other hand, the peak of **Rh–3–R** appeared at 307.2 eV, which is approximately equal to the peak energy of Rh foil (307.0 eV).[36] The Rh metal nanoparticles of **Rh–3–R** would more weakly interact with TiO_2 than those of **Rh–8–A**. XPS measurements were carried out at a given sputtering time by Xe ion in these two samples. The composition ratio between Rh and Ti (Rh/Ti ratio) at a given sputtering time was evaluated from those peak areas divided by respective atomic sensitivity factors.[36] The variation in Rh/Ti ratio with sputtering time of **Rh–3–R** and **Rh–8–A** is shown in Fig. 10. The Rh/Ti ratio of **Rh–3–R** was constant with the sputtering time, whereas that of **Rh–8–A** increased with the sputtering time and approached to 1.3% after 14 min of sputtering. This change in Rh/Ti ratio indicates that the photodeposited Rh metal nanoparticles on **3–R** are not decorated, although $TiO_{2-\delta}$ generated by the photoirradiation of TiO_2 modifies the Rh metal nanoparticles on **8–A** due to the SMSI between the Rh metal nanoparticles and $TiO_{2-\delta}$.

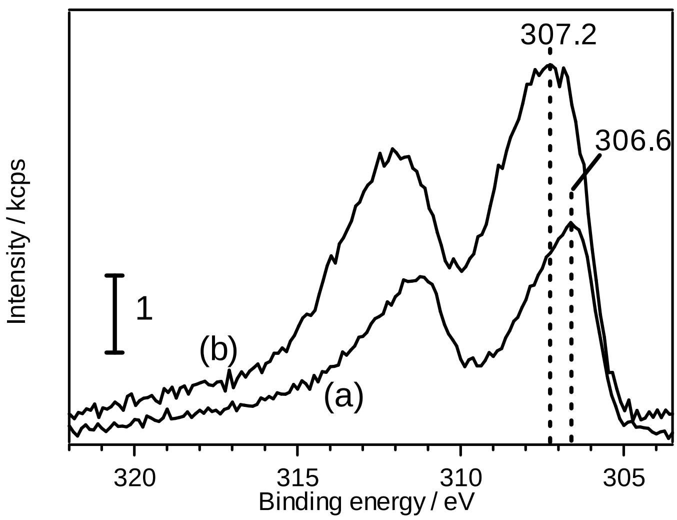

Figure 9. Rh 3d XPS of (a) Rh–3–R and (b) Rh–8–A.

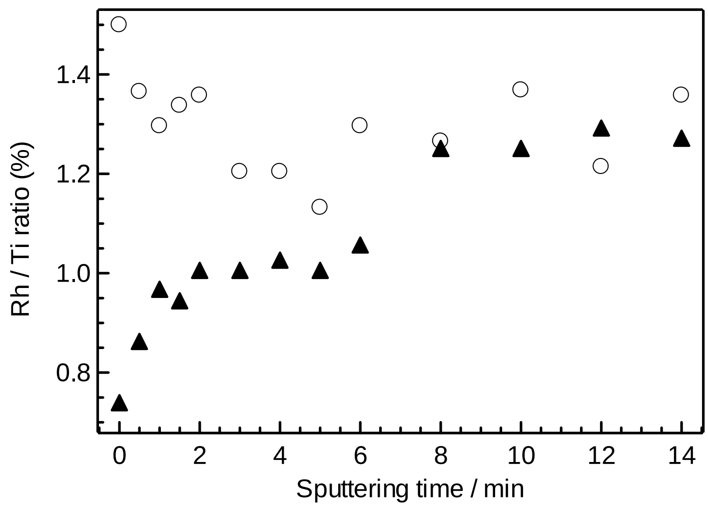

Figure 10. The change in Rh/Ti ratio of Rh–3–R (○) and Rh–8–A (▲) by Xe ion sputtering for 14 min.

Conclusion

In the photodeposition process, the Rh metal nanoparticles with a uniform size appear on both anatase and rutile phase of TiO_2. The appearance rate of Rh metal nanoparticles is constant on the anatase while it decreases with the photoirradiation time on the rutile. The Rh metal species on the anatase is covered with TiO_2, although the aggregated Rh species, which is composed of the primary Rh nanoparticles on rutile phase of TiO_2, are not decorated. The crystalline phase of TiO_2 has a significant effect on both the formation process of Rh metal particles and the structure of photodeposited Rh species.

References

[1] B. Kraeutler, A. J. Bard, *J. Am. Chem. Soc.* **1978**, *100*, 4317-4318.

[2] J. M. Herrmann, J. Disdier, P. Pichat, *J. Phys. Chem.* **1986**, *90*, 6028-6034.

[3] E. Borgarello, N. Serpone, G. Emo, R. Harris, E. Pelizzetti, C. Minero, *Inorg. Chem.* **1986**, *25*, 4499-4503.

[4] J. M. Herrmann, J. Disdier, P. Pichat, *J. Catal.* **1988**, *113*, 72-81.

[5] K. Tanaka, K. Harada, S. Murata, *Solar Energy* **1986**, *36*, 159-161.

[6] M. R. Prairie, L. R. Evans, B. M. Stange, S. L. Martinez, *Environ. Sci. & Tech.* **1993**, *27*, 1776-1782.

[7] D. Chen, A. K. Ray, *Chem. Eng. Sci.* **2001**, *56*, 1561-1570.

[8] G. R. Bamwenda, S. Tsubota, T. Nakamura, M. Haruta, *Catal. Lett.* **1997**, *44*, 83-87.

[9] L.-H. Chang, Y.-L. Yeh, Y.-W. Chen, *Int. J. Hydrogen Energy* **2008**, *33*, 1965-1974.

[10] K. Maeda, K. Teramura, D. Lu, N. Saito, Y. Inoue, K. Domen, *Angew. Chem. Int. Ed.* **2006**, *45*, 7806-7809.

[11] V. Iliev, D. Tomova, L. Bilyarska, A. Eliyas, L. Petrov, *Appl. Catal. B* **2006**, *63*, 266-271.

[12] K. Chiang, R. Amal, T. Tran, *Adv. Environ. Res.* **2002**, *6*, 471-485.

[13] S. Kitano, N. Murakami, T. Ohno, Y. Mitani, Y. Nosaka, H. Asakura, K. Teramura, T. Tanaka, H. Tada, K. Hashimoto, H. Kominami, *J. Phys. Chem. C* **2013**, *117*, 11008-11016.

[14] I. Tsuji, H. Kato, H. Kobayashi, A. Kudo, *J. Am. Chem. Soc.* **2004**, *126*, 13406-13413.

[15] O. C. Compton, E. C. Carroll, J. Y. Kim, D. S. Larsen, F. E. Osterloh, *J. Phys. Chem. C* **2007**, *111*, 14589-14592.

[16] Y. Matsumoto, S. Ida, T. Inoue, *J. Phys. Chem. C* **2008**, *112*, 11614-11616.

[17] D. C. Koningsberger, J. H. A. Martens, R. Prins, D. R. Short, D. E. Sayers, *J. Phys. Chem.* **1986**, *90*, 3047-3050.

[18] S. Sakellson, M. McMillan, G. L. Haller, *J. Phys. Chem.* **1986**, *90*, 1733-1736.

[19] D. Li, N. Ichikuni, S. Shimazu, T. Uematsu, *Appl. Catal. A* **1999**, *180*, 227-235.

[20] V. I. Simagina, O. V. Netskina, O. V. Komova, G. V. Odegova, D. I. Kochubei, A. V. Ishchenko, *Kinet. Catal.* **2008**, *49*, 568-573.

[21] M. R. Gogate, R. J. Davis, *ChemCatChem* **2009**, *1*, 295-303.

[22] S. Bordiga, E. Groppo, G. Agostini, J. A. van Bokhoven, C. Lamberti, *Chem. Rev.* **2013**, *113*, 1736-1850.

[23] A. Caballero, A. R. González-Elipe, A. Fernández, J. M. Herrmann, H. Dexpert, F. Villain, *J. Photochem. Photobiol. A* **1994**, *78*, 169-172.

[24] A. Fernandez, A. Caballero, A. R. Gonzalez-Elipe, J. M. Herrmann, H. Dexpert, F. Villain, *J. Phys. Chem.* **1995**, *99*, 3303-3309.

[25] K. Teramura, S.-i. Okuoka, S. Yamazoe, K. Kato, T. Shishido, T. Tanaka, *J. Phys. Chem. C* **2008**, *112*, 8495-8498.

[26] J. Ohyama, K. Teramura, S. Okuoka, S. Yamazoe, K. Kato, T. Shishido, T. Tanaka, *Langmuir* **2010**, *26*, 13907-13912.

[27] J. Ohyama, K. Teramura, Y. Higuchi, T. Shishido, Y. Hitomi, K. Kato, H. Tanida, T. Uruga, T. Tanaka, *ChemPhysChem* **2011**, *12*, 127-131.

[28] J. Ohyama, K. Teramura, T. Shishido, Y. Hitomi, K. Kato, H. Tanida, T. Uruga, T. Tanaka, *Chem. Phys. Lett.* **2011**, *507*, 105-110.

[29] J. Ohyama, K. Teramura, Y. Higuchi, T. Shishido, Y. Hitomi, K. Aoki, T. Funabiki, M. Kodera, K. Kato, H. Tanida, T. Uruga, T. Tanaka, *PCCP* **2011**, *13*, 11128-11135.

[30] H. Asakura, K. Teramura, T. Shishido, T. Tanaka, N. Yan, C. Xiao, S. Yao, Y. Kou, *PCCP* **2012**, *14*, 2983-2990.

[31] X. Yuan, G. Sun, H. Asakura, T. Tanaka, X. Chen, Y. Yuan, G. Laurenczy, Y. Kou, P. J. Dyson, N. Yan, *Chemistry – A European Journal* **2013**, *19*, 1227-1234.

[32] J. Ohyama, A. Yamamoto, K. Teramura, T. Shishido, T. Tanaka, *ACS Catal.*, **2011**, 187-192.

[33] S. J. Tauster, S. C. Fung, R. T. K. Baker, J. A. Horsley, *Science* **1981**, *211*, 1121-1125.

[34] Y. Li, Y. Fan, H. Yang, B. Xu, L. Feng, M. Yang, Y. Chen, *Chem. Phys. Lett.* **2003**, *372*, 160-165.

[35] In this DXAFS experiments using 8-A, the photodeposition finished after 75 min photoirradiation. That time was shorter than that in our previous paper (90 min). This is because the light intensity of this experiment is higher than that of previous one.

[36] C. D. Wagner, W. M. Ringgs, L. E. Davis, J. F. Moulder, *Handbook of X-ray photoelectron spectroscopy*, Perkin-Elmer Corp., Eden Prairie, MN, **1979**.

[37] A. Fernandez, A. R. Gonzalez-Elipe, A. Caballero, G. Munuera, *J. Phys. Chem.* **1993**, *97*, 3350-3354.

List of Publications

Chapter 1

1. Effect of Reaction Temperature on Photocatalytic Activity for Photo-SCR of NO with NH_3 over a TiO_2 Photocatalyst
   Akira Yamamoto, Yuto Mizuno, Kentaro Teramura, Shishido Tetsuya, and Tsunehiro Tanaka
   Catalysis Science & Technology, **2013**, *3*, 1771–1775.

Chapter 2

2. Visible-light-assisted selective catalytic reduction of NO with NH_3 on porphyrin derivative-modified TiO_2 photocatalysts
   Akira Yamamoto, Yuto Mizuno, Kentaro Teramura, Saburo Hosokawa, Shishido Tetsuya, and Tsunehiro Tanaka
   Catalysis Science & Technology, **2015**, *5*, 556–561.

Chapter 3

3. Visible-Light-Assisted Selective Catalytic Reduction of NO with NH_3 over Dye-Modified TiO_2 Photocatalysts
   Akira Yamamoto, Kentaro Teramura, Shishido Tetsuya, and Tsunehiro Tanaka
   ChemCatChem, **2015,** *in press*.
   DOI: 10.1002/cctc.201500207R1

Chapter 4

4. Effects of SO_2 on Selective Catalytic Reduction of NO with NH_3 over a TiO_2 Photocatalyst
   Akira Yamamoto, Kentaro Teramura, Saburo Hosokawa, and Tsunehiro Tanaka
   Science and Technology of Advanced Materials, **2015**, *16*, 024901 (page 1–9).

Chapter 5

5. Noble-metal-free NO_x storage over Ba-modified TiO_2 photocatalysts under UV-light irradiation at low temperatures
Akira Yamamoto, Yuto Mizuno, Kentaro Teramura, Saburo Hosokawa, and Tsunehiro Tanaka
ACS Catalysis, **2015**, 5, 2939–2943.

Chapter 6

6. Mechanism of NO_x storage over Ba-modified TiO_2 Photocatalysts under UV-light Irradiation: Effect of Ba Loading and Structure of Ba species
Akira Yamamoto, Yuto Mizuno, Kentaro Teramura, Saburo Hosokawa, and Tsunehiro Tanaka
Submitted to Applied Catalysis B.

Appendix

7. Effect of a crystalline phase of TiO_2 photocatalysts on the photodeposition of Rh metal nanoparticles
Akira Yamamoto, Junya Ohyama, Kentaro Teramura, Shishido Tetsuya, and Tsunehiro Tanaka
Catalysis Today, **2014,** *232*, 165–170.